UNIVERSIDAD DE CHILE
FACULTAD DE CIENCIAS FÍSICAS Y MATEMÁTICAS
DEPARTAMENTO DE INGENIERÍA ELÉCTRICA

DESIGN AND EVALUATION OF ANGLE DIVERSITY RECEIVERS CONSIDERING ACCURATE VISIBLE LIGHT COMMUNICATION CHANNEL MODELS IN UNDERGROUND MINES

TESIS PARA OPTAR AL GRADO DE
DOCTOR EN INGENIERÍA ELÉCTRICA

PABLO GEOVANNY PALACIOS JÁTIVA

PROFESOR GUÍA:
CESAR AZURDIA MEZA

MIEMBROS DE LA COMISIÓN:
SANDRA CÉSPEDES UMAÑA
VICENTE MATUS ICAZA
RAFAEL PÉREZ JIMÉNEZ

SANTIAGO DE CHILE
2023

RESUMEN DE LA TESIS PARA OPTAR
AL GRADO DE DOCTOR EN INGENIERÍA ELÉCTRICA
POR: PABLO GEOVANNY PALACIOS JÁTIVA
FECHA: 2023
PROF. GUÍA: CESAR AZURDIA MEZA

DISEÑO Y EVALUACIÓN DE RECEPTORES CON DIVERSIDAD ANGULAR CONSIDERANDO MODELOS PRECISOS DE CANAL DE COMUNICACIÓN POR LUZ VISIBLE EN MINAS SUBTERRÁNEAS

Los enlaces ópticos en el espectro de luz visible, llamados Comunicación por Luz Visible (VLC), están bajo intensa investigación para aplicaciones de Minería Subterránea (UM) debido a sus ventajas en comparación con las tecnologías basadas en Radio Frecuencia (RF). Sin embargo, en este entorno físicamente complejo, el modelado de canal y las soluciones para mejorar la eficiencia del sistema VLC tienden a ser más desafiantes. Esta tesis aborda el desafío de garantizar el correcto funcionamiento de los sistemas VLC mineros subterráneos (UM-VLC) mediante el diseño y la evaluación de Receptores con Diversidad Angular (ADR) en modelos precisos de canal VLC minero subterráneo mediante formulación analítica y simulaciones por computadora. Específicamente, desarrollo modelos precisos de canales UM-VLC modelando distribuciones de dispersores aplicables a escenarios de UM e integrándolos en un modelo general. También evalúo el rendimiento del modelo de canal UM-VLC considerando métricas típicas de rendimiento. Luego, diseño una solución que mejora a los ADRs basada en la orientación adaptativa de los fotodiodos para mitigar problemas de propagación de la señal óptica en escenarios UM-VLC. Los resultados muestran que esta solución, en comparación con los ADR típicos, mejora la señal óptica recibida y el rendimiento del sistema UM-VLC debido a su posicionamiento angular adaptativo óptimo.

SUMMARY OF THE THESIS SUBMITTED
FOR THE DEGREE OF DOCTOR IN ELECTRICAL ENGINEERING
BY: PABLO GEOVANNY PALACIOS JÁTIVA
DATE: 2023
ADVISOR: PROF. CESAR AZURDIA MEZA

DESIGN AND EVALUATION OF ANGLE DIVERSITY RECEIVERS CONSIDERING ACCURATE VISIBLE LIGHT COMMUNICATION CHANNEL MODELS IN UNDERGROUND MINES

Optical links in the visible light spectrum, called Visible Light Communication (VLC), are under intense research for Underground Mining (UM) applications due to their advantages compared to RF-based technologies. However, in this physically complex environment, the channel modeling and solutions to improve the VLC system efficiency are more challenging. This thesis addresses the challenge of guaranteeing the proper operation of UM-VLC systems by designing and evaluating angle diversity architectures in precise UM-VLC channel models via analytic formulation and computer simulations. Specifically, I formulate and develop accurate UM-VLC channel models by modeling scatterer distributions applicable to UM scenarios and integrating them into a scattering channel model. I also evaluate the performance of the proposed UM-VLC channel model by considering performance metrics and comparison with state-of-the-art UM-VLC channel models. Then, I design a solution that improves the angle diversity receivers based on the adaptive orientation of the photo-diodes in terms of the received signal strength ratio scheme to mitigate the optical signal propagation problems in UM-VLC scenarios. Simulation results show that this solution enhances the received optical signal and improves the UM-VLC system performance due to its optimum adaptive angular positioning.

Acknowledgements

I want to acknowledge ANID for supporting me with the Doctoral Grant No. 21190489, as well as the Department of Electrical Engineering, Universidad de Chile, for the opportunity of undertaking my studies in its excellent Ph.D. program. This work received support from ANID FONDECYT Regular No. 1211132 and CODELCO through Piensa Minería.

"If you want a different life, you have to do different things." I would like to express my most sincere gratitude to my esteemed advisor, César A. Azurdia Meza, for unconditionally supporting me throughout the Doctoral process. Your shared knowledge, your dedicated time, and your encouragement throughout my academic research and life itself have made you a wonderful professor and researcher, a great friend, and a great human being.

Next, but no less important are my parents Silvia and Ángel, my sister Krhistin, my girlfriend Cony, my family, and my closest friends. All of them, at some point in this stage, have understood the sacrifice and effort I have made to achieve this goal. Without your support, especially from Ecuador, I would not have achieved this goal.

Finally, I also would like to thank my research teams and colleagues for the kind help, treasured support, and cherished time that we spent together.

Pablo Palacios Játiva

TABLE OF CONTENT

List of Tables

List of Figures

List of Acronyms

ADR	Angle Diversity Receiver
AoA	Angle of Arrival
AWG	Arbitrary Waveform Generator
BER	Bit Error Rate
BEP	Bit Error Probability
CDF	Cumulative Distribution Function
CFoV-ADR	Constrained Field-of-View Angular Diversity Receiver
CIR	Channel Impulse Response
CSI	Channel State Information
DC	Direct Current
DD	Direct Detection
eCA-RSSR	enhanced Camera Assisted Received Signal Strength Ratio
ELM	Extreme Learning Machine
GDP	Gross Domestic Product
GPS	Global Positioning System
ICI	Inter-Cell Interference
IEEE	Institute of Electrical and Electronics Engineers
IM	Intensity Modulation
IoT	Internet of Things
FET	Field Effect Transistor
FoV	Field of View
GPS	Global Positioning System
LED	Light Emitting Diode
LiFi	Light Fidelity
LoS	Line-of-Sight
LS	Least Square
MIMO	Multiple-Input-Multiple-Output
MISO	Multiple-Input-Single-Output
ML	Maximum Likelihood
MMSE	Minimum Mean Square Error

MODTRAN	Atmospheric Radiation Transport Model
NARX	Nonlinear Auto-Regressive Exogenous
NLoS	Non-Line-of-Sight
OFDM	Orthogonal Frequency Division Multiplexing
OOC	Optical Orthogonal Codes
OOK	On-Off Keying
PD	Photo Diode
PDF	Probability Distribution Function
PLC	Power Line Communication
PMU	Phasor Measurement Unit
RF	Radio Frequency
RMS	Root Mean Square
RSS	Received Signal Strength
RSSR	Received Signal Strength Ratio
RS-GBSM	Regular-Shaped Geometry-Based Stochastic Mode
SER	Symbol Error Rate
SB	Single Bound
SINR	Signal-to-Interference-plus-Noise-Ratio
SISO	Single-Input-Single-Output
SDR	Software Defined Ratio
SNR	Signal to Noise Ratio
TIA	Trans-Impedance Amplifier
ToA	Time to Arrival
UM	Underground Mining
VLC	Visible Light Communication
VLP	Visible Light Positioning
UDR	User Data Rate
UDSM	Unified Disk Scattering Model
ZF	Zero Forcing

Chapter 1

Introduction

The working environment and physical characteristics of underground mines are considered dangerous and unsafe [1]. External factors generated by the regular operation of the mine such as dust, toxic components, and sewage water make the underground mining environment one of the harshest environments [2]. Therefore, it is necessary to establish reliable and stable communication systems to manage day-to-day communication, along with emergencies that may occur in this environment (landslides, fires, or the intoxication of workers). However, the physical conditions of underground mines present a challenge for the development of reliable and effective communication systems [3]. Furthermore, underground mining tunnels need good lighting that meets international standards. However, this problem in some countries also remains without efficient solutions. These challenges are presented as opportunities for proposals for emerging and complementary communications systems that optimize communication and lighting in underground mining environments. To meet these requirements, the concept of Visible Light Communication (VLC) has been introduced for underground mining communication [4]-[7].

It is well known that by modeling the communication channel realistically and efficiently, the overall performance of the communication system can be improved [8]. Furthermore, adequate modeling ensures a correct approach and contextualization of the problems that may arise in communication systems [7,9]. Under this context and compared to existing works in the literature, in [10], a more complete VLC channel model applied to underground mines was proposed, which is part of the contributions of this thesis. Here, the tilt and rotation of Light Emitting Diodes (LEDs) and Photo-Diodes (PDs) that impact Line-of-Sight (LoS) and Non-Line-of-Sight (NLoS) components of the optical link were characterized and included in the model. In addition, the characterization of non-flat walls in tunnels and their reflection effects on the optical signal were considered. Finally, a shadowing model that considers the entry of objects into the underground mining tunnel and a scattering model based on a disk-shaped distribution of dust particles around the optical receiver were considered. It should be noted that the scatterer distribution model used in [10] is easy to develop and implement. Therefore, it was necessary to develop and study more realistic and accurate scatterer distribution models regarding the behavior of dust particles in the tunnel, which was addressed in [11]. This contribution allowed us to improve the channel model presented in [10] adjusting it in its precision and realism for a better representation of the external

variables that influence the underground mining environment.

As the study of VLC systems applied to underground mines is considered a new area of application, problems such as low light coverage in tunnels that generate poor signal propagation, or otherwise, when there are many transmitters (LEDs) that produce Inter-Cell Interference (ICI) and Signal-to-Interference-plus-Noise-Ratio (SINR) fluctuations have not yet been addressed in detail. This implies that solutions such as those based on Angle Diversity Receivers (ADRs) have not been tested in these scenarios either. In this context, in [12], a solution to mitigate ICI based on a hemidodecahedric ADR is presented. However, the main limitation of this work is not the ADR proposal, but rather that its analysis and performance test were carried out in a mining environment using the typical indoor VLC channel as a reference. Therefore, verifying the efficient mitigation of the ICI through the use of the hemidodecahedric ADR implementing it in an underground mining VLC scenario with the specific VLC channel for underground mines presented in [10] is an open topic. In addition, as these types of solutions are new and easy to design, develop and implement due to their low complexity, cost, and processing, it is essential to investigate and propose more solutions based on ADR that further optimize the mitigation capacity of propagation problems of the signal in VLC systems applied to underground mines.

1.1 Motivation

Underground mining leads the mining industry globally and its growth is expected to continue over the years. Such is the importance of this industry that in 2006, the United States government updated its security policies and enacted Public Law 109-236 [13]. In this law, security activities such as tracking mining workers inside the mine and information on their activity are mandatory. Therefore, in order to comply with international safety standards and regulations within underground mining tunnels, it is necessary to improve the technological infrastructure that supports the regulated applications for these scenarios. Despite the existence of technologies based on Radio Frequency (RF), wire, or hybrid, which have been applied to underground mines, these scenarios are unique and hostile, and generate different limitations to current technologies [14]. For this reason, it is important to propose alternative communication systems that adapt to the characteristics of these scenarios. Among the possible solutions with the greatest popularity in recent years are VLC-based systems [4]-[7]. Its features of immunity to electromagnetic interference, low installation cost, use of an unlicensed spectrum range, and also providing lighting make it an ideal solution for the dynamic and dangerous environment of underground mines [15, 16].

It is important to note that in the specialized literature and the mining industry, VLC is presented as a complementary technology and not a solution that will replace RF-based technologies, such as 5G in underground mines. Although 5G has been widely promoted and implemented in mines for some years now [17]-[20], several differentiations from VLC technology can be considered [21]. First, compared to other RF technologies, 5G is more energy efficient; however, VLC is more efficient in terms of Mbps/WATT. Second, VLC is notably more secure in terms of end-to-end communication and information security, as it is a confined technology. Third, since 5G is an RF-based technology, it is prone to electromagnetic interference. Therefore, in RF-sensitive environments, such as the interior of

underground mines, its performance could decrease under certain adverse circumstances. In contrast, VLC does not have this electromagnetic interference problem, due to its physical nature of data communication using light as a medium. Fourth, one of the main differentiators is based on the paradigm that the underground mining environment is hostile and one of its most critical needs is lighting. Thus, VLC would take advantage of the existing lighting infrastructure in underground mines, thereby reducing implementation costs, which are in fact cheaper than 5G-based technologies. Finally, in terms of critical applications for underground mines, we can mention that geolocation, such as Global Positioning System (GPS), is one of them. Therefore, given the physical characteristics of the mining tunnel, it is very difficult to implement it with traditional technologies. Therefore, VLC is presented as a fairly reliable alternative to improve the performance of this type of geolocation-based applications [22]-[24]. These differentiators allow us to consider that 5G and VLC can be complementary technologies in an underground mining environment, each with its advantages and disadvantages. An additional consideration that could serve for the proposal of hybrid networks (RF/VLC) is given under the definition that the communication system of a backbone network that could be based on 5G can be reused in VLC. However, our proposal focuses on the last mile located inside the underground mines.

As we have previously discussed, the application of VLC technology to underground mining environments is relatively new, underground mining VLC channel models have not been studied in depth. An underground mine is composed of irregular tunnels, which have characteristics that do not appear in typical indoor environments. Factors such as dust particles that cause scattering, heavy machinery that creates shadowing, and non-flat walls and ceilings, which require angular positioning of the LEDs and PDs to provide better illumination and light reception within the tunnel respectively are a challenge to be considered in the underground mining VLC channel model. On the other hand, it is well known that by modeling the communication channel, the overall performance of the system can be improved using dedicated time/frequency techniques [8]. Therefore, a robust and accurate VLC channel model for underground mines will allow us to design reliable VLC systems for these scenarios. This will be possible if we model in a realistic way the intrinsic phenomena of tunnel work, for example, the behavior and distribution of the dust that generates scattering, and we include it in the general VLC underground mining model.

As we can see, the typical indoor VLC channel is inefficient in its application to underground mining environments. Therefore, with a precise VLC channel model for underground mining tunnels, we will also be able to better analyze and contextualize the problems present in the VLC system. In general, among the main issues that could affect the overall performance of VLC systems in underground mines are poor signal propagation due to low light coverage in tunnels, ICI and SINR fluctuations [25]-[28]. These are challenges that must be addressed to improve the efficiency of the underground mining VLC system. To contribute to the mitigation of these problems, solutions based on the use of multiple PDs in reception located in geometric distributions called ADR have been studied [25, 26, 29]-[32]. Among its advantages are the diversification of the received optical signal, a narrow Field-of-View (FoV), greater granularity, and fast processing of the optical signal. Therefore, it is necessary to explore solutions based on ADRs, implement them in the underground mining VLC system with its specific and precise channel for this scenario, and verify the improvement of the communication system performance.

1.2 Problem Statement

I am interested in obtaining a specific VLC channel model for underground mining environments that serves as a baseline to develop more robust and accurate VLC applications and systems for these environments. In summary, the literature review shows that the channel model assumed by various authors for underground mining VLC environments is the same as that used for indoor VLC environments [6, 7, 33]-[36]. However, little or no evidence is presented to justify the assumed models and the main factors that could affect the VLC link are not included in their analytical expressions. In this context, including all the intrinsic characteristics of underground mining tunnels such as positioning of LEDs and PDs, non-flat walls, scattering and shadowing are essential. Although there are several studies on the effect of scattering in typical VLC indoor environments, this phenomenon has not been extensively and adequately analyzed in underground mining environments [37]-[42]. Few VLC channel modeling studies for underground mines consider dust particles. However, these proposals are not very realistic because they are based on the assumption of the typical indoor VLC channel. Therefore, modeling in a realistic way and with a random approach, the physical phenomenon of scattering in the underground mining scenario will allow us to have a more accurate underground mining VLC channel model and therefore better systems and applications.

On the other hand, VLC systems applied to underground mines are very noisy schemes with poor lighting coverage. Therefore, due to the nature of light, they are prone to poor optical signal propagation and interference. This interference can be from external light sources or internal light interference itself. Due to the characteristics of darkness in a tunnel, there must be multiple optical transmitters installed along the tunnel, because it is necessary to have complete lighting and communication coverage in these scenarios. Each optical transmitter (LED) generates an optical cell of determining dimensions. According to the position of the LEDs and the dimensions of their optical cells, adjacent cells may have areas of overlap. It is precisely in this overlapping area that there is strong interference as a result of receiving several different optical signals from different LEDs. Therefore, the problem of ICI occurs, because the SINR of the optical signal constantly decreases or fluctuates [25, 26, 29, 32, 43]-[45]. It has been verified that if the distance measured between two optical transmitters is less than or equal to the diameter of the optical cell, there will be an area of overlap and consequently ICI [12]. Therefore, this problem will be present frequently in underground mining scenarios and the research for solutions to mitigate these inconveniences is an open issue.

1.3 Hypothesis

The appropriate operation of underground mining VLC systems (in terms of signal reception quality, communication reliability, and bit error rate) can be achieved by designing low-complexity ADR-based architectures taking into consideration precise underground mining VLC channel models.

1.4 General Objective

Design and evaluate ADR architectures in precise underground mining VLC channel models via analytic formulation and computer simulations to provide the proper operation of underground mining VLC systems in terms of signal reception quality, communication reliability, and bit error rate.

1.5 Specific Objectives

1. To propose, model, and validate scatterer distributions in underground mining scenarios for their integration into a scatterer channel component model through statistics and mathematical modeling in order to improve the underground mining VLC channel model and ensure communication reliability.
2. To design, model, and validate low complexity ADR-based architectures that integrate mechanisms to diminish the optical signal propagation problems in VLC underground mining scenarios, considering the trade-off between the design objectives such as the number of PDs and geometric complexity in order to ensure the communication reliability.
3. To evaluate the performance of the proposed underground mining VLC channel with the scatterer channel component through numerical analysis and simulations, considering performance metrics such as channel impulse response and bit error rate, and comparison with state-of-the-art underground mining VLC channel models.
4. To evaluate the performance of the ADR-based architectures by using realistic simulation frameworks, considering metrics related to design goals such as user data rate and received power, and a comparison with other relevant ADR schemes.

1.6 Contributions

This thesis contributes to the current state of knowledge by improving the underground mining VLC channel model through a suitable dust particle model and by improving the optical signal reception through efficient ADR architectures. First, I have derived and provided an underground mining VLC channel model specific to this harsh environment, which involves features such as the random orientation of LEDs and PDs, non-regular walls, and the effects of shadowing and scattering phenomena. Second, I verified and evaluated the derived channel model by obtaining analytical expressions of the statistical distribution of the underground mining visible light communication square-channel gain. These expressions are used to compute the system's Bit Error Probability (BEP) considering shot and thermal noises, On-Off Keying (OOK) modulation, as well as perfect and imperfect Channel State Information (CSI) at the receiver side. Third, I improved the derived underground mining VLC channel model by introducing a suitable dust particle distribution model compatible with these scenarios to describe the dispersion phenomenon coherently in order to design realistic UM-VLC systems with better performance. Consequently, I carried out an in-depth study of the interaction of optical links with suspended dust particles in the UM environment and the atmosphere. Furthermore, I analytically derived a 3D hemispherical dust particle distribution model, together with its main statistical parameters. Fourth, to improve the reception performance of the underground mining VLC system, I provided and designed a

novel solution that involves an improvement to the ADRs based on the adaptive orientation of the PDs in terms of the Received Signal Strength Ratio (RSSR) scheme. Specifically, this methodology is implemented in a hemidodecahedral ADR. The contributions made in this thesis have been tested in a computer simulation framework of the VLC underground mining system. This simulation tool was developed by me throughout my Doctoral process. The base software of the mining environment and VLC system created was Matlab. It was decided to create our own simulation environment due to the cost of specialized software and the lack of specific simulation scripts or developments for VLC systems applied to hostile environments. This simulation tool developed for the thesis allowed us to verify metrics such as channel impulse response, received power, Root Mean Square (RMS) delay spread, user data rate, and Bit Error Rate (BER) in each of the contributions proposed throughout the doctoral work.

1.7 Thesis Organization and Papers Published

This doctoral thesis is organized according to "Format 2: New optional doctoral thesis format based on 2 accepted/published ISI journal papers." https://www.die.cl/sitio/proceso-de-doctorado/.

Therefore, Chapter 1, the Introduction, addresses the following topics: the research motivation, the problem statement, the general and specific objectives, the hypotheses, the contributions, the thesis organization, and the papers published.

As a result of this doctoral thesis, four journal papers (WoS) were published. As Format 2 requires, the contents of Chapters 2 through 5 are the published papers in chronological order. In Appendix A you can find the articles that make up the chapters of this thesis.

Chapter 2 [10] contains the first journal paper, published in IEEE Access, 2020. This research was an improvement to the work carried out in [12], in which a solution based on a hemidodecahedral ADR architecture was presented to mitigate the ICI in VLC systems applied to underground mining. However, the channel model used is not suitable for these environments. Therefore in this research [10], I proposed a novel channel model that incorporates important factors that influence the quality of the VLC link in underground mines. Features such as arbitrary positioning and orientation of the optical transmitter and receiver, tunnels with irregular walls, shadowing by large machinery, and scattering by dust clouds are considered. These factors are integrated into a single modeling framework that lends itself to the derivation of compact mathematical expressions for the overall Direct Current (DC) gain, the Channel Impulse Response (CIR), the RMS delay spread, and the received power of the proposed VLC channel model. Our analytical results are validated by computer simulations. These results show that the rotation and tilt of the transmitter and receiver, as well as the tunnels' irregular walls, have a notorious influence on the magnitude and temporal dispersion of the VLC channel's LoS and NLoS components. Furthermore, results show that shadowing reduces the LoS component's magnitude significantly. The findings also show that scattering by dust particles contributes slightly to the total VLC channel gain, although it generates a large temporal dispersion of the received optical signal.

Chapter 3 [46] contains the second journal paper, published in AEU-International Journal

of Electronics and Communications, 2022. In this research, I evaluated the performance of the VLC underground mining channel proposed in [10]. I derived analytical expressions of the statistical distribution of the underground mining visible light communication square-channel gain. These expressions are employed to compute the system's BEP considering shot and thermal noises, OOK modulation, as well as perfect and imperfect CSI at the receiver side. The results obtained for the BEP are validated by computer simulations for various underground mining visible light communication scenarios. Simulation results demonstrated that the performance of the UM-VLC system improves by increasing the FoV and/or Signal to Noise Ratio (SNR). Indeed, for an FoV value of 45° for both the UM-VLC system with perfect CSI and imperfect CSI, the best performance in terms of BEP is obtained. In terms of the UM-VLC system with imperfect CSI, BEP curves saturate for higher values of SNR due to lower values of FoV, specifically in the case of 45°. Finally, the performance of the underground mining visible light communication system increases significantly for higher values of SNR, specifically in the case of 20 dB.

Chapter 4 [11] contains the third journal paper, published in Sensors MDPI, 2022. In this research, first, I focused on presenting an in-depth study of the interaction of optical links with dust particles suspended in the UM environment and the atmosphere. Then, I analytically derived a hemispherical 3D dust particle distribution model, along with its main statistical parameters. This analysis allowed me to develop a more realistic scattering channel component and present an improvement to the underground mining VLC channel model obtained in [10]. Finally, I evaluated the performance of the channel model derived using computational numerical simulations following the IEEE 802.1.5.7 standard in terms of CIR, received power, SNR, RMS delay spread, and BER. The results demonstrate that the hemispherical dust particle distribution model is more accurate and realistic in terms of the metrics evaluated compared to other models found in the literature. Furthermore, the performance of the UM-VLC system is negatively affected when the number of dust particles suspended in the environment increases.

Chapter 5 [47] contains the fourth journal paper, published in Entropy MDPI, 2022. This research was oriented to present a novel solution that involves an improvement to the ADRs based on the adaptive orientation of the PDs in terms of the RSSR scheme. Specifically, this methodology is implemented in a hemidodecahedral ADR and evaluated in a simulated UM-VLC scenario. The performance of the proposed design is evaluated using metrics such as received power, user data rate, and BER. Furthermore, this approach was compared with state-of-the-art ADRs implemented with fixed PDs and with the Time of Arrival (ToA) reception method. An improvement of at least 60% in terms of the analyzed metrics compared to state-of-the-art solutions is obtained. Simulation results demonstrate that the hemidodecahedral ADR, with adaptive orientation PDs, enhances the received optical signal. Furthermore, the proposed scheme improves the performance of the UM-VLC system due to its optimum adaptive angular positioning, which is completed according to the strongest optical received signal power. By improving the performance of the UM-VLC system, this novel method contributes to further consideration of VLC systems as potential and enabling technologies for future 6G deployments.

Finally, Chapter 6 contains the general conclusions of this thesis as well as future work.

Appendix A contains the published papers in journals (WoS) and conferences that contributed to the development of this thesis, and Appendix B contains the main matlab code as a baseline of the simulations to obtain the results of the thesis work

1.8 Other Publications

This doctoral thesis is composed of four papers published in journals (WoS). However, there are twelve more published papers; two in journals (WoS) and ten at conferences, which are directly related to the topic addressed in this thesis and therefore are additional contributions. In the following, the published papers are presented in chronological order.

The work in [48] is a published conference paper, presented at the IEEE CHILECON, 2019. In this paper, Orthogonal Frequency Division Multiplexing (OFDM) techniques designed for Intensity Modulation/Direct Detection (IM/DD) modulation applied to VLC systems are evaluated. The work in [49] is a published conference paper, presented at the IEEE Latin-American Conference on Communications, 2019. In this paper, the application and benefits of several combining schemes to create diversity at the optical receiver are analyzed and compared in a multi-cell indoor VLC system. The work in [50] is a published conference paper, presented at the IEEE South American Colloquium on Visible Light Communications (SACVLC), 2019. In this paper, several OFDM-based VLC techniques designed for IM/DD are evaluated and compared for various optical channels. Evaluations are done for LoS and NLoS channels. The work in [51] is a published conference paper, presented at the International Conference on Applied Technologies, 2019. In this paper, one of the first analysis of a VLC system applied to underground mining environments is presented.

The work in [12] is a journal paper (WoS), published in Sensors, 2020. This paper proposes two solutions based on ADRs to mitigate the ICI in underground mining VLC systems, one of them is a novel approach. The work in [52] is a published conference paper, presented at the 12th International Symposium on Communication Systems, Networks and Digital Signal Processing (CSNDSP), 2020. In this paper I presented the empirical path loss distribution in underground mining environments. Considering tunnel dimensions and optical signal components, path loss expressions are mathematically determined by using a curve fitting technique. The work in [53] is a published conference paper, presented at the IEEE Latin-American Conference on Communications, 2020. In this paper, a study on the special physical characteristics and external factors of UM that affect the performance of VLC systems applied to these environments is presented. The work in [54] is a published conference paper, presented at the IEEE Latin-American Conference on Communications, 2020. In this article I evaluated the impact of using intelligent reflecting surfaces in a diffuse visible light communications link. I proposed a propagation model in order to consider different types of reflective surfaces, namely, diffuse, specular and glossy.

The work in [55] is a published conference paper, presented at the 3rd IEEE South American Colloquium On Visible Light Communications (SACVLC), 2021. In this paper, three OFDM schemes are simulated and applied in the UM-VLC system. The work in [56] is a published conference paper, presented at the IEEE Latin-American Conference on Communications (LATINCOM), 2021. In this paper, the channel estimation and equalization based

on the standard extreme learning machine (ELM) scheme applied to UM-VLC systems are presented. To verify the performance of the proposed technique, typical channel estimation schemes such as least square (LS), Minimum Mean Square Error (MMSE), and Spectral Temporal Averaging (STA) were implemented using Zero-Forcing (ZF) as the equalizer. The work in [57] is a journal paper (WoS), published in Photonic Network Communications, 2022. This article developed a study and characterization of the UM tunnels' physical factors and external phenomena, as well as the orientation of optical components that affect the performance of VLC systems. In order to evaluate and verify the behavior of the underground mining VLC channel, the CIR and the received optical power distribution in the tunnel scenario were presented. The work in [58] is a published conference paper, presented at the 13th International Symposium on Communication Systems, Networks and Digital Signal Processing (CSNDSP), 2022. In this article, I proposed the implementation of pyramidal and hemi-dodecahedral ADRs in the reception stage of a UM-VLC system. These solutions, along with the Maximum Ratio Combining (MRC) signal selection scheme, are evaluated and compared in terms of User Data Rate (UDR) and Cumulative Distribution Function (CDF) with respect to the SINR. The published papers that contributed to the development of this thesis are shown in Appendix A along with co-authored papers that also contributed to this thesis.

Chapter 2

A VLC Channel Model for Underground Mining Environments with Scattering and Shadowing

Underground mining is an industry that preserves the miners' safety and efficiency in their work using wireless communication systems as a tool. In addition to communication links characterized by radio frequency signals, optical links in the visible light spectrum are under intense research for underground mining applications due to their high transmission rates and immunity to electromagnetic interference. However, the design of a robust VLC system for underground mining is a challenging task due to the harsh propagation conditions encountered in mining tunnels. To assist researchers in the design of such VLC systems, we present in this paper a novel channel model that incorporates important factors that influence the quality of the VLC link in underground mines. Features such as an arbitrary positioning and orientation of the optical transmitter and receiver, tunnels with irregular walls, shadowing by large machinery, and scattering by dust clouds are considered. These factors are integrated into a single modeling framework that lends itself to the derivation of compact mathematical expressions for the overall DC gain, the impulse response, the root mean square delay spread, and the received power of the proposed VLC channel model. Our analytical results are validated by computer simulations. These results show that the rotation and tilt of the transmitter and receiver, as well as the tunnels' irregular walls, have a notorious influence on the magnitude and temporal dispersion of the VLC channel's LoS and NLoS components. Furthermore, results show that shadowing reduces the LoS component's magnitude significantly. Our findings also show that scattering by dust particles contributes slightly to the total VLC channel gain, although it generates a large temporal dispersion of the received optical signal.

2.1 Introduction

The inherent working environment of underground mines is considered as very dangerous and unsafe due to inherent characteristics of the tunnels [1], as well as numerous external agents generated by regular mine operation such as dust, toxic components, and sewage water,

among others [59]. These factors make the underground mining environment be considered one of the most harsh environments for work and for establishing reliable communication links [60]. To manage day-to-day communication, along with the emergencies that can occur in this environment (landslides, fires, or intoxication of workers), a stable communication system is required [3]. This system must be designed to support applications focused on reliably localize and monitor infrastructure, and provide real-time information of all personnel within the tunnel infrastructure [61]. However, the physical conditions of the underground mines present a challenge for developing reliable and effective communication systems.

The geometric characteristics of the underground mine environment (the shape of walls and roof), as well as the interference and electromagnetic noise produced by the machinery employed in mining, contribute to the difficulty of the communication system design [62]. In other words, the previous factors cause problems in the communication systems frequently used in mines, which are normally based on RF. Among the main complications of RF-based underground mining communications systems are a poor BER, a high delay spread in the signal, and a limited data transmission rate [63]. One solution to these issues comes from the combination of RF technologies with the novel scheme termed VLC, which also provides continuous lighting within the underground mining environment [64].

VLC systems have several benefits, such as the use of unlicensed spectrum ranging from 400 THz to 800 THz, system elements with reasonable prices, and immunity to electromagnetic interference, for instance, [65,66]. These advantages make VLC a good candidate to get secure, robust, and reliable communication in underground mining environments [12]. Unfortunately, in this physically complex environment, the channel modeling tends to be more challenging in comparison to the traditional indoor scenarios where a VLC link is generally adopted [67].

An underground mine is composed of irregular tunnels, which present features that do not appear in typical indoor environments [68]. Factors such as dust particles that cause scattering, heavy machinery that generates shadowing, and non-flat walls and ceilings, which require angular positioning of the LEDs and PDs to provide better illumination and light reception inside the tunnel respectively are challenging for the VLC design in mining environments. On the other hand, it is well known that by modeling the communication channel, the overall system performance may be enhanced by using dedicated time/frequency techniques [8]. To the best of our knowledge, specifically applied to underground mining VLC systems, no channel model that considers its complicating characteristics has been presented. Based on an extensive review of the state of the art (see Section 2.2), and in an effort to design better underground mining communication systems, we present a VLC channel model that considers physical features that will have an effect on mining tunnels. We characterize and include in the underground mining VLC channel model the tilt and rotation of LEDs and PDs that impact the LoS and NLoS components of the optical link. The characterization of non-flat walls in tunnels and their reflection effects in the optical signal are further considered. Finally, a scattering model that considers a disk-shaped distribution of the dust particles around the optical receiver, and a shadowing model that takes into account the entry of objects into the mining scenario are considered. The inclusion of the aforementioned parameters help us to understand the differences between a referential (typically indoor) VLC channel and a UM-VLC channel. For channel modeling, we use the ray tracing methodology,

which allows an accurate description of the interaction of rays emitted from LEDs to PDs within the underground mining environment.

The main contributions of this paper are summarized as follows:

1. Discussing the differences between the proposed underground mining VLC channel and the typical indoor VLC channel, which is used as a reference VLC channel model.
2. Adjusting and analyzing the effect of non-flat and non-regular tunnel walls, that generate non-orthogonal reflections, to properly model the optical signal in the proposed underground mining VLC channel.
3. Proposing a ray tracing-based underground mining VLC channel model that includes the effects of scattering and shadowing phenomena due to the presence of dust particles and objects (machinery), respectively. Firstly, the entry of objects that cause shadowing in the mining scenario is statistically modeled through a Poisson process. Secondly, the distribution and interaction of the dust particles are statistically modeled through a disk-shaped distribution, and by using the theories of Mie and Rayleigh scattering.

2.2 Related Work

2.2.1 VLC Applications in Underground Mines

In the state of the art, several applications for VLC systems in underground mines have been proposed [12,69]-[74]. Among the most popular applications are those of location inside underground mining tunnels.

In [69], a hybrid system based on VLC and Power Line Communication (PLC) for mines is proposed by showing its design and corresponding experimental demonstration. The channel model used for the evaluation of the VLC system is the Lambertian optical model, where only the LoS component is considered. Numerical results are presented in terms of the horizontal illumination and power received. These results indicate that the proposed VLC system can provide adequate lighting and good data transmission performance for mine communication applications. In [12], a solution to mitigate ICI in an underground mining VLC system based on ADR is proposed. The implemented optical channel is based on the Lambertian model by considering the LoS and NLoS components, as well as shot and thermal noises. The employed metrics to evaluate the solution are illuminance, RMS delay spread, UDR, BER, and SINR. The analysis of these metrics corroborates and validates the ICI mitigation in the VLC system applied to the underground mining environment. In [70], a method of positioning in underground mines based on the VLC technology is studied in detail. In this work, the author briefly provides theoretical concepts about the factors that could affect the mining VLC channel and how they would be involved in improving the capacity of the location system. In [71, 72], a VLC-based system along with a trilateration technique for locating objects and people in an underground mining tunnel is proposed. In addition, the typical indoor VLC channel model is used to verify the performance of the proposed system. Localization error results show that the proposed application has a better performance compared to typical localization technologies. In [73], another system based on a VLC scheme for localization by using three-dimensional trilateration is proposed. The channel model used for this work is the typical indoor VLC channel model. Location error, despite not having implemented its

own VLC channel model for tunnels, is low compared to other RF-based technologies. In [74], a hybrid VLC-RF scheme by showing the implementation of a portable Phasor Measurement Unit (PMU) for deep underground tunnels is proposed. Here, for the information download link, the proposed system uses VLC technology. However, the authors highlight that a generic channel model for VLC systems in underground mining has not been proposed. Therefore, a typical indoor VLC channel model is employed. Experimental tests demonstrate the feasibility of the prototype, which has a better performance compared to commercial PMUs.

The extreme conditions present throughout the tunnel are important characteristics to consider when we design VLC-based applications for underground mines. High levels of humidity, dust in the air, extreme heat, and machinery within the mine can affect the performance of the VLC system and applications based on it. Therefore, we believe that the revised VLC-based underground mining applications could improve their performance if they use our proposed VLC channel model in their development. In this context, our channel model proposal considers the most critical factors present in underground mines that are not considered in the traditional indoor VLC channel, which are the positioning of LEDs and PDs, non-flat walls, shadowing, and scattering. Hence, VLC-based applications such as positioning, location, and real-time data transmission in underground mines would be more accurate and robust.

2.2.2 Works Related to Underground Mining VLC Channel Models

In this subsection we present the most relevant and recent works reported in the literature that describe VLC channel models applied to underground mining environments [34, 36, 68, 75]-[77].

In [34, 75], a path loss model for a VLC channel applied to mines and two mining VLC communication scenarios, named mining roadway and mining working face, are proposed. In both works, the channel model is based on the well-known Lambertian optical model for indoor environments, where the LoS and NLoS components are considered. The system performance is evaluated in terms of the path loss distribution and RMS delay spread in the first work [75]. Whereas in [34], the analysis focused on the CIR and received power. Both manuscripts demonstrate that the path loss exhibits a linear behavior in the log domain. However, their results are based on a channel model that does not include in its analytical expression the main components that affect underground mining tunnels. In [76], an optical channel taking into account the reflections that occur in a confined structure, such as tunnels, is characterized. The adopted model is the Lambertian VLC channel model with direct and diffuse components. The VLC system performance is evaluated through simulations, and the results are presented in terms of the Symbol Error Rate (SER). The results show that the VLC system robustness during tunnel construction, in terms of SER, is improved. Despite the fact that its results are obtained by simulating a tunnel scenario, the channel model limits them because it does not consider factors such as shadowing or scattering. In [77], the first analysis of a VLC channel model that considers an intrinsic characteristic of mines, such as dust particles, is presented. This paper studies the effects of coal dust particles in terms of optical signal degradation. This phenomenon is analyzed using a Lambertian VLC channel model by considering LoS and NLoS components, and the results are presented in terms of

the CIR. These results show the optimized location of the optical transmitter to decrease the effect of dust on the degradation of the optical signal. However, the limitation of this work is not to include the effect of scattering directly in the theoretical model of the channel, since the analysis of its effect is developed as a factor external to the channel. In [68], the analysis on a VLC channel applied to underground mines is presented. The effect of shadowing and scattering are analyzed as channel-independent phenomena. Consequently, the effects of these phenomena are not included in the analytical model of the VLC channel, so this omission would be its main limitation. The channel model is based again on the Lambertian optical scheme with LoS and NLoS components. Therefore, angular variations of transmitter and receiver, and the effect of non-flat walls are considered neither. The channel is evaluated in terms of the path loss and RMS delay spread. The results demonstrate the linear behavior of the path loss and depict differences in the RMS delay spread for different mining scenarios.

Finally, in [36], a neural network-based approach is applied to derive an underground mine VLC channel model. The proposed channel model is based on nonlinear Auto-Regressive Exogenous Parameters (NARX). Furthermore, the authors assumed a dynamic non-linear behavior of the optical channel. This work is experimentally validated in a dark gallery with a curved roof that emulates a mining tunnel. The main contribution of this work is the estimation of the parameters used for the neural network-based VLC channel model applied to underground mining environments. However, a disadvantage of this work is that the model does not consider the scattering or shadowing phenomena in the estimated coefficients.

In summary, this literature review depicts that the channel model assumed by several authors for underground mining VLC environments is the same as the one used for indoor VLC environments. However, little or no evidence is presented to justify the assumed models because they do not include the main factors of underground mines in their analytical expressions. In contrast to this works, we consider that in practical underground mining scenarios, LEDs would not always be located on the ceiling pointing directly downwards, the PDs would not be fixed pointing directly upwards since they could be installed in the helmets of the miners, and the shadowing and scattering phenomena must be included directly in the underground mining VLC channel model. These assumptions should be considered because they directly influence the quality of the received optical signal, which could affect the performance of the VLC system at the underground mine.

Moreover, in works that consider optical signal reflections, reflective surfaces (roof or walls) are flat and regular. This idea would also be unpractical because of the tunnels are U-shaped and the walls are irregular and non-flat. On the contrary, we consider the irregularity of reflective surfaces by randomly modeling their normal vectors through their angles of rotation and tilt. These considerations influence the reflections that are modeled as random Lambertian point sources, and the radiation intensity of these "sources" is included in the underground mining VLC channel model.

2.2.3 Scattering and Shadowing Models Applied to VLC Indoor Non-Mining Channels

The scattering and shadowing effects on the underground mining VLC channel have not been studied in depth in the literature, nevertheless, these effects have been analyzed in

VLC channels applied to typical indoor environments [37]-[42, 78]-[82].

One of the first investigations that consider shadowing in an indoor VLC environment is presented in [78]. In this work, the shadowing effect is produced by humans, who are modeled as cylinders. In [79], shadowing on the VLC indoor scenario is also generated by the human body where it is modeled as a cubic object. In [80], the authors continue with the trend of considering humans as blocking agents of the optical signal and modeling it as cylindrical objects. The novelty in previous work is to model the effect of shadowing on the VLC indoor stage as a Gaussian bi-modal distribution. In [81], a new study that considers shadowing in a Light Fidelity (LiFi)/RF hybrid indoor environment is proposed. The authors present the objects that cause shadowing as cylinders by affecting the LoS and NLoS components. Finally, in [82], the authors consider the behavior and dimensions of the objects that produce shadowing as similar as possible to what happens in an underground mining scenario. In addition, a joint probability distribution to characterize the size and the position of the obstructions is introduced. According to our analysis of the literature, this work widely considers the real characteristics of a scenario in its statistical model. Therefore, we adapted its methodology for shadowing modeling that we developed in our underground mining VLC channel model proposal (see Section 2.5). This adaptation is achieved by adjusting the obstacle entry model to the proposed mining scenario, by considering realistic obstacle dimensions, and by establishing optical link-blocking conditions typical of the tunnel.

On the other hand, the works related to scattering models applied to general RF communication schemes and optical systems are presented in [37]-[42]. In [37] and [38], a uniform distribution model of scatters is presented, which are located in a disc plane centered on the receiver. For this work, the receiver comes to be a mobile station. Although the focus of this work is not optical systems, the proposed model could be generalized for any type of technology, since it only presents the distribution of the particles that generate scattering. In [39] and [40], the study of optical wireless scattering modeling is presented as a NLoS component over broad spectra. The modeling approach of these works is based on the concept that air molecules and suspended aerosols help to build optical scattering communication of NLoS links by using near-infrared carriers to visible light and ultraviolet frequency bands. References [41] and [42] are the first works that consider the phenomenon of scattering in typical indoor VLC environments are presented. The authors locate possible scatters around a ring or an ellipse, depending on the number of lightning strikes on the scatterers. The total VLC channel is represented as the arithmetic sum of the LoS channel component and the channel components from the interaction between the optical transmitter, scatterer, and optical receiver.

Although there are several studies on the effect of scattering and shadowing in typical VLC indoor environments, in the authors' opinion, these phenomena have not been widely and properly analyzed in underground mining environments. In this context, only a few VLC channel modeling manuscripts for underground mines consider blocking and dust particles. However, these proposals are not very realistic because they are based on the assumption of the typical indoor VLC channel. These works realistically model the tunnel features nor give a random approach to the physical phenomena present in underground mining scenarios. Furthermore, the reviewed works are limited since they do not analyze the effects that physical phenomena may have on the optical channel by not including them in the

mathematical expression of the underground mining VLC channel model.

Then, in contrast to the studies reported in the literature, we included in the mathematical expressions of the LoS and NLoS components of the proposed underground mining VLC channel model a weighting function to adequately describe the shadowing effect. This function is based on a Poisson process [82], which randomly describes the entry of objects in the underground mining VLC environment. Furthermore, to model the scattering effect, we considered the following premises: (1) The dust particles are uniformly distributed over a disc region centered on the installed PD in the helmet of the mining worker. (2) We consider the interaction of the optical link with the dust particles by modeling it through Mie scattering and Rayleigh scattering theories. Consequently, we derive and present a channel component produced by scattering the optical signal, and its mathematical expression is included in the proposed mathematical model of the VLC channel for underground mines.

Finally, we have made a comparison between the characteristics considered by the main works on VLC channel modeling in underground mines found in the literature and our proposal. This comparison is summarized in Table 2.1. It can be seen that our proposal contemplates the main factors that exist in underground mines and that need to be considered in the channel model.

2.3 Reference VLC Channel Model Applied to Underground Mining

Usually, a closed indoor environment with reflective objects (walls and roof) for optical wireless downlink transmission is considered to model the standard indoor VLC channel. For our case, the geometric configuration of the downlink transmission applied to an ideal (referential) underground mining scenario is illustrated in Figure 5.1, where all its variables and constants will be described below. The VLC channel is the space between the LED and the PD and to model it, three different components must be analyzed: LEDs (light sources), PDs (light detectors), and the light propagation model.

2.3.1 Light Sources

It is assumed that a LED is a point source that follows the Lambertian radiation pattern. Furthermore, the LED is assumed to operate within the linear dynamic range of the current-power characteristic curve and that it is fixed and oriented vertically downwards; its position is given by $(x_{\mathrm{i}}^T, y_{\mathrm{i}}^T, z_{\mathrm{i}}^T)$ in the Cartesian coordinate system. For the remainder of the manuscript, we consider the LED as an optical transmitter T_{i}, which belongs to a set of optical transmitters, where $\mathrm{i} = 1, 2, ..., I$ and I is the total number of optical transmitters. Finally, we assume that each T_{i} has the same generalized Lambertian radiation pattern; therefore, the radiation intensity pattern $R\mathrm{i}(\phi_{\mathrm{i}j})$ can be modeled as follows [65]:

$$R\mathrm{i}(\phi_{\mathrm{i}j}) = \begin{cases} \frac{m+1}{2\pi}\cos^m(\phi_{\mathrm{i}j}) & \text{if } -\pi/2 \leq \phi_{\mathrm{i}j} \leq \pi/2 \\ 0 & \text{otherwise} \end{cases}, \tag{2.1}$$

where $\phi_{\mathrm{i}j}$ is the radiance angle with respect to the normal vector to the T_{i} surface, which is $\boldsymbol{n}_{\mathrm{i}} = [0, 0, -1]$, and $m = -1/log_2\left[cos(\Phi_{\mathrm{i}1/2})\right]$ represents the Lambertian mode number of

Table 2.1: Comparison between the proposed and state-of-art models.

Model	**Characteristics**			
	Tilt/Rotation LED/PD	Non-flat walls	Shadowing	Scattering
Riurean et. al. 2020 [36]	✗	✗	✗	✓
Morales et. al. 2019 [76]	✓	✗	✗	✗
Wang et. al. 2018 [68]	✗	✗	✓	✓
Wang et. al. 2017 [75]	✗	✗	✗	✗
Wang et. al. 2017 [34]	✗	✗	✗	✗
Zhai et. al. 2015 [77]	✗	✗	✗	✓
Our proposal	✓	✓	✓	✓

the T_{i}, which is a function of semi-angle at half power ($\Phi_{\mathrm{i}1/2}$) of the T_{i} [65]. The subscript j of $\phi_{\mathrm{i}j}$ will be defined in Section 2.3.2.

2.3.2 Light Detectors

We assume PDs as light detectors in the reception side of the VLC link. A PD is composed of a non-imaging concentrator (lens) and a physical active area A_p. In addition, for an ideal scenario, the PD may be assumed as fixed and vertically oriented upwards, where its position is represented by (x_j^R, y_j^R, z_j^R) in the Cartesian coordinate system. Hence, we consider the PD as an optical receiver R_j, which belongs to a set of optical receivers where $j = 1, 2, ..., J$ and J is the total number of optical receivers. R_j collects the incident power produced by the light intensity of T_{i}. The effective collection area of the R_j detector acquires the form of [65]

$$A_{\mathrm{e}ff}(\theta_{\mathrm{i}j}) = \begin{cases} A_p cos(\theta_{\mathrm{i}j}) & \text{if } -\Theta/2 \leq \theta_{\mathrm{i}j} \leq \Theta/2 \\ 0 & \text{otherwise} \end{cases}, \tag{2.2}$$

where $\theta_{\mathrm{i}j}$ is the incidence angle with respect to the normal vector to the R_j surface, which is $\boldsymbol{n}_j = [0, 0, 1]$, and Θ is the PD FoV. The optical concentrator gain can be written as $g(\theta_{\mathrm{i}j}) = \eta^2 / sin^2(\Theta)$, being η the internal refractive index of the concentrator [65].

2.3.3 Visible Light Propagation Model

In Sections 2.3.1 and 2.3.2, the mathematical models of the LEDs and PDs were introduced. Here, we use them to derive the reference VLC channel model. In general, the VLC channel is modeled based on two optical components: the LoS component and NLoS component. The LoS component directly results from the LED lighting falling on the PD. Therefore, the LoS link depends on LEDs and PDs parameters as seen above. The DC gain of the LoS optical

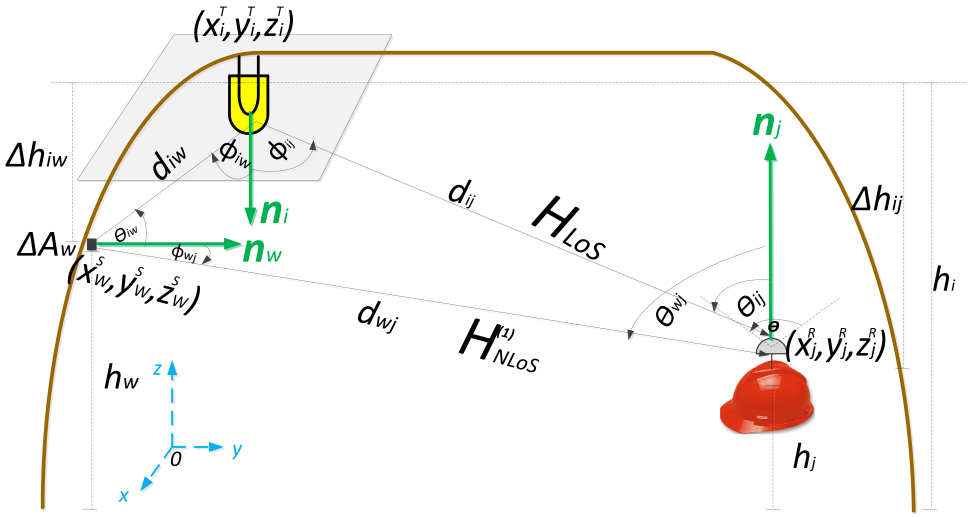

Figure 2.1: Downlink geometry of the light propagation for the reference underground mining scenario.

wireless channel is formulated by merging (2.1) and (2.2) by the following form [65]:

$$H_{LoS}(0; T_{\mathrm{i}}, R_j) = \frac{(m+1)A_p}{2\pi \mathrm{d}_{\mathrm{ij}}^2} \cos^m(\phi_{\mathrm{ij}}) \cos(\theta_{\mathrm{ij}}) G(\theta_{\mathrm{ij}}) \times rect\left(\frac{\theta_{\mathrm{ij}}}{\Theta}\right), \tag{2.3}$$

where $rect\left(\frac{\theta_{\mathrm{ij}}}{\Theta}\right) = 1$ for $0 \leq \theta_{\mathrm{ij}} \leq \Theta$ and 0 otherwise; the Euclidean distance between T_{i} and R_j is denoted by d_{ij}, and $G(\theta_{\mathrm{ij}})$=$T_s(\theta_{\mathrm{ij}})$ $g(\theta_{\mathrm{ij}})$ represents the combined gain of the optical filter and optical concentrator, respectively [65].

On the other hand, as a result of obstacles, indoor wall, and ceiling surfaces, a diffuse component of the transmitted light is reflected by these elements. The sum of these reflections generates the NLoS component of the VLC channel, termed as H_{NLoS}. A common model for diffuse reflection is the Lambertian reflectance where light is reflected with equal radiance in all directions. This model is based on the paradigm that the component $\|\mathrm{H}_{NLoS}^{(k)}\| \to 0$ when $k \to \infty$, where $H_{NLoS}^{(k)}$ is the NLoS component after k bounces, and k is the total number of bounces [65, 70]. This concept implies two generalities: (1) Reflections caused by large number of bounces of k^{th} order would be negligible. (2) The first bounce comes to be the most important component that affects the received power and its temporal dispersion. Therefore, the H_{NLoS} component could be estimated by considering the first bounce, which is known as $H_{NLoS}^{(1)}$.

The DC gain of the NLoS optical wireless channel can be calculated by adding all the

components arriving at the R_j after being reflected in a surface, namely [65]

$$H^{(1)}_{NLoS}(0; T_{\mathrm{i}}, R_j) = \frac{(m+1)A_p}{2\pi} \sum_{w=1}^{W} \frac{\Delta A_w \rho_w}{\mathrm{d}^2_{\mathrm{i}w} \mathrm{d}^2_{wj}} \cos^m(\phi_{\mathrm{i}w}) \times cos(\theta_{\mathrm{i}w}) cos(\phi_{wj}) \cos(\theta_{wj}) G(\theta_{wj}) \times rect\left(\frac{\theta_{wj}}{\Theta}\right), \tag{2.4}$$

where ΔA_w denotes the w^{th} area of the considered reflective element w, whose reflection coefficient and position are respectively represented by ρ_w and (x^S_w, y^S_w, z^S_w). W is the total number of reflective elements considered in the scenario. The incidence angle with respect to the normal vector to the reflective element w ($\boldsymbol{n}_w = [0, 1, 0]$) and the radiance angle of the light component reaching the reflective element w are symbolized with $\theta_{\mathrm{i}w}$ and $\phi_{\mathrm{i}w}$, respectively. The angles of incidence and radiance denoted by θ_{wj} and ϕ_{wj} respectively are measured with respect to the light component that is reflected in the reflective element w and reaches R_j. Finally, the Euclidean distances between T_{i} and the reflective element w, and between the reflective element w and R_j are given by $\mathrm{d}_{\mathrm{i}w}$ and d_{wj}, respectively.

As we mentioned, the analysis of VLC system components that we present in this section focuses on a reference VLC channel model. Therefore, despite applying it to a tunnel, we do not consider intrinsic factors and features of the underground mine. However, this observation gives us a overall framework and naturally leads us to Sections 2.4, 2.5 and 2.6, where we discuss more details about the development of the proposed underground mining VLC channel model. In Section 2.4 we analyze and consider in the underground mining VLC channel model to be proposed, the position characteristics (rotation and tilt) of the system elements (LEDs and PDs), and the effect of the non-regular and non-flat walls of the tunnels. Then, in Section 2.5, we statistically characterize the shadowing and add it to the VLC underground mining channel components derived in Section 2.4. The scattering distribution in the underground mining scenario, its statistical characterization, and its channel component are derived in Section 2.6. At the end of this section, the closed mathematical expression of the proposed underground mining VLC channel model is presented.

2.4 Position Characterization of LEDs and PDs, and Non-Flat Walls Modeling

2.4.1 Tilted and Rotated LEDs and PDs

In a real underground mining scenario, LED luminaries are normally installed on the ceiling or on the walls of the tunnels. To facilitate maintenance and replacement work, the placement of LEDs in the curved sections between the wall and the ceiling of the tunnel is preferred. When we place the T_{i} on the tunnel walls, it normally does not point vertically downwards. A convenient way to describe the orientation of the T_{i} is to use two separate angles that show the tilt and rotation on the axes of the reference coordinate system. The tilt angle with respect to the z-axis is represented by β_{i}, which takes values in range of $[90°, 180°)$ and the rotation angle with respect to the x-axis is denoted as α_{i}, which is defined in the interval $[0°, 360°)$. Both ranges of values are based on the characteristics of the underground

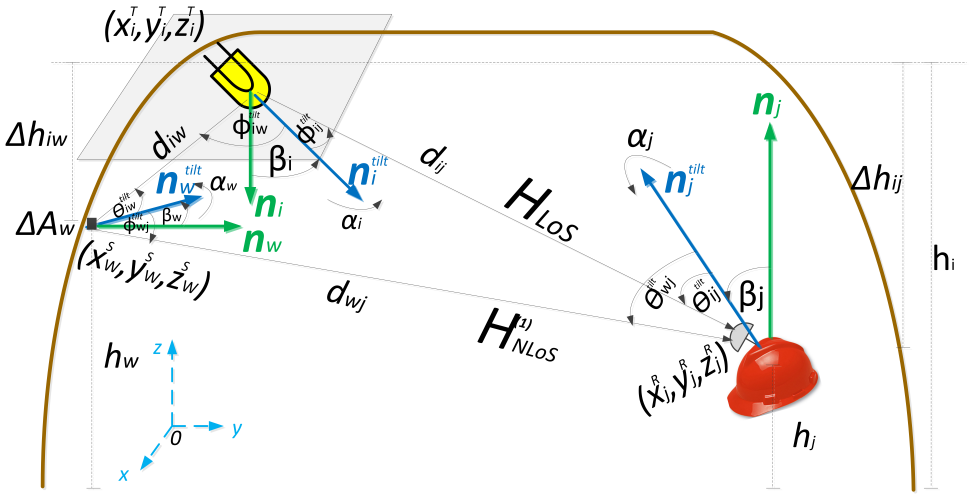

Figure 2.2: Downlink light propagation geometry for the proposed underground mining scenario.

mining scenario and work related to LED positioning [83]-[85]. These elementary angles are represented in Figures 2.2 and 2.3.

It is evident that the orientation of the T_i determines its normal vector $\boldsymbol{n}_\mathrm{i}$. Therefore, $\boldsymbol{n}_\mathrm{i}$ after the tilt and rotation of the T_i is termed by $\boldsymbol{n}_\mathrm{i}^{tilt}$. This orientation also affects $\phi_{\mathrm{i}j}$, which is now denoted as $\phi_{\mathrm{i}j}^{tilt}$. The effect of these considerations is directly distinguished in the term $\cos(\phi_{\mathrm{i}j}^{tilt})$ of the LoS channel component, which is based on the vector concepts as follows:

$$\cos(\phi_{\mathrm{i}j}^{tilt}) = \frac{V_{\mathrm{i}-j} \cdot \boldsymbol{n}_\mathrm{i}^{tilt}}{\|V_{\mathrm{i}-j}\| \|\boldsymbol{n}_\mathrm{i}^{tilt}\|}, \tag{2.5}$$

where the vector from T_i to R_j is denoted by $V_{\mathrm{i}-j}$, the notation $\|\cdot\|$ denotes the 2-norm, and $\cdot$ represents the product dot operation. Also, for vector concepts, $\|V_{\mathrm{i}-j}\| = \mathrm{d}_{\mathrm{i}j}$, $\|\boldsymbol{n}_\mathrm{i}^{tilt}\| = 1$, and $\boldsymbol{n}_\mathrm{i}^{tilt}$ can be represented in terms of α_i and β_i as $\boldsymbol{n}_\mathrm{i}^{tilt} = [\sin(\beta_\mathrm{i})\cos(\alpha_\mathrm{i}), \sin(\beta_\mathrm{i})\sin(\alpha_\mathrm{i}), -\cos(\beta_\mathrm{i})]$. T_i positioning characteristics are shown in Figure 2.3. Notice that the z-component of the $\boldsymbol{n}_\mathrm{i}^{tilt}$ is negative since the T_i is pointing downwards. Furthermore, $V_{\mathrm{i}-j} = \left[x_j^R - x_\mathrm{i}^T, y_j^R - y_\mathrm{i}^T, -\Delta h_{\mathrm{i}j}\right]$, assuming that $\Delta h_{\mathrm{i}j}$ is the difference height between T_i and R_j, that is z_i^T-$z_j^R = \Delta h_{\mathrm{i}j}$. Consequently, the expression (2.5) can be rewritten in the following form:

$$\cos(\phi_{\mathrm{i}j}^{tilt}) = \frac{\left[x_j^R - x_\mathrm{i}^T, y_j^R - y_\mathrm{i}^T, -\Delta h_{\mathrm{i}j}\right]}{\mathrm{d}_{\mathrm{i}j}} \cdot \left[\sin(\beta_\mathrm{i})\cos(\alpha_\mathrm{i}), \sin(\beta_\mathrm{i})\sin(\alpha_\mathrm{i}), -\cos(\beta_\mathrm{i})\right]. \tag{2.6}$$

On the other hand, when we install R_j in the helmets of the mining workers, R_j does not always point vertically upward due to the nature of the person's head movement. As in T_i, the orientation of R_j can be described by using the angles of tilt and rotation on the reference coordinate system. Here, the tilt angle with respect to the z-axis is denoted as β_j, which takes values in range of $[0°, 90°)$, and the rotation angle with respect to the x-axis is denoted with α_j that can be values in range of $[0°, 180°)$. Both range of values are based on the characteristics of the underground mining scenario, the range of motion of a person's head, and works related to PD positioning [86]-[88]. These angles are displayed in Figures 2.2 and 2.4 for clarification purposes.

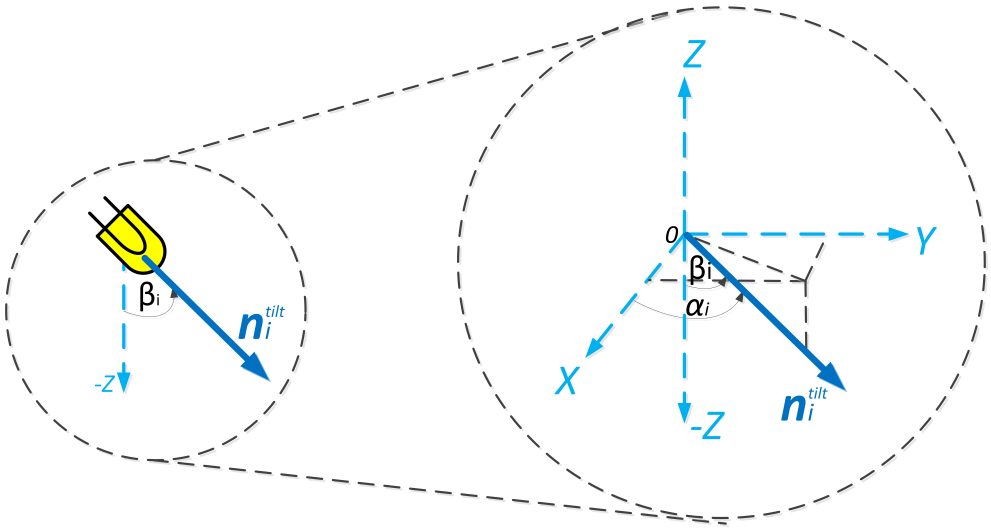

Figure 2.3: Transmitter position characteristics.

The previous considerations for the orientation of R_j change its $\boldsymbol{n}_j$ and $\theta_{\mathrm{i}j}$, which are now denoted as $\boldsymbol{n}_j^{tilt}$ and $\theta_{\mathrm{i}j}^{tilt}$, respectively. Furthermore, this effect is directly noticeable in the term $\cos(\theta_{\mathrm{i}j}^{tilt})$ of the LoS channel component, which is based on the vector concepts as follows:

$$\cos(\theta_{\mathrm{i}j}^{tilt}) = \frac{V_{j-\mathrm{i}} \cdot \boldsymbol{n}_j^{tilt}}{\|V_{j-\mathrm{i}}\| \|\boldsymbol{n}_j^{tilt}\|}, \tag{2.7}$$

where $V_{j-\mathrm{i}}$ is the vector from R_j to T_i. For vector concepts, we also consider that $\|V_{j-\mathrm{i}}\| = \mathrm{d}_{\mathrm{i}j}$, $\|\boldsymbol{n}_j^{tilt}\| = 1$, $\boldsymbol{n}_j^{tilt} = [\sin(\beta_j)\cos(\alpha_j), \sin(\beta_j)\sin(\alpha_j), \cos(\beta_j)]$, and $V_{j-\mathrm{i}} = \left[x_\mathrm{i}^T - x_j^R, y_\mathrm{i}^T - y_j^R, \Delta h_{\mathrm{i}j}\right]$ as can be seen in Figure 2.4. Consequently, the expression (2.7) can be rewritten as

$$\cos(\theta_{\mathrm{i}j}^{tilt}) = \frac{\left[x_\mathrm{i}^T - x_j^R, y_\mathrm{i}^T - y_j^R, \Delta h_{\mathrm{i}j}\right]}{\mathrm{d}_{\mathrm{i}j}} \cdot [\sin(\beta_j)\cos(\alpha_j), \sin(\beta_j)\sin(\alpha_j), \cos(\beta_j)]\,. \tag{2.8}$$

Finally, in order to include the effect of the orientation of T_i and R_j in the proposed underground mining VLC channel model, we replace the expressions (2.6) and (2.8) in the mathematical expression of the LoS channel component expressed in (2.3) to obtain a precise model for H_{LoS} that is given by (2.9).

$$\begin{aligned} H_{LoS}(0; T_\mathrm{i}, R_j) = \frac{(m+1)A_p}{2\pi \mathrm{d}_{\mathrm{i}j}^{m+3}} &\left\{\left[x_j^R - x_\mathrm{i}^T, y_j^R - y_\mathrm{i}^T, -\Delta h_{\mathrm{i}j}\right] \cdot [\sin(\beta_\mathrm{i})\cos(\alpha_\mathrm{i}), \sin(\beta_\mathrm{i})\sin(\alpha_\mathrm{i}), -\cos(\beta_\mathrm{i})]\right\}^m \\ &\times \left\{\left[x_\mathrm{i}^T - x_j^R, y_\mathrm{i}^T - y_j^R, \Delta h_{\mathrm{i}j}\right] \cdot [\sin(\beta_j)\cos(\alpha_j), \sin(\beta_j)\sin(\alpha_j), \cos(\beta_j)]\right\} G(\theta_{\mathrm{i}j}^{tilt}) rect\left(\frac{\theta_{\mathrm{i}j}^{tilt}}{\Theta}\right). \end{aligned} \tag{2.9}$$

2.4.2 Non-Flat and Non-Regular Tunnel Walls

Usually, in the modeling of reflective elements for traditional interior environments such as offices and hospitals, the walls are considered as ideal reflective elements. Among the ideal features assumed can be mentioned: perpendicularity with respect to the ceiling, regularity, and flat surface. However, these assumptions do not make sense in underground mines since

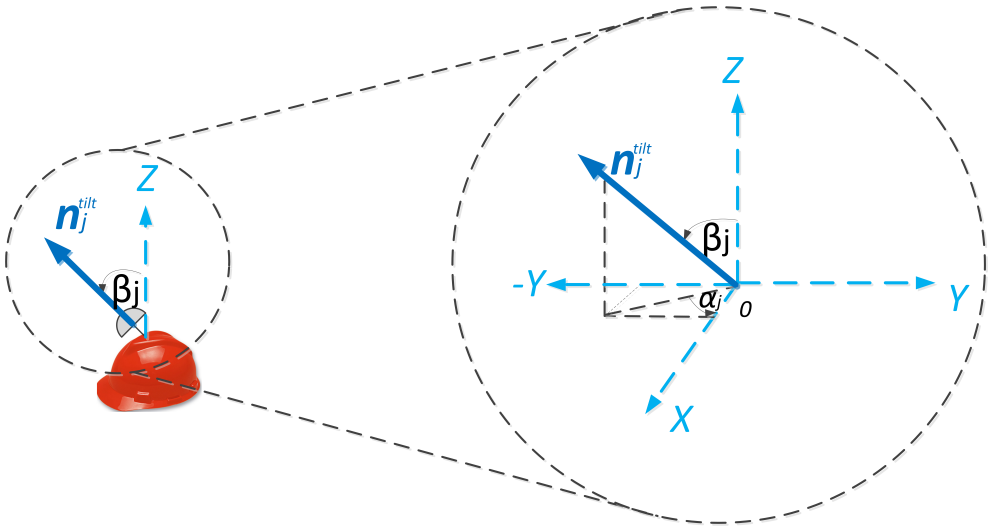

Figure 2.4: Receiver position characteristics.

most tunnels are U-shaped, irregular, and non-flat. Therefore, it is necessary to adequately model the effect of the tunnel walls to include them in the proposed underground mining VLC channel model and analyze their impact on system performance.

As mentioned in Section 2.3.3, each reflective element is modeled with the Lambertian reflectance, so each of them can be considered as a Lambertian point source. However, in the underground mining context, the irregularity of the surface of each reflective element implies that the radiation intensity of this source and the direction of the reflected light are not deterministic. Additionally, in ideal reflective elements, their normal vectors are orthogonal to their surfaces and everyone pointing in the same direction. This situation does not occur in a underground mining scenario. Here, each reflective element has an irregular surface. Therefore, their normal vectors are not orthogonal to their surface, and they point in different directions.

As happened with the normal vectors described in Section 2.4.1, the normal vector $\boldsymbol{n}_w$ of each reflective element w can be described in terms of their tilt and rotation angles on the axes of the reference coordinate system. Here, the tilt angle with respect to the z-axis is denoted as β_w, which belongs to the range of $[0°, 180°)$ and the rotation angle with respect to the x-axis is denoted as α_w and takes values in range of $[0°, 180°)$. Both intervals are based on the characteristics and limitations that exist in a underground mining scenario (see Figure 2.2).

The introduced features for the orientation of each reflective element w changes its normal vector $\boldsymbol{n}_w$, and its angles $\theta_{\mathrm{i}w}$ and ϕ_{wj}, which are now termed by $\boldsymbol{n}_w^{tilt}$, $\theta_{\mathrm{i}w}^{tilt}$ and ϕ_{wj}^{tilt}, respectively. Additionally, the tilt and rotation of T_{i} and R_j affects this channel component in terms of the angles $\phi_{\mathrm{i}w}$ and θ_{wj}, which are redefined by $\phi_{\mathrm{i}w}^{tilt}$ and θ_{wj}^{tilt}, respectively. Therefore, the irregular walls of the tunnels along with the orientation of T_{i} and R_j directly affect the NLoS component of the underground mining VLC channel.

The effect of these considerations is noticeable in terms of the following cosines: $\cos(\phi_{\mathrm{i}w}^{tilt})$,

$\cos(\theta_{\mathrm{i}w}^{tilt})$, $\cos(\phi_{wj}^{tilt})$ and $\cos(\theta_{wj}^{tilt})$ in the following form:

$$\cos(\phi_{\mathrm{i}w}^{tilt}) = \frac{V_{\mathrm{i}-w} \cdot \boldsymbol{n}_{\mathrm{i}}^{tilt}}{\|V_{\mathrm{i}-w}\|\|\boldsymbol{n}_{\mathrm{i}}^{tilt}\|}, \tag{2.10}$$

where $V_{\mathrm{i}-w}$ is the vector from T_{i} to w, $\|V_{\mathrm{i}-w}\| = \mathrm{d}_{\mathrm{i}w}$, and $V_{\mathrm{i}-w} = \left[x_w^S - x_{\mathrm{i}}^T, y_w^S - y_{\mathrm{i}}^T, -\Delta h_{\mathrm{i}w}\right]$, assuming that $\Delta h_{\mathrm{i}w}$ is the difference height between T_{i} and w.

$$\cos(\theta_{\mathrm{i}w}^{tilt}) = \frac{V_{w-\mathrm{i}} \cdot \boldsymbol{n}_{w}^{tilt}}{\|V_{w-\mathrm{i}}\|\|\boldsymbol{n}_{w}^{tilt}\|}, \tag{2.11}$$

where $V_{w-\mathrm{i}}$ is the vector from w to T_{i}, $\|V_{w-\mathrm{i}}\| = \mathrm{d}_{\mathrm{i}w}$, $\|\boldsymbol{n}_{w}^{tilt}\|$=1, $\boldsymbol{n}_{w}^{tilt}$ can be represented in terms of α_w and β_w, that is $\boldsymbol{n}_{w}^{tilt} = [\sin(\beta_w)\cos(\alpha_w), \sin(\beta_w)\sin(\alpha_w), \cos(\beta_w)]$ and $V_{w-\mathrm{i}} = \left[x_{\mathrm{i}}^T - x_w^S, y_{\mathrm{i}}^T - y_w^S, \Delta h_{\mathrm{i}w}\right]$.

$$\cos(\phi_{wj}^{tilt}) = \frac{V_{w-j} \cdot \boldsymbol{n}_{w}^{tilt}}{\|V_{w-j}\|\|\boldsymbol{n}_{w}^{tilt}\|}, \tag{2.12}$$

where V_{w-j} is the vector from w to R_j, $\|V_{w-j}\|$=d_{wj}, and $V_{w-j} = \left[x_j^R - x_w^S, y_j^R - y_w^S, -\Delta h_{wj}\right]$, assuming that Δh_{wj} is the difference height between w and R_j.

$$\cos(\theta_{wj}^{tilt}) = \frac{V_{j-w} \cdot \boldsymbol{n}_{j}^{tilt}}{\|V_{j-w}\|\|\boldsymbol{n}_{j}^{tilt}\|}, \tag{2.13}$$

where V_{j-w} is the vector from R_j to w, $\|V_{j-w}\| = \mathrm{d}_{wj}$, and $V_{j-w} = \left[x_w^S - x_j^R, y_w^S - y_j^R, \Delta h_{wj}\right]$.

All the previous definitions allow us to reform the expressions (**??**), (2.11), (2.12), and (2.13). Finally, in order to include the effect of non-regular walls of the tunnels in the proposed underground mining VLC channel model, we replace these new expressions in the mathematical model of the NLoS channel component expressed in (2.4). As a consequence, we obtain an exact expression for $H_{NLoS}^{(1)}$ given by (2.14).

$$\begin{aligned} H_{NLoS}^{(1)}(0; T_{\mathrm{i}}, R_j) = {} & \frac{(m+1)A_p}{2\pi} \sum_{w=1}^{W} \frac{\Delta A_w \rho_w}{\mathrm{d}_{\mathrm{i}w}^{m+3} \mathrm{d}_{wj}^4} \\ & \times \left\{ \left[x_w^S - x_{\mathrm{i}}^T, y_w^S - y_{\mathrm{i}}^T, -\Delta h_{\mathrm{i}w}\right] \cdot [\sin(\beta_{\mathrm{i}})\cos(\alpha_{\mathrm{i}}), \sin(\beta_{\mathrm{i}})\sin(\alpha_{\mathrm{i}}), -\cos(\beta_{\mathrm{i}})] \right\}^m \\ & \times \left\{ \left[x_{\mathrm{i}}^T - x_w^S, y_{\mathrm{i}}^T - y_w^S, \Delta h_{\mathrm{i}w}\right] \cdot [\sin(\beta_w)\cos(\alpha_w), \sin(\beta_w)\sin(\alpha_w), \cos(\beta_w)] \right\} \\ & \times \left\{ \left[x_j^R - x_w^S, y_j^R - y_w^S, -\Delta h_{wj}\right] \cdot [\sin(\beta_w)\cos(\alpha_w), \sin(\beta_w)\sin(\alpha_w), \cos(\beta_w)] \right\} \\ & \times \left\{ \left[x_w^S - x_j^R, y_w^S - y_j^R, \Delta h_{wj}\right] \cdot [\sin(\beta_j)\cos(\alpha_j), \sin(\beta_j)\sin(\alpha_j), \cos(\beta_j)] \right\} \\ & \times G(\theta_{wj}^{tilt}) rect\left(\frac{\theta_{wj}^{tilt}}{\Theta}\right). \end{aligned} \tag{2.14}$$

2.5 Statistical Shadowing Model Caused by Random Obstructions

A physical phenomenon that particularly conditions wireless communication links in underground mining environments is shadowing due to its great dependence on having a line of

sight, by affecting the system performance. Because of the underground mining infrastructure, in which there are large machinery and vehicles that move by the tunnels, the effect of shadowing must be considered in order to derive a reasonable underground mining VLC channel model.

In our shadowing study, we are assuming that the PD is mounted on the miners' helmet. Therefore, due to the location of T_{i}, we do not consider the shadowing effect that could occur when miners (human obstacles) block the VLC link. Because of the real characteristics of the tunnels, we only consider the optical link blockage caused by vehicles and obstacles moving along the tunnels.

2.5.1 Assumptions Considered to Model Shadowing Statistically

Shadowing comes from non-quantitative obstructions (vehicles and obstacles) that randomly enter to the underground mining area with particular characteristics (size, position, income intensity, etc.). In addition, we consider that numerous LEDs illuminate the work area in underground mines completely. Therefore, it is impossible for all optical links to be completely blocked. However, vehicles entering the underground mining area can block certain optical links and partially attenuate the transmitted signal strength.

According to the literature, shadowing applied to VLC systems has been modeled as a binomial Gaussian distribution [68] and as a Poisson process [82]. After a comparative analysis of models that fit the real characteristics of the shadowing phenomenon in underground mines, we follow and extrapolate to our analysis a statistical methodology for shadowing modeling [82]. This approach utilizes a Poisson process to describe the appearance of obstructions in the VLC environment, a probability density function to characterize the size and position of the obstructions, such as vehicles or heavy machinery, and a weighting function to describe the shadowing effect. The weighting function will be described in detail and derived in Section 2.5.3.

2.5.2 Description of the Underground Mining Scenario with Optical Link Blocking

We consider a VLC link obstruction/non-obstruction underground mining scenario as shown in Figure 2.5. In order to easily represent the underground mining environment and without losing the generality, we assume that the tunnel area to be analyzed is cubic with the following dimensions: length (X), width (Y), and height (Z). For a better description of the scenario, we consider a line segment AB, where the point A is the Cartesian coordinate where T_{i} is located and the point B is the Cartesian coordinate where R_j is located. We observe that the magnitude of line segment AB matches to the magnitude of $\mathrm{d}_{\mathrm{i}j}$.

For our model, we discard the thickness of the obstruction and consider the point V, whose coordinates are represented by $(x_v, y_v, 0)$, as the midpoint of the projection of the obstruction in the x-y plane. Furthermore, the line segment CD represents the projection of line segment AB in the x-y plane, whose coordinates of the points C and D are $(x_{\mathrm{i}}^T, y_{\mathrm{i}}^T, 0)$, $(x_j^R, y_j^R, 0)$ respectively. Finally, we consider a perpendicular line segment to CD from the point $(x_v, y_v, 0)$ with the point E being the foot point and, thus, we construct a line EF

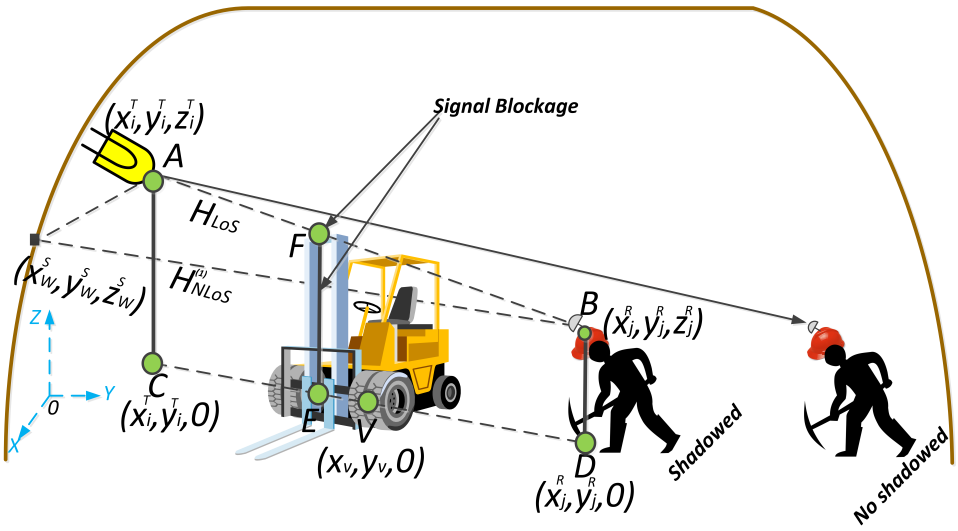

Figure 2.5: Schematic diagram of the AB optical link being blocked by a mobile obstruction with width w_v and height h_v.

parallel to the z-axis through point E, where the point F denotes the intersecting point with the segment AB.

2.5.3 Proposed Statistical Shadowing Model

Based on the work presented in [82], we statistically model the entry of obstructions into the underground mining environment and, consequently, the shadowing produced considering the following statistical assumptions: (1) We assume that there are not obstructions in the scenario at the beginning time. (2) For the no-shadowed case, VLC channel components are not affected. On the other hand, for the shadowed situation, a weighting function $P_{\mathrm{i}j}$ is introduced to describe the random shadowing. $P_{\mathrm{i}j}$ describes the probability that the LoS optical link is not blocked. (3) We assume the entry of obstructions to the underground mining area as a Poisson process N_t with an intensity parameter ϵ. Furthermore, each obstruction is independently and identically distributed with its own dimensions (width w_o and height h_o) and position (x_o , y_o). Therefore, the blocking or not of the optical link that the obstacles can cause are independent of each other. (4) We denote possible obstructions entering the scenario within a period of time t as (w_1, h_1, x_1, y_1), (w_2, h_2, x_2, y_2),...,$(w_{N_t}, h_{N_t}, x_{N_t}, y_{N_t})$. (5) We denote p_v as the probability that the LoS optical link (line segment AB) is blocked by (w_v, h_v, x_v, y_v) where v takes values from 1 to N_t and p_1, p_2,..., p_{N_t} are independent and identically distributed. Consequently, $P_{\mathrm{i}j}$ can be written as [82]

$$P_{\mathrm{i}j} = \exp\left[-\epsilon E(p_v)t\right], \tag{2.15}$$

where $E(p_v)$ is the expected value of p_v. Now, we must find the specific physical and geometric conditions that mathematically demonstrate when the optical link is blocked by some obstruction (w_v, h_v, x_v, y_v). Based on the geometry of Figure 2.5, we can summarize two main conditions [82]: (1) Half of w_v must be greater than or equal to the distance from the point (x_v, y_v) to the segment CD, namely $w_v/2 \geq \mathrm{d}(x_v, y_v)$. (2) h_v must be greater than or equal to the length of EF, namely $h_v \geq s(x_v, y_v)$.

Since the coordinates of the points A and B are known, we can formulate the expressions of $\mathrm{d}(x_v, y_v)$ and $s(x_v, y_v)$ as follows:

$$\mathrm{d}(x_v, y_v) = \frac{|(y_{\mathrm{i}}^T - y_j^R)x_v - (x_{\mathrm{i}}^T - x_j^R)y_v - x_j^R y_{\mathrm{i}}^T + x_{\mathrm{i}}^T y_j^R|}{\sqrt{(y_{\mathrm{i}}^T - y_j^R)^2 + (x_{\mathrm{i}}^T - x_j^R)^2}}, \tag{2.16}$$

$$\begin{aligned} s(x_v, y_v) = &\frac{(y_{\mathrm{i}}^T - y_j^R)^2 + (x_{\mathrm{i}}^T - x_j^R)^2 + (x_v - x_j^R)^2}{2\sqrt{(y_{\mathrm{i}}^T - y_j^R)^2 + (x_{\mathrm{i}}^T - x_j^R)^2}} \\ &+ \frac{(y_v - y_j^R)^2 - [(x_v - x_{\mathrm{i}}^T)^2 + (y_v - y_{\mathrm{i}}^T)^2]}{2\sqrt{(y_{\mathrm{i}}^T - y_j^R)^2 + (x_{\mathrm{i}}^T - x_j^R)^2}} + z_j^R. \end{aligned} \tag{2.17}$$

$$E(p_v) = \int_0^X \int_0^Y \left[\int\int_{\{(w,h):w \geq 2\mathrm{d}(x,y), h \geq s(x,y)\}} g_v(w,h)\mathrm{d}w \ \mathrm{d}h \right] f_v(x,y)\mathrm{d}x \ \mathrm{d}y, \tag{2.18}$$

$$P_{\mathrm{i}j} = \exp\left\{ -\epsilon \left\{ \int_0^X \int_0^Y \left[\int\int_{\{(w,h):w \geq 2\mathrm{d}(x,y), h \geq s(x,y)\}} g_v(w,h)\mathrm{d}w \ \mathrm{d}h \right] f_v(x,y)\mathrm{d}x \ \mathrm{d}y \right\} \ t \right\}. \tag{2.19}$$

As the entry of possible obstructions to the tunnel is not deterministic, we denote functions of joint probability density for w_v and h_v as $g_v(w,h)$ and for x_v and y_v as $f_v(x,y)$, respectively. It is worth noting that these joint probability density functions can be adapted and chosen depending on the actual situation of the scenario to be modeled, in our case, the underground mining scenario. Consequently, $E(p_v)$ and $P_{\mathrm{i}j}$ are presented in (2.18) and (2.19) [82].

Finally, we include the shadowing characterization and its effect in the LoS channel component expressed in (2.9) by including the weighted function $P_{\mathrm{i}j}$ in its mathematical expression. In addition, we also consider the shadowing effect in the NLoS channel component expressed in (2.14) by including the weighted functions $P_{\mathrm{i}w}$ and P_{wj} in its mathematical expression. These weighted functions are obtained through the same statistical process to obtain $P_{\mathrm{i}j}$ and they represent possible blockages in the optical link between T_{i} and the reflective element w, and the optical link between w and R_j, respectively. Therefore, the new mathematical expressions obtained by multiplying the LoS an NLoS channel components by their corresponding weighting function are denoted as $H_{LoS_{(sh)}}$ and $H^{(1)}_{NLoS_{(sh)}}$ respectively, and expressed as follows:

$$H_{LoS_{(sh)}}(0; T_{\mathrm{i}}, R_j) = H_{LoS}(0; T_{\mathrm{i}}, R_j)P_{\mathrm{i}j}, \tag{2.20}$$

$$H^{(1)}_{NLoS_{(sh)}}(0; T_{\mathrm{i}}, R_j) = H^{(1)}_{NLoS}(0; T_{\mathrm{i}}, R_j)P_{\mathrm{i}w}P_{wj}. \tag{2.21}$$

2.6 Statistical Scattering Model Produced by Dust Particles

In general, the scattering produced by the suspended dust is generally despicable in traditional indoor environments, such as offices, hospitals, or non-dangerous industries. Therefore,

in these scenarios, VLC systems are not generally affected by dust particles. Instead, in underground mines, large amounts of dust are originated by crushing, grinding, flying, and drilling the rock within the mine. Hence, it is necessary to model the scattering effect and introduce it into the underground mining VLC channel model. Consequently, we perform an in-depth analysis to derive the appropriate mathematical model that fits this physical phenomenon.

We propose a stochastic model that provides a simple physical interpretation but in accordance with the real characteristics of the underground mining scenarios. The model that we introduce is based on the theory of absorption and dispersion of photons that travel through the atmosphere. Also, we model the distribution of the scatterers elements (dust particles) based on the Unified Disk Scattering Model (UDSM), which is revealed in [38]. This model allows us to control the distribution of the scatterers by using a factor, which controls the concentration pattern of the scatterers.

2.6.1 Scatterers Distribution Model Considerations

The outline of the scatterers distribution, as well as the geometric considerations that we adopt in our analysis, are displayed in Figure 2.6. By considering the underground mining environment, we assume that at the beginning, T_{i} is free of scatterers to their surroundings and the height where they are positioned is greater than the height where R_j is located. Furthermore, we assume that the scatterers are randomly and independently distributed within a disk-shaped area of radio R_r centered on R_j. These scatterers are called local scatterers.

We consider that within the disk centered on R_j, there are numerous local scatterers S_n, where $n = 1, 2, ..., N$. Theoretically, the number of scatters N could tend to infinite. The location of each local scatterer is represented by its polar coordinates as (r_n, θ_{S_n-j}), where r_n is the distance from the n^{th} local scatterer to R_j and θ_{S_n-j} represents the angle between the distance vector from the n^{th} local scatterer to R_j and $\boldsymbol{n}_j^{tilt}$. Owing to the high path loss that occurs in VLC systems, we discarded the contribution of scatterers outside the assumed disk-shaped area (remote scatterers). Furthermore, we assume that the light beam from the optical link transmitted from T_{i} travels through the atmosphere, impacts some of the local scatterers, and reaches R_j after a single bounce.

After the optical signal hits the local scatterer, it can be absorbed or dispersed. Therefore, R_j could receive signals from diverse directions, which are only determined by the distribution of local scatterers. We define the Euclidean distance of the transmitted optical link between T_{i} and S_n as $\mathrm{d}_{\mathrm{i}-S_n}$ and the radiance angle between the T_{i} and S_n as $\phi_{\mathrm{i}-S_n}$. Therefore, we can describe the Probability Distribution Function (PDF) of the UDSM as follows [38]:

$$p_{r_n}(r_n, \theta_{S_n-j}) = \begin{cases} \frac{(a+1)(r_n)^a}{2\pi R_r^{(a+1)}}, & \text{if } -\pi \leq \theta_{S_n-j} \leq \pi \\ & \text{and } 0 < r_n \leq R_r \\ 0 & \text{otherwise} \end{cases}, \tag{2.22}$$

where $a \geq 0$ is the shape factor that corresponds to a real value. This value controls the distribution of the scatterers within the disk-shaped area (see Figure 2.6). The UDSM

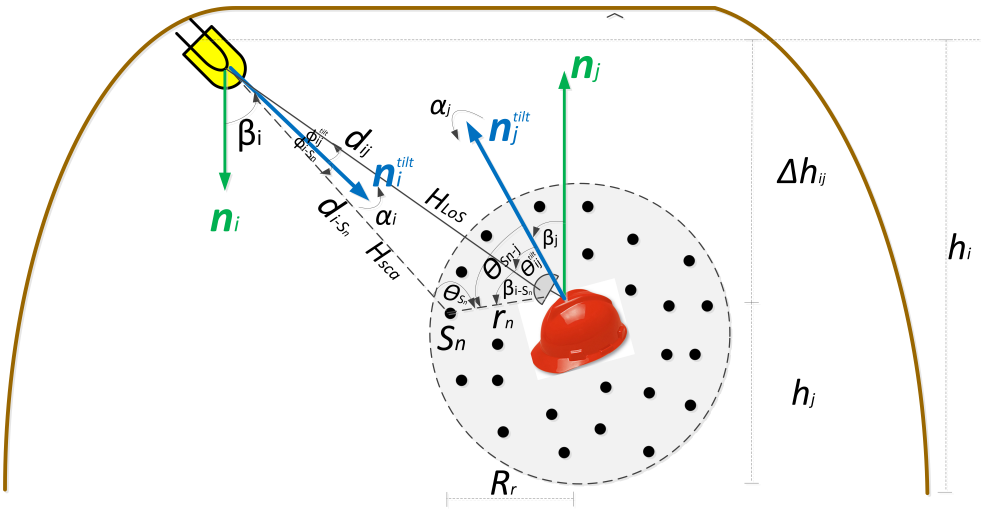

Figure 2.6: Outline of the geometric scattering pattern.

generally depends on r_n, except for $a = 0$ and θ_{S_n-j} is uniformly distributed in the interval $[-\pi, \pi]$. In other words, the UDSM obeys to a circularly symmetric scattering model. For an specific R_r, we can choose values of a between 0 and 1, which only includes scatterers near to R_j and is useful for modeling urban and suburban propagation areas. Due to the real characteristics of the underground mine and the work carried out inside it, we obtain a purely uniform distribution of the scatterers by fixing a to 1. Therefore, the expression (2.22) acquires the form of

$$p_{r_n}(r_n, \theta_{S_n-j}) = \begin{cases} \frac{r_n}{\pi R_r^2}, & \text{if} -\pi \leq \theta_{S_n-j} \leq \pi \\ & \text{and } 0 < r_n \leq R_r \\ 0 & \text{otherwise} \end{cases} . \tag{2.23}$$

Notice that if the value of a increases, the scatterers are concentrated in a hollow disk-shaped area centered on R_j.

2.6.2 Analysis of the Interaction between the Optical Link and Local Scatterers

To characterize the effect of the interaction between the optical link and local scatterers, we assume a scenario where the light ray emitted by T_{i} travels through the atmosphere, interacts with S_n effective scatterers, and reaches R_j. To derive a generalized theoretical approach, we present a reference model based on the assumption that the number of local scatterers can tend to infinity, $(N \to \infty)$. Consequently, the total diffuse channel components produced by the scattered signals can be represented as a superposition of an infinite number of plane waves coming from different directions determined by the distribution of the local scatterers. We assume that each scatterer S_n introduces a coefficient G_n. This gain is inversely proportional to N and directly proportional to the average of the dust particle reflection coefficient $\overline{\rho_s}$, that is, $G_n = \overline{\rho_s}/N$.

As the light beam (photons) after leaving T_{i} travels through the atmosphere, we can

model the interaction of light with dust particles in the atmosphere as a combination of light absorption and scattering events [39, 40], whose coefficients of absorption and dispersion are represented by k_a and k_s, respectively. It is important to mention that when a photon is absorbed by some dust particle, it is annihilated and does not reach the R_j. Therefore the coefficient k_a is not considered in our analysis.

On the other hand, when a light link collides with a dust particle and it scatters, its path is altered before continuing to travel through the atmosphere, as can be see in Figure 4.2. Therefore, the coefficient k_s must be considered in the analysis. To describe this path change in a stochastic way, we consider the pair of angles $(\phi_{\mathrm{i}-S_n}, \theta_{S_n})$, where $\phi_{\mathrm{i}-S_n}$ is the radiance angle measured between $\boldsymbol{n}_{\mathrm{i}}^{tilt}$ and the vector from T_{i} to S_n, and θ_{S_n} is the scattering angle. To validate these considerations, we must obtain the PDF of the phase function that describes the angular distribution of the scattered optical power.

This phase function can be modeled as a weighted combination of the generalized Rayleigh scattering phase function p_{ray} and the phase function based on the Mie scattering theory, represented by the generalized Henyey-Greenstein function p_{mie}. In particular, for $0 \leq \phi_{\mathrm{i}-S_n} \leq \pi/2$ and $0 \leq \theta_{S_n} \leq \Theta$, these functions are expressed as [39, 40]

$$p_{ray}(\mu) = \frac{3[1 + 3\gamma + (1-\gamma)\mu^2]}{16\pi(1+2\gamma)}, \tag{2.24}$$

$$p_{\mathrm{mie}}(\mu) = \frac{1-g^2}{4\pi}\left[\frac{1}{\sqrt{(1+g^2-2g\mu)^3}} + \frac{f(3\mu^2-1)}{2\sqrt{(1+g^2)^3}}\right], \tag{2.25}$$

where $\mu = cos(\theta_{S_n})$, and γ, g and f are atmospheric model parameters.

The contribution that the scattering generates is determined in terms of the type of dust particle according to its diameter. This contribution is governed by atmospheric composition and modeled by the weighting parameters k_r and k_m, which are Rayleigh scattering and Mie scattering coefficients, respectively. In addition, we know that k_s=k_r+k_m [39, 40]. The interaction of these phase functions follows a Bernoulli distribution, i.e. the probability that the photon is modeled as p_{ray} is k_r/k_s and the probability that the photon is modeled as p_{mie} is k_m/k_s. Therefore, the overall phase function along with its respective PDF is given by [39, 40]

$$p_{total}(\mu) = \frac{k_r}{k_s}p_{ray}(\mu) + \frac{k_m}{k_s}p_{\mathrm{mie}}(\mu), \tag{2.26}$$

$$f_{sca}(\mu) = p_{total}(\mu)\sin(\mu). \tag{2.27}$$

Finally, G_n is redefined as $G_n(\mu) = \overline{\rho_s} f_{sca}(\mu)/N$.

2.6.3 Proposed Channel Model Considering the Effects of Scattering

Based on the mathematical expression of the typical Lambertian channel model, we present the channel model produced by scattering on the optical path T_{i}-S_n-R_j, which corresponds to the light beam that travels from T_{i}, interacts with the local scatterrer S_n and reaches R_j. In

this context, the DC gain mathematical expression of the scattering optical wireless channel can be written as

$$H_{sca}(0;T_{\mathrm{i}},S_n,R_j)=\lim_{N\to\infty}\sum_{n=1}^{N}\frac{A_p(m+1)G_n(\mu)}{2\pi D_{\mathrm{i}-n-j}^2}\cos^m(\phi_{\mathrm{i}-S_n})\cos(\theta_{S_n-j})rect\left(\frac{\theta_{S_n-j}}{\Theta}\right), \quad (2.28)$$

where the path length $D_{\mathrm{i}-n-j}$ represents the total distance that light travels from the T_{i} via S_n to the R_j and can be expressed as $D_{\mathrm{i}-n-j}=\mathrm{d}_{\mathrm{i}-S_n}+r_n$. Furthermore, based on the geometry of the Figure 2.6, the expression $\mathrm{d}_{\mathrm{i}-S_n}$ can be determined by using the law of cosines as follows:

$$\mathrm{d}_{\mathrm{i}-S_n}=\sqrt{r_n^2+\mathrm{d}_{\mathrm{ij}}^2-2r_n\mathrm{d}_{\mathrm{ij}}\cos\left(\beta_{\mathrm{i}-S_n}\right)}, \quad (2.29)$$

where $\beta_{\mathrm{i}-S_n}$ denotes the difference between the angles $\theta_{\mathrm{i}-S_n}$ and $\theta_{\mathrm{ij}}^{tilt}$. The value of $\beta_{\mathrm{i}-S_n}$ depends on the value of these angles and the position of the S_n in the following form:

$$\beta_{\mathrm{i}-S_n}=\begin{cases}\theta_{S_n-j}-\theta_{\mathrm{ij}}^{tilt} & \text{if } \theta_{\mathrm{ij}}^{tilt}<\theta_{S_n-j}\\ \theta_{\mathrm{ij}}^{tilt}-\theta_{S_n-j} & \text{otherwise}\end{cases}. \quad (2.30)$$

To conclude, we now present the general expression of the proposed underground mining VLC channel DC gain as follows:

$$H_{miner}(0;T_{\mathrm{i}},R_j)=H_{LoS_{(sh)}}(0;T_{\mathrm{i}},R_j)+H_{NLoS_{(sh)}}^{(1)}(0;T_{\mathrm{i}},R_j)+H_{sca}(0;T_{\mathrm{i}},S_n,R_j). \quad (2.31)$$

The general expression of the underground mining VLC channel model is formed by the addition of expressions (2.20), (2.21), and (2.28). Therefore, we fulfill the objective of including in a single expression all the intrinsic factors of the underground mining scenarios.

2.7 Results and Analysis

In this section, we simulate the CIR, RMS delay spread, and received power based on the proposed underground mining VLC channel model. For the simulation, we choose a tunnel section of dimensions 6m × 3m × 5m. In our analysis, but without losing the generality, we consider a single transmitter and a single receiver, T_1 and R_1, respectively. R_1 is installed on the helmet of mining workers. For a better comparison of the results, an ideal (reference) underground mining scenario and a more realistic (proposed) underground mining scenario are simulated, where the reference VLC channel model and the proposed VLC channel model are included, respectively. These scenarios and their parameters are specified in Table 2.2. Other system parameters are listed in Table 2.3.

As the benchmark situation, a reference underground mining scenario is simulated and then compared to the proposed underground mining scenario to discuss and highlight their differences. As mentioned in Section 2.3, the ideal scenario only considers the LoS channel component and the NLoS components produced by reflections in the walls. Here, two walls are considered to represent the side walls of the tunnel, which are assumed flat and regular. T_1 is installed pointing downwards and R_1 is installed pointing upwards, both located in

fixed positions on the tunnel. Finally, in this scenario, neither the shadowing effect nor the scattering effect are considered.

Instead, in the proposed underground mining scenario, we consider five different positions of R_1 in the tunnel. These locations represent the most likely positions that mining workers could have in the tunnel according to their general work area. It should be emphasized that these positions are referential since we assume a single LED and a fixed PD position only to verify the feasibility of the proposed VLC channel model. Generally in underground mines, distributed LED array lighting sources composed of several LEDs are used. In addition, multiple of these LED arrays are distributed throughout the tunnel. Therefore, we would only need superpose all the solutions induced by each LED in order to get the analysis of the total tunnel. Due to the considered characteristics of the proposed underground mining scenario, no matter where R_1 is located, the proposed VLC channel model would work in the same way.

The positions of R_1 are graphically described in Figure 2.7. For illustrative purposes in all positions, R_1 is tilted and rotated, and its angles of tilt (β_j) and rotation (α_j) are both 45°. Two walls are considered to represent the side walls of the tunnel, which are non-flat and non-regular. This effect is considered in β_w and α_w, which follow a uniform probability distribution, $\beta_w \sim U[0,180°]$ and $\alpha_w \sim U[0,180°]$. The effect of shadowing is considered with obstructions entering the tunnel and following the Poisson process described in the Section 2.5, whose intensity parameter ϵ is 5 per minute. Furthermore, for simplicity and model illustration, we consider that the joint probability density functions $f_v(x,y)$ and $g_v(w,h)$ follow a uniform distribution, $f_v(x,y) \sim U[0,25]$ and $g_v(w,h) \sim U[0,2]$. The scattering effect is considered by including local scatterers that follow the distribution detailed in Section 2.6. The number of local scatterers (N) is set at 40 [41, 42]. The analysis of this value and its variations is carried out in Section 2.7.1.

2.7.1 Analysis of the Proposed Underground Mining Channel Impulse Response

To evaluate the derived underground mining VLC channel model and confirm the accuracy of our approach, we present the CIRs for the five positions of R_1. These CIRs, each represented by $h_{miner}(t;T_{\mathrm{i}},R_j)$ are defined as the received optical intensity when the transmitted optical intensity is a unit-area Dirac delta function. Therefore $h_{miner}(t;T_{\mathrm{i}},R_j)$ can be obtained from expression (2.31), by adding the delta components $\delta(\cdot)$ that depend on the distance the light beam travels as follows:

$$\begin{aligned} h_{miner}(t;T_{\mathrm{i}},R_j) = {} & h_{LoS_{(sh)}}(t;T_{\mathrm{i}},R_j)\delta\left(t-\frac{\mathrm{d}_{\mathrm{i}j}}{c}\right) \\ & + h^{(1)}_{NLoS_{(sh)}}(t;T_{\mathrm{i}},R_j)\sum_{w=1}^{W}\delta\left(t-\frac{\mathrm{d}_{\mathrm{i}w}+\mathrm{d}_{wj}}{c}\right) \\ & + h_{sca}(t;T_{\mathrm{i}},S_n,R_j)\sum_{n=1}^{N}\delta\left(t-\frac{D_{\mathrm{i}-n-j}}{c}\right). \end{aligned} \tag{2.32}$$

Given a number of rays including LoS, NLoS, and scattering, we compute the detected

Table 2.2: Parameters for the underground mining simulation scenarios.

Parameters	**Features**	
	Reference underground mining scenario	Proposed underground mining scenario
Tunnel:		
Length, X (m)	6	6
Width, Y (m)	3	3
Height, Z (m)	5	5
Wall reflection coefficient, ρ_w	0.6	0.6
Wall rotation angle, α_w (°)	90	U[0,180]
Wall tilt angle, β_w (°)	90	U[0,180]
Scatterer reflection coefficient, ρ_s	0	0.1
Number of scatterers, N	0	40
Transmitter:		
Position, (x,y,z) (m)	(3,0.5,4.5)	(3,0.5,4.5)
Transmitter rotation angle, α_{i} (°)	0	45
Transmitter tilt angle, β_{i} (°)	90	45
Receiver:		
Position 1 (x, y, z) (m)	(3,1,1.8)	(3,1,1.8)
Position 2 (x, y, z) (m)	-	(3,1.5,1.8)
Position 3 (x, y, z) (m)	-	(4,2,1.8)
Position 4 (x, y, z) (m)	-	(2.2,2.5,1.8)
Position 5 (x, y, z) (m)	-	(1,2.5,1.6)
Receiver rotation angle, α_j (°)	0	45
Receiver tilt angle, β_j (°)	90	45
Resolution:		
Time resolution (ns)	0.25	0.25
Area elements in X	18	18
Area elements in Y	18	18
Area elements in Z	15	15
Space resolution in X (m)	0.33	0.33
Space resolution in Y (m)	0.16	0.16
Space resolution in Z (m)	0.33	0.33

Table 2.3: System parameters.

Parameters	**Values**	**References**
Absolute temperature, T_k (K)	295	[12]
Atmospheric parameter, γ	0.017	[89]
Atmospheric parameter, g	0.72	[89]
Atmospheric parameter, f	0.5	[89]
Average transmitted power, P_{i} (W)	10	[12]
Background dark current, I_{bg} (nA)	10	[12]
Band-pass filter of transmission	1	[12]
Boltzmann constant, κ (J/K)	1.38×10^{-23}	[12]
Capacitance, $C_{p\mathrm{d}}$ (F)	112×10^{-8}	[12]
Disc shaped area radius, R_r (m)	1	[41, 42]
Electronic charge, q (C)	1.6×10^{-19}	[12]
FET channel noise factor, Γ	1.5	[12]
FET trans-conductance, g_m (S)	0.03	[12]
Gain of the optical filter, $g(\cdot)$	1	[12]
Half angle FoV, $\Theta/2$ ($^\circ$)	70	[68, 82]
Joint probability density, $g_v(w, h)$	U[0,2]	[82]
Joint probability density, $f_v(x, y)$	U[0,25]	[82]
Lambertian mode number, m	1	[41, 42]
Mie scattering coefficient, k_m	U[0,10]	[39, 40]
Noise bandwidth factor, I_2	0.562	[12]
Noise bandwidth factor, I_3	0.0868	[12]
Open-loop voltage gain, G	10	[12]
Physical active area, A_p (cm^2)	1	[12]
Rayleigh scattering coefficient, k_r	U[0.1,0.01]	[39, 40]
Reflective element area, ΔA_w (cm^2)	1	[12]
Refractive index, η	1.5	[12]
Responsivity, R_{PD} (A/W)	0.53	[12]
Semi-angle at half power, $\Phi_{\mathrm{i}1/2}$ ($^\circ$)	60	[12]

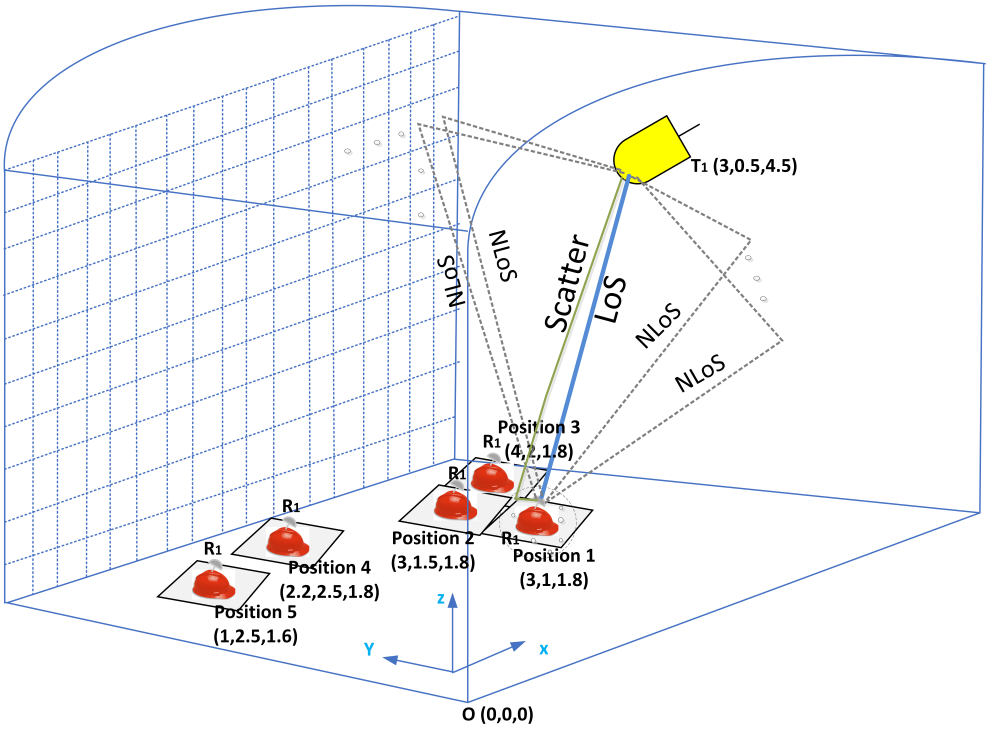

Figure 2.7: Proposed simulation scenario for five different positions of R_1.

power and path lengths from T_1 to R_1 for each ray. Then, these data are processed to produce the CIRs. To compare the results of the CIR, we find it convenient to assume that the transmitted power is 1 W.

Figure 2.8 shows the CIRs for the five positions of R_1 in the proposed underground mining scenario. The number of partitions is set to 18 for X and Y, and 15 for Z. The spacial resolution is set to 0.33 m for X and Z, and 0.16 m for Y. The temporal resolution is set to 0.25 ns (see Table 2.2). The distance represented in the Figure 2.8 is the referential Euclidean distance between T_1 and R_1. We observed in all R_1 positions that the LoS component has a higher contribution in the CIR compared to the NLoS and scattering components. However, the NLoS and scattering components tend to add a significant amount of power to the total CIR. Furthermore, these components arrive later than the LoS component.

If we compare the CIRs in the Figure 2.8, several interesting findings can be distinguished. Firstly, as the distance between T_1 and R_1 increases, the underground mining CIR decreases and its propagation delay increases, as well as the rising edge of the CIR becomes less abrupt. However, we note that although the distance from position 3 of R_1 is less than the distance from positions 4 and 5, the CIR of position 3 is the smallest. This behavior occurs because the effect of shadowing is greater in that scenario due to the position of R_1. In this position, the optical link is more likely to be partially or totally blocked due to the physical characteristics of the obstructions entering the tunnel. Secondly, the results show that the obstructions affect all underground mining scenarios. However, the position least affected by shadowing is the position 1 due to the proximity of R_1 to T_1. It is important to mention that both the LoS component and the NLoS components are affected by shadowing.

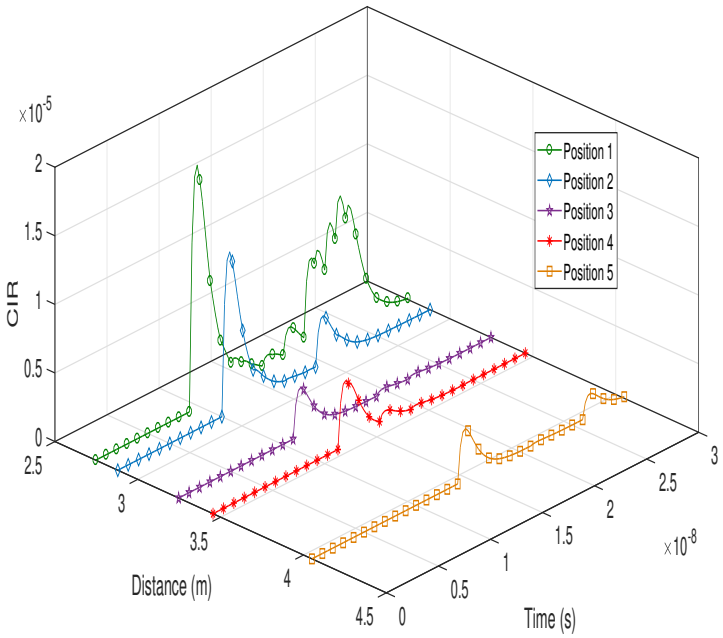

Figure 2.8: CIRs of the five R_1 positions in the evaluated underground mining scenario.

Channel Impulse Response Produced by NLoS Components

To develop an in-depth analysis of each channel component that contributes to the underground mining CIR, Figure 2.9 shows the CIRs of the sum of all the NLoS components of the five positions of R_1. These CIRs in all the scenarios maintain the trend of the total CIRs, that is, the greater the distance between T_1 and R_1, the smaller the magnitude of the CIR and the longer the propagation time. We also note that due to bouncing on the walls, the NLoS component travels a greater distance since leaving T_1 compared to the distance the LoS component travels. Therefore, the NLoS components arrive at R_1 with a longer delay than the LoS component. The effect of non-flat walls by having uniform random α_w and β_w in a specific interval causes NLoS components of various magnitudes without marking an increasing or decreasing trend with respect to time. On the other hand, we note that shadowing directly affects NLoS components depending on the location of R_1. This factor makes the position 1 the least affected and the position 3 the most affect, even though the latter has a shorter distance between T_1 and R_1 compared to positions 4 and 5.

Channel Impulse Response Produced by Scattering Components

To analyze the channel components produced by scattering, Figure 2.10 illustrates the CIRs produced by scattering in the five positions of R_1 for the proposed underground mining scenario. It is possible to notice that although each position increases the distance between T_1 and R_1, the magnitude of the CIR is not drastically decreased among R_1 positions. In fact, it is observed that the maximum magnitudes of the CIRs of position 1 and 2 are approximately equal, as well as the maximum magnitudes of positions 3, 4 and 5, with slight differences. This effect is because each local scatter follows the UDSM distribution. Therefore, since the position of the local scatter with respect to R_1 is random, the distance between the local

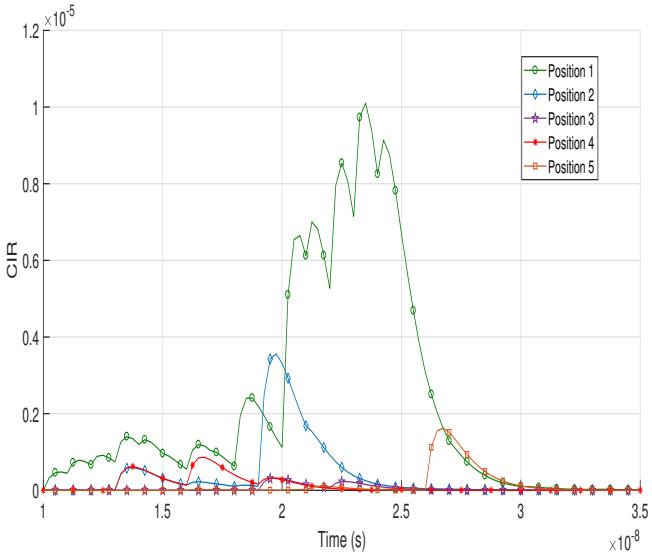

Figure 2.9: CIRs considering the sum of the NLoS components of the five positions of R_1 in the evaluated underground mining scenario.

scatter and T_1 will also be variable, so the CIR will not depend solely on the distance between T_1 and R_1. Furthermore, we consider a gain (G_n) that depends on a general phase function gain that randomly combines Rayleigh and Mie scattering, which directly influences similar magnitudes between scenarios.

On the other hand, we note that when the distance between T_1 and R_1 increases, the scattering components reach R_1 later, maintaining the same trend as the LoS and NLoS components. However, if we compare the arrival times per position of the NLoS CIRs (Figure 2.9) with the arrival times per position of the scattering CIRs (Figure 2.10), we observe that for scattering they are lower. This is due to two factors: 1) We only consider the optical path that starts from T_1, bounces off the local scatterer, and reaches R_1. Therefore, the distance that the optical signal travels is less compared to the distance of the optical path starting from T_1 going to the wall and reaching R_1. 2) Since the local scatters are much closer to R_1 (disk-shaped area), the signal bounce in the local scatter would reach R_1 faster if we compare it with the wall's proximity with R_1. Finally, we can deduce that due to the size of the local scatterers (dust particles) the magnitude of the scatterer CIRs in all the positions is smaller compared to the CIRs NLoS and LoS. However, this magnitude is not negligible and contributes with a factor of the total mining CIR.

For illustrative purposes, and to analyze the effect of the variation and amount of local scatterers, we only choose position 1 of R_1 and vary its values of N as seen in Figure 2.11. We can notice that with values of N=20 and N=40, the maximum magnitude of the CIR remains approximately the same. Furthermore, with these values of N, the CIR reaches the maximum values in comparison with the other values of N. As the value of N decreases, the magnitude of the CIR also decreases. This is because the gain factor (G_n) in the CIR is inversely proportional to N. Although we theoretically assume that $N \to \infty$ (see expression (2.28)) , not all optical signal bounces in local scatterers and reach R_1. This would depend on the optical signal being inside the FoV of R_1. Therefore, with this analysis, we can

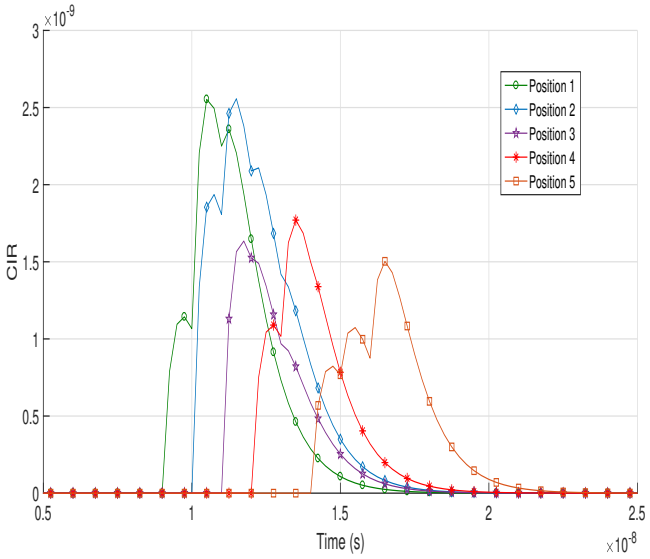

Figure 2.10: CIRs of the scattering components for the five positions of R_1 in the evaluated underground mining scenario.

verify that the value of N (N=40) chosen for all the positions of R_1, allows us to develop a feasible simulation model with reasonable complexity. Furthermore, and not least, it is correct in terms of generating a greater contribution from the CIR of the scatterer, which is superimposed to the total underground mining CIR.

2.7.2 Comparative Analysis between the Reference and Proposed Underground Mining Channel Impulse Responses

To discuss the differences between the proposed underground mining channel model and the reference underground mining channel model, we chose position 1 of R_1 for illustrative purposes. We present their respective CIRs in Figure 2.12. As we described at the beginning of this section, the characteristics of the reference underground mining scenario are deterministic. Furthermore, it is considered neither shadowing nor scattering. As we can notice, because the distance between T_1 and R_1 for both scenarios is the same, both CIRs have the same delay. However, the differences in magnitudes and temporal evolution are notable. In the first instance, we observe that the magnitude of the LoS part that makes up the CIR of the reference underground mining scenario is 3.489×10^{-5} while for the proposed underground mining scenario it is 1.772×10^{-5}. This is a magnitude reduction of 50.78%. This decrease occurs because in the proposed scenario, the obstructions that generate shadowing severely affect the LoS link.

On the other hand, we also observe that the NLoS components of the CIR that belong to the proposed underground mining scenario have a greater contribution compared to the reference underground mining scenario. This effect can be best observed in Figure 2.13. In the reference underground mining scenario the magnitude of the maximum NLoS contribution is 4.002×10^{-6} while for the proposed underground mining scenario it is 2.434×10^{-6}. The effect of shadowing also negatively affects the NLoS components in the proposed underground mining scenario. Compared to the LoS contribution, the magnitude of the maximum

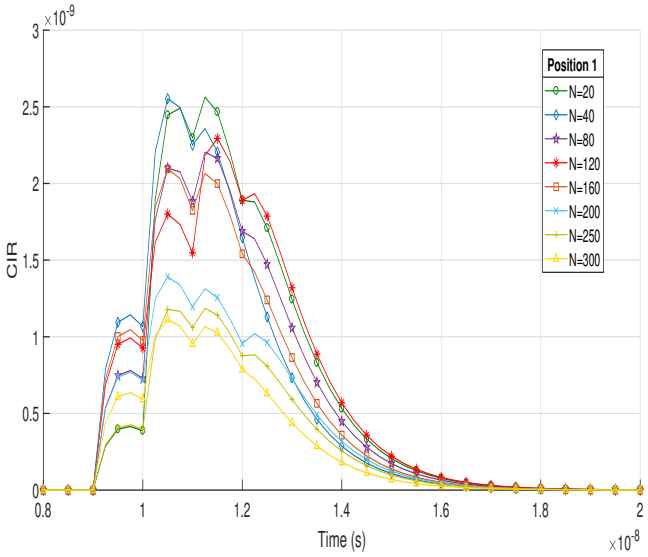

Figure 2.11: CIRs of the scattering component with different values of N for the position 1 of R_1 in the evaluated underground mining scenario.

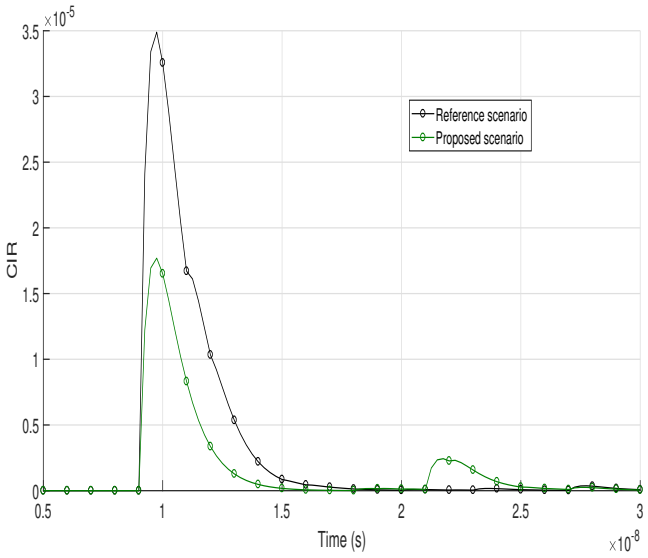

Figure 2.12: Comparison between the total CIR in the reference underground mining scenario and the total CIR in the evaluated underground mining scenario for position 1 of R_1.

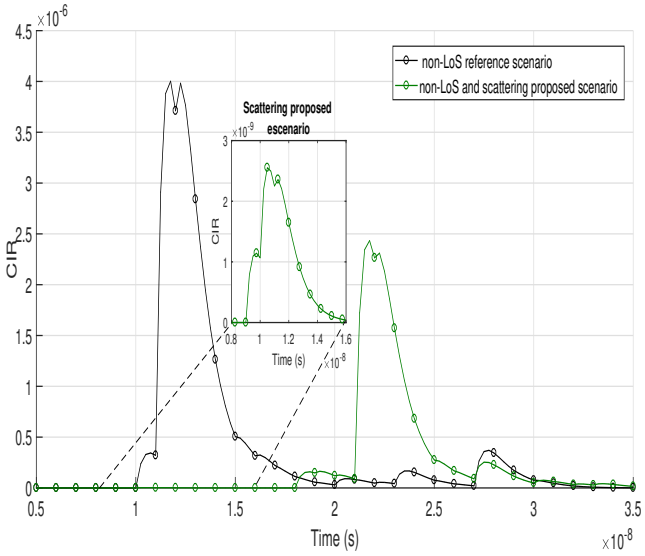

Figure 2.13: Comparison between the CIR of the NLoS component in the reference underground mining scenario and the CIR of the NLoS and scattering components in the evaluated underground mining scenario for position 1 of R_1.

NLoS contribution in the proposed underground mining scenario represents 13.73%. However, for the reference underground mining scenario, the magnitude of the maximum NLoS contribution represents 11.47% with respect to the LoS contribution. The effect of non-flat walls in the proposed underground mining scenario is also highlighted, we can observe greater variability in the magnitudes that make up the CIR.

Finally we see in Figure 2.13 the contribution of scattering in the proposed underground mining scenario and its time delay. Compared to the LoS contribution, the maximum scattering contribution is approximately 0.75%. However, because it is close in time to the LoS pulse and broad in time terms (almost 1 ns), it modifies and affects the falling edge of the LoS pulse of the total underground mining CIR.

2.7.3 Temporal Dispersion Analysis of the Proposed Underground Mining Channel

In wireless communication systems, due to the own nature of the media and multi-path reflections, the channel stretches the signal transmission in time. This phenomenon is well known as temporal dispersion. Therefore, since we are analyzing a VLC channel characterized by reflections and scattering, we find it more practical and effective to adopt a channel estimator. This estimator must be a parameter that directly reports on the temporal dispersion suffered by the CIR $h_{miner}(t, T_{\mathrm{i}}, R_j)$. A detailed observation of this time parameter provides direct information about the channel configuration. Thus, the initial delay until the first pulse appears is proportional to the length of the LoS path. Any delay measured longer than the initial delay is called an excess delay and corresponds to the existence of pulses after the main pulse, which are non-negligible contributions to the total CIR. Following the above reasoning, the parameter that quantifies the temporal dispersion of the CIR is the

RMS delay spread defined as [41, 65]

$$D_{RMS} = \sqrt{\frac{\int_0^\infty (t - \mu_{RMS})^2 \; h^2_{miner}(t, T_\mathrm{i}, R_j)\mathrm{d}t}{\int_0^\infty h^2_{miner}(t, T_\mathrm{i}, R_j)\mathrm{d}t}}, \tag{2.33}$$

where the mean delay spread μ_{RMS} is given by [41, 65]

$$\mu_{RMS} = \frac{\int_0^\infty t \; h^2_{miner}(t, T_\mathrm{i}, R_j)\mathrm{d}t}{\int_0^\infty h^2_{miner}(t, T_\mathrm{i}, R_j)\mathrm{d}t}. \tag{2.34}$$

It should be noted that μ_{RMS} strongly depends on the time that the transmitted pulse takes to propagate from T_1 to R_1 after undergoing a reflection, while the D_{RMS} considers only the stretching of the CIR over time. In practice, we consider $h_{miner}(t, T_\mathrm{i}, R_j)$ as the sum of samples numeric of all the channel components that form it, so the approximate numeric expressions for D_{RMS} and μ_{RMS} are as follows:

$$D_{RMS} = \sqrt{\frac{\sum_{p=0}^{P} (p\Delta t - \mu_{RMS})^2 \; h^2_{miner}(p\Delta t, T_\mathrm{i}, R_j)}{\sum_{p=0}^{P} h^2_{miner}(p\Delta t, T_\mathrm{i}, R_j)}}, \tag{2.35}$$

$$\mu_{RMS} = \frac{\sum_{p=0}^{P} p\Delta t \; h^2_{miner}(p\Delta t, T_\mathrm{i}, R_j)}{\sum_{p=0}^{P} h^2_{miner}(p\Delta t, T_\mathrm{i}, R_j)}, \tag{2.36}$$

where $p\Delta t$ is discretized quantity of t with a maximum number of samples P. We must emphasize that D_{RMS} is critical in high-speed applications, where the maximum bit rate (R_b) is $R_b \leq 1/10 D_{RMS}$ [41, 65].

We have applied the analysis of this subsection and the expressions (2.35) and (2.36) to obtain the characteristic D_{RMS} of $h_{miner}(t, T_\mathrm{i}, R_j)$ over the entire proposed underground mining scenario, as depicted in Figure 2.14. In addition, the main statistical parameters of channel time dispersion are shown in Table 2.4. These parameters are: mean (μ), standard deviation (σ), 90th percentile (90%i*le*), and 100th percentile (100%i*le*).

We consider the entire proposed underground mining scenario according to the dimensions and temporal and spatial resolution of Table 2.2. The maximum and minimum values of the D_{RMS} are 8.28×10^{-9} and 9.01×10^{-12} respectively. Therefore, the maximum R_b that we can reach is 1.20×10^{7} bps. On the other hand, we observe from the Figure 2.14 that the D_{RMS} distribution is totally non-uniform and with high variability compared to ideal indoor scenarios [65, 90] or referential underground mining scenarios [68]. This high variability effect is due to non-flat walls and scattering that we consider in the proposed underground mining environment. As these characteristics are modeled with random parameters, the temporal dispersion of the signals does not have a certain trend.

2.7.4 Analysis of the Received Power in the Evaluated Underground Mining Scenario

An important metric in all communication systems that allows us to verify and analyze the behavior of the channel is the power received at the receiver. For our proposed underground

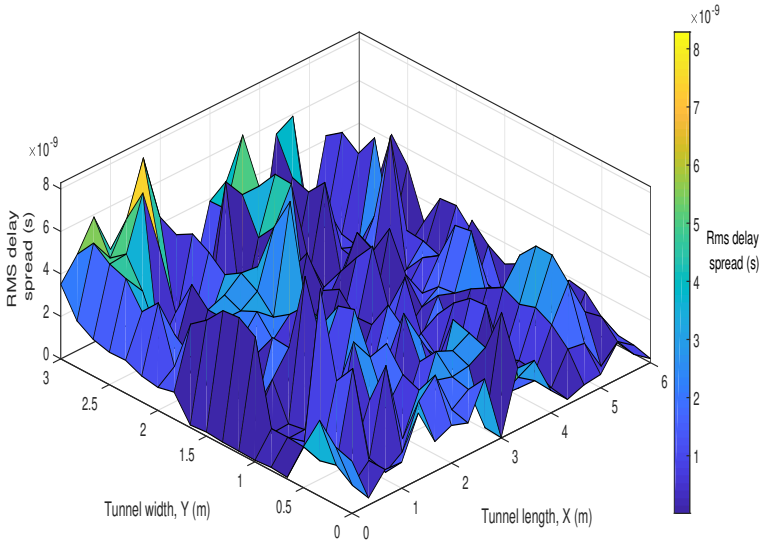

Figure 2.14: RMS delay spread distribution of the proposed underground mining channel model within the evaluated underground mining scenario.

mining scenario, since we consider a single LED along with a single PD, the power received by R_1 due to the light emitted by T_1 is expressed as [65]

$$P_r(R_1) = R_{PD} P_t h_{miner}(0; T_1, R_1) + N_{R1}, \tag{2.37}$$

where $P_r(R_1)$ is the power received of R_1, R_{PD} is the PD responsivity, and P_t is the emitted optical power by T_1. N_{R1} is the additive noise in R_1 that includes two types of noise that particularly affect underground mining environments, shot noise and thermal noise whose variances are denoted as σ^2_{shot} and $\sigma^2_{thermal}$ respectively. These variances are determined by the following expressions [65, 91]:

$$\sigma^2_{shot} = 2qR_{PD}P_rB_n + 2qI_{bg}I_2B_n, \tag{2.38}$$

$$\sigma^2_{thermal} = \frac{8\pi\kappa T_k}{G}\eta A_p I_2 B_n^2 + \frac{16\pi^2\kappa T_k \Gamma}{g_m} C_{\text{pd}}^2 A_p^2 I_3 B_n^3. \tag{2.39}$$

σ^2_{shot} contains two components. The former corresponds to photon fluctuation noise or quantum noise, where q is the electric charge constant, and B_n is the bandwidth of the electrical filter that follows the PD. The latter corresponds to the dark current and excess noise, where I_{bg} is the background current due to the ambient light and the noise bandwidth factor is I_2. In $\sigma^2_{thermal}$, the former and latter components represent the feedback-resistor noise and Field-Effect Transistor (FET) channel noise, respectively. Here, κ is Boltzmann's constant, T_k is absolute temperature, G is the open-loop voltage gain, C_{pd} is the fixed capacitance of PD per unit area, Γ is the FET channel noise factor, g_m is the FET trans-conductance, and I_3 is the noise bandwidth factor [65,91]. The values of these components are defined in Table 2.3.

Figure 2.15 shows the CDF of the power received by R_1 throughout the proposed underground mining scenario. In addition, we insert the graphical distribution of the power

Table 2.4: Statistics of the Temporal Parameters of the Proposed Underground Mining Channel.

	Statistics			
	μ (s)	σ (s)	90%ile (s)	100%ile (s)
D_{RMS}	2.09×10^{-9}	1.77×10^{-9}	4.58×10^{-9}	8.28×10^{-9}
μ_{RMS}	1.74×10^{-8}	4.72×10^{-9}	2.48×10^{-8}	3.59×10^{-8}

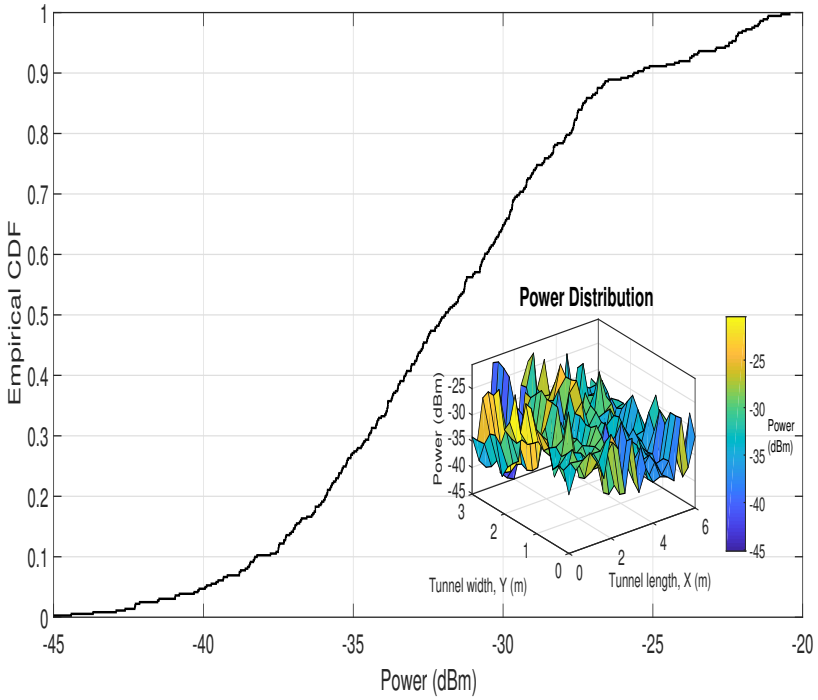

Figure 2.15: Empirical CDF and distribution of the received power in the plane of R_1 for the evaluated underground mining scenario.

received in the evaluated underground mining scenario. We evaluate the power received by maintaining the z-coordinate of R_1 with a value of 1.8 m because it is a typical height value for a miner with a helmet. Furthermore, P_t is fixed at 10 W, to also provide consistent lighting in the tunnel. The maximum and minimum values of the received power are -20.43 dB and -45.10 dB, respectively. From the received power CDF we obtain its μ, σ, and 90%*ile*, whose values are -31.87 dB, 4.91 dB, and -25.58 dB, respectively. If we compare these values with VLC indoors scenarios or referential underground mining scenarios, it can be seen that the received power in the proposed underground mining scenario is the least [65, 68]. Furthermore, the received power distribution in the proposed scenario is not always directly proportional to the distance between T_1 and R_1. Therefore, we note that the effect of the rotation and tilt of T_1 and R_1, non-flat walls, and shadowing are influential on the received optical power levels. In order to mitigate the effects of the proposed channel model, and therefore the received power, it is necessary to apply proper channel estimation and equalization schemes, optical modulation systems, and channel coding techniques.

The proposed underground mining VLC channel model considers the most important

characteristics of an underground mining scenario. Therefore, the proposed model will be a great contribution to the future design of systems or applications based on VLC in these type of harsh environments. However, future work is required to fully validate experimentally the proposed model. Among the future work to be done, we consider the most crucial tasks as follows: (1) Experimental validation of the proposed channel model in a real underground mining scenario. (2) Obtaining experimental statistics of the position, rotation and tilt of the optical receiver and develop empirical models. (3) Obtaining experimental statistics of the rotation and tilt of the non-flat walls of the underground mining tunnel and develop empirical models.

2.8 Conclusion

In this paper, we proposed a novel VLC channel model for underground mines. The derived model is different to the traditional indoor VLC channel model due to the special characteristics found in underground mining environments. In particular, five main factors make the underground mine channel model unique and different. These unique features are the following: randomly rotated and tilted optical transmitters, randomly rotated and tilted optical receivers, non-flat tunnel walls, the presence of obstructions that randomly enter the underground mining scenario that could cause shadowing, and the presence of dust particles that could originate scattering. In order to reasonably present the proposed underground mining VLC channel model, we derived the mathematical analytical expressions of the overall DC channel gain, the underground mining VLC CIR, the RMS delay spread, and the received power in the receiver plane. With these expressions, we verified the validity of the proposed model through numerical experiments within a representative section of a tunnel. Furthermore, we simulated a reference underground mining VLC channel in a referential underground mining scenario, which was compared to the proposed underground mining VLC channel. The simulated data was obtained using a ray tracing methodology. The obtained results demonstrate the notable differences between the proposed underground mining VLC channel model and the reference VLC channel model. In the proposed channel model, the power of the LoS component is reduced by 50.78% compared to the reference channel model. This is mainly due to shadowing, as well as the position and orientation of the transmitter and receiver. Regarding the total magnitude of the proposed underground mining CIR, the NLoS components have a greater contribution compared to the NLoS contributions in the reference CIR. This is due to the effect of the non-flat walls, which generate variability in the magnitudes of the NLoS components. Finally, we have the presence of scattering components that generate temporal dispersion in the proposed total underground mining CIR. The distribution of the RMS delay spread in the entire underground mining environment and its main statistics were found. The impact of non-flat walls and scattering is evidenced by the high variability of the temporal dispersion. Finally, the CDF of the received power and its total distribution in the underground mining scenario were revealed. An in-depth discussion of these parameters demonstrated that the effects of non-flat walls and shadowing are evident in the magnitude of the received power and its variability across the underground mining scenario.

2.9 Acknowledgements

This work was supported in part by the Doctoral Fellowship Grant from ANID PFCHA/Doctorado Nacional/2019-21190489, in part by UDLA Telecommunications Engineering Degree, in part by Project STIC-AMSUD 19-STIC-08, in part by ANID FONDECYT Regular No. 1201893, in part by Vicerrectoría de Investigación y Desarrollo (VID) de la Universidad de Chile Proyecto ENL 01/20, in part by SENESCYT "Convocatoria abierta 2014-primera fase, Acta CIBAE-023-2014", in part by ANID FONDECYT Postdoctorado No. 3190147, and by Grupo de Investigación en Inteligencia Artificial y Tecnologías de la Información (IA&TI).

Chapter 3

Bit Error Probability of VLC Systems in Underground Mining Channels with Imperfect CSI

Analytical expressions of the statistical distribution of the UM-VLC square-channel gain are derived considering scattering, shadowing, and a random position and orientation of the receiver. These expressions are employed to compute the system's BEP considering shot and thermal noises, on-off keying modulation, as well as perfect and imperfect CSI at the receiver side. The results obtained for the BEP are validated by computer simulations for various UM-VLC scenarios. A close agreement is observed between the analytical and simulated curves. Furthermore, the performance of the UM-VLC system improves by increasing the FoV and/or SNR. Indeed, for an FoV value of 45° for both the UM-VLC system with perfect CSI and imperfect CSI, the best performance in terms of BEP is obtained. In terms of the UM-VLC system with imperfect CSI, BEP curves saturate for higher values of SNR due to lower values of FoV, specifically in the case of 45°. Finally, the performance of the UM-VLC system increases significantly for higher values of SNR, specifically in the case of 20 dB.

3.1 Introduction

Compared to traditional indoor environments, the design and implementation of UM-VLC systems are more challenging. This is due to the positioning, tilt, and rotation of the LEDs and PDs that interfere with the LoS link, the irregular walls that affect the optical reflections in the NLoS links, the mobile objects that generate shadowing, and dust particles that produce scattering of the optical signal [33]. Furthermore, shot and thermal noises cause degradation of the received signal [33]. The aforementioned factors generate a high BEP; therefore, an in-depth analysis of the performance of UM-VLC systems is required [31, 92].

The UM-VLC channel gain fluctuates in the time domain due to the physical variables that compose it. To mitigate this impairment, a widely applied strategy is to estimate the CSI at the optical receiver, by considering the random and probabilistic nature of the channel. Several works with these considerations have been reported in the literature. In

[93], the authors propose an interference mitigation scheme by employing a Constrained Field-of-View Angular Diversity Receiver (CFoV-ADR) and channel estimation based on the Least Square (LS) approach. Despite considering an indoor Multiple-Input-Multiple-Output (MIMO) VLC system, the authors assume the VLC channel to be deterministic in nature. Whereas in [22, 23, 94], a performance analysis of indoor VLC systems in terms of error probability and BER, both for Single-Input-Single-Output (SISO) and MIMO systems, is presented. Imperfect CSI is considered by generalizing the error or by utilizing the LS method. In addition, variables such as user mobility and PD orientation are considered in the channel model. However, the channel only considers the LoS component, namely an ideal VLC channel.

In terms of the most relevant and recent works reported in the literature describing UM-VLC channel models, in [16, 34], a path loss model for a VLC channel applied to mines is proposed. In both works, the channel model is based on the well-known Lambertian optical model for indoor environments, where the LoS and NLoS components are considered. Both manuscripts demonstrate that the path loss exhibits a linear behavior in the log-domain. However, their results are based on a channel model that does not include in its analytical expression the main components that affect underground mining tunnels. In [35], the analysis of a VLC system applied to tunnels is characterized. The adopted model is the Lambertian VLC channel model with the LoS and diffuse components. The VLC system performance is evaluated in terms of SER. Despite the fact that its results are obtained by simulating a tunnel scenario, the channel model limits them because it does not consider factors such as shadowing or scattering, and the receiver assumes perfect CSI. In [95], a VLC channel model that considers dust particles is presented. The scenario is analyzed using a Lambertian VLC channel model by considering LoS and NLoS components, and the results are presented in terms of the CIR. However, the limitation of this work is not to include the effect of scattering directly in the theoretical model of the channel.

In [96], the analysis of a VLC system applied to underground mines is presented. The effect of shadowing and scattering are analyzed as channel-independent phenomena. Consequently, the effects of these phenomena are not included in the analytical model of the VLC channel, so this omission would be its main limitation. The channel model is based again on the Lambertian optical scheme with LoS and NLoS components. Therefore, angular variations of transmitter and receiver, and the effect of non-flat walls are considered neither. The channel is evaluated in terms of the path loss and RMS delay spread. Finally, in [36], a neural network-based approach is applied to derive a UM-VLC channel model. The authors assumed a dynamic non-linear behavior of the optical channel. The work is experimentally validated in a dark gallery with a curved roof that emulates a mining tunnel. The main contribution of this article is the estimation of the parameters used for the neural network. However, a disadvantage of this proposal is that the model does not consider the scattering or shadowing phenomena in the estimated coefficients.

Based on previous literary analysis on channel estimation methods and UM-VLC channel models, to the best of our knowledge, the BEP of UM-VLC systems subject to a precise statistical channel model with imperfect CSI has not been analyzed in the literature. Therefore, this paper presents a comprehensive performance analysis of a UM-VLC system corrupted by shot and thermal noises. Based on the IEEE 802.15.7 standard and employing PHY-I

mode, OOK modulation is adopted for the transmission of symbols and the LS estimator is implemented in the receiver side [25].

Our contributions can be summarized as follows: a) The PDF expression of the UM-VLC square-channel gain in terms of LoS, NLoS, and scattering channel components through independent probabilistic factors, that correspond to the random position and orientation of the receiver, and shadowing is obtained. b) An analytical error-rate analysis for the UM-VLC system, simultaneously affected by the aforementioned factors and imperfect CSI, is presented to derive the BEP expressions for OOK modulation based on the IEEE 802.15.7 standard. c) A performance analysis of the UM-VLC system with perfect and imperfect CSI in terms of the FoV is presented.

3.2 System Model

We consider a SISO UM-VLC downlink system, as shown in Figure 3.1. This scenario includes shadowing produced by moving objects, scattering by dust particles, and light reflections from irregular walls. A single LED positioned and oriented between the ceiling and the wall serves a randomly positioned user within the LED coverage area. We assume that the UM-VLC system is affected by the user's random position, the random orientation of a PD-based receiver located in the user's helmet, shadowing effects characterized by a Poisson process, and imperfect CSI. Data transmission is based on the IEEE 802.1.5.7 standard, employing the PHY-I mode and OOK modulation [25], whereas the receiver employs symbol-by-symbol detection. Consequently, the received signal, r, is expressed as [33, 92]

$$r = h_m\, s + n_m, \tag{3.1}$$

where s denotes the transmitted symbol, h_m represents the UM-VLC channel-gain coefficient, and n_m stands for the noise affecting the UM-VLC system. Furthermore, n_m=n_s+n_t, $n_s \sim \mathcal{N}(0,\sigma_s^2)$, and $n_t \sim \mathcal{N}(0,\sigma_t^2)$, being σ_s^2 and σ_t^2 the variances of the shot noise, n_s, and thermal noise, n_t, respectively [33, 43].

3.2.1 Mathematical Model of the UM-VLC Channel Gain

Based on the UM-VLC channel model proposed in [33], the instantaneous UM-VLC channel gain, h_m, can be written as [33]

$$h_m = h_{LoS} + h_{NLoS}^{(1)} + h_{sca}, \tag{3.2}$$

where h_{LoS}, $h_{NLoS}^{(1)}$, and h_{sca} are the channel gains of the LoS link, the NLoS link due to wall reflections, and a NLoS link due to dust scattering, respectively. The channel gains h_{LoS} and $h_{NLoS}^{(1)}$ are subject to shadowing [33]. For simplicity, in expression (3.2) we do not denote time dependency. However, it must be considered that the expression and its variables are time-dependent. After restructuring the channel gain components in terms of the variables of interest (random position and orientation of the receiver, and shadowing) and the geometry

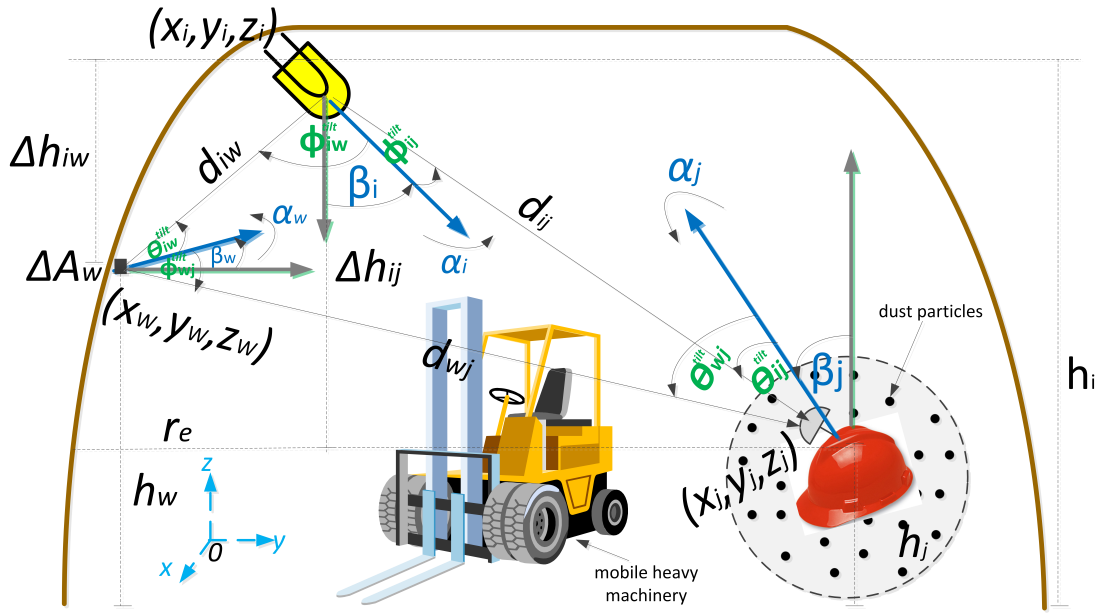

Figure 3.1: Downlink light propagation geometry for the UM-VLC system.

of the UM scenario, the instantaneous channel gain of the LoS link (h_{LoS}) is given by

$$h_{LoS} = \overbrace{\frac{(m+1)A_pG_r}{2\pi}}^{h_{c_1}} \overbrace{\frac{C_2(\frac{C_1}{C_2}+r_m)}{\left(r_m^2+\Delta h_{ij}^2\right)^{m+2/2}}}^{h_{r_{m_1}}} \overbrace{\cos(\theta_{ij}^{tilt})\text{rect}\left(\frac{\theta_{ij}^{tilt}}{\Theta}\right)}^{h_{\theta_{ij}^{tilt}}} \overbrace{P_{ij}}^{h_{p_1}}, \tag{3.3}$$

where A_p is the active area of the PD, θ_{ij}^{tilt} denotes the incidence angle, $G_r = T_s(\theta_{ij}^{tilt})g(\theta_{ij}^{tilt})$ represents the combined gain of the optical filter and optical concentrator, respectively, and r_m is the distance from the center of the optical cell to the receiver. Furthermore, Δh_{ij} is the difference in height between the LED and PD, $m = -1/\log_2\left[\cos(\Phi_{i1/2})\right]$ is the Lambertian mode number of the LED, which is a function of semi-angle at half power ($\Phi_{i1/2}$), P_{ij} is the probability that the LoS optical link is not blocked [33], Θ is the FoV of the PD, and rect $\left(\theta_{ij}^{tilt}/\Theta\right) = 1$ is a decision function, such that $0 \leq \theta_{ij}^{tilt} \leq \Theta$ and 0 otherwise. The respective constants' values are given as $C_1 = \Delta h_{ij}\cos^m(\beta_i) - x_i\sin^m(\beta_i)\cos^m(\alpha_i) - y_i\sin^m(\beta_i)\sin^m(\alpha_i)$ and $C_2 = \cos(\theta_m)\sin(\beta_i)\cos(\alpha_i) + \sin(\theta_m)\sin(\beta_i)\sin(\alpha_i)$, where (x_i, y_i) is the x-y LED location in Cartesian coordinates, β_i is the LED tilt angle with respect to the z-axis, α_i is the LED rotation angle with respect to the x-axis, and θ_m is the user's angular position within the LED coverage area.

The instantaneous gain of the first reflection of the NLoS link $h^{(1)}_{NLoS}$ is given by

$$h^{(1)}_{NLoS} = \overbrace{\frac{(m+1)A_p G_r \Delta A_w \rho_w \cos^m(\phi^{tilt}_{\mathrm{i}w})\cos(\theta^{tilt}_{\mathrm{i}w})}{2\pi(r_{\mathrm{e}}^2+\Delta h^2_{\mathrm{i}w})}}^{h_{c_2}} \underbrace{\frac{C_4(\frac{C_3}{C_4}+r_m)}{\left((r_{\mathrm{e}}+r_m)^2+\Delta h^2_{wj}\right)^{1/2}}}_{h_{r_{m_2}}} \overbrace{P_{wj}}^{h_{p_2}}$$

$$\times \underbrace{\cos(\theta^{tilt}_{wj})\mathrm{rect}\left(\frac{\theta^{tilt}_{wj}}{\Theta}\right)}_{h_{\theta^{tilt}_{wj}}}, \tag{3.4}$$

where ΔA_w denotes the area of the reflective element w, whose reflection coefficient and location are represented by ρ_w and (x_w, y_w), respectively. The incidence angle with respect to w and the irradiance angle of the light component reaching w are symbolized with $\theta^{tilt}_{\mathrm{i}w}$ and $\phi^{tilt}_{\mathrm{i}w}$, respectively. The angles of incidence and irradiance, denoted by θ^{tilt}_{wj} and ϕ^{tilt}_{wj}, respectively, are measured with respect to the light beam reflected by w toward the PD. Δh_{wj} is the difference in height between w and the PD, $\Delta h_{\mathrm{i}w}$ is the difference in height between the LED and w, r_{e} is the maximum coverage radius of the LED, which we assume to coincide with the wall position where w is located. P_{wj} represents the probability that the NLoS optical link is not blocked [33]. The constant's values are $C_3 = -\Delta h_{wj}\cos(\beta_w) - x_w \sin(\beta_w)\cos(\alpha_w) - y_w \sin(\beta_w)\sin(\alpha_w)$ and $C_4 = \cos(\theta_m)\sin(\beta_w)\cos(\alpha_w) + \sin(\theta_m)\sin(\beta_w)\sin(\alpha_w)$, where β_w is the w tilt angle with respect to the z-axis and α_w is the rotation angle with respect to the x-axis.

Finally, the instantaneous channel gain due to dust scattering is given by

$$h_{sca} = \sum_{n=1}^{N} \frac{\overbrace{\frac{C_5 A_p(m+1)}{2\pi}}^{h_{c_3}} \overbrace{\cos(\theta_{S_n-j})\mathrm{rect}\left(\frac{\theta_{S_n-j}}{\Theta}\right)}^{h_{\theta_{S_n-j}}}}{\underbrace{\left[\sqrt{C_r + r_m^2 - C_6\left(r_m^2+\Delta h^2_{\mathrm{i}j}\right)^{1/2}} + r_n\right]^2}_{h_{r_{m_3}}}}. \tag{3.5}$$

We consider that within the disk-shaped area centered on the PD, there are N scatterers (S_n), r_n is the distance from the n^{th} scatterer to the PD, and θ_{S_n-j} represents the angle between the distance vector from the n^{th} scatterer to the PD normal vector [33]. The respective values of the constants are given as $C_r = r_n^2 + \Delta h^2_{\mathrm{i}j}$, $C_5 = G_n \cos^m(\phi_{\mathrm{i}-S_n})$, and $C_6 = 2r_n\cos(\beta_{\mathrm{i}-S_n})$, where G_n is a scatter gain coefficient, $\phi_{\mathrm{i}-S_n}$ is the irradiance angle measured between the LED normal vector and the distance vector from the LED to S_n, and $\beta_{\mathrm{i}-S_n}$ denotes the difference between the angles $\theta_{\mathrm{i}-S_n}$ and $\theta^{tilt}_{\mathrm{i}j}$ [33]. From (3.3), (3.4), and (3.5), it is observed that the channel gains can be expressed as a product of factors corresponding to the random position $h_{r_{m_{(\cdot)}}}$ and orientation $h_{\theta_{(\cdot)}}$ of the receiver, shadowing $h_{p_{(\cdot)}}$, and the constant expressions $h_{c_{(\cdot)}}$.

3.2.2 PDF Derivation of the UM-VLC Square-Channel Gain

In order to obtain the analytical BEP expressions [97], first it is necessary to generate the UM-VLC square channel gain and then obtain its PDF [94, 97]. Therefore, from (3.3), the

channel gain h_{LoS} can be expressed as the product of the deterministic gain h_{c_1}, the user random position $h_{r_{m_1}}$, the random receiver-orientation $h_{\theta_{\mathrm{ij}}^{tilt}}$, and the shadowing h_{p_1}. To obtain the PDF of the LoS square-channel gain, we define $\Delta_{\theta_{ij}^{tilt}}(a,b) = F_{\theta_{ij}^{tilt}}(b) - F_{\theta_{ij}^{tilt}}(a)$ for the $h_{\theta_{\mathrm{ij}}^{tilt}}$ factor, which represents the probability that the random variable $\theta_{\mathrm{ij}}^{tilt}$ is in the interval $(a,b]$, for $a,b \in \mathbb{R}$, $a \leq b$, where $F_{\theta_{ij}^{tilt}}(\cdot)$ is the cumulative distribution function (CDF) of $\theta_{\mathrm{ij}}^{tilt}$ [97]. The CDF of the LoS square-channel gain, $F_{h^2_{\theta_{\mathrm{ij}}^{tilt}}}(x)$, is equal to $F_{h^2_{\theta_{\mathrm{ij}}^{tilt}}}(x) = \Delta_{\theta_{ij}^{tilt}}\left(0.5\cos^{-1}(2x-1), \Theta\right) + T_1(\Theta)\mathrm{rect}\,(x)$, for $0 < x \leq 1$, $F_{h^2_{\theta_{\mathrm{ij}}^{tilt}}}(x) = 0$ for $x < 0$, and $F_{h^2_{\theta_{\mathrm{ij}}^{tilt}}}(x) = 1$ for $x > 1$, whereas $T_1(\Theta) = 1 - F_{\theta_{ij}^{tilt}}(\Theta)$ [97]. The corresponding PDF is given as

$$f_{h^2_{\theta_{\mathrm{ij}}^{tilt}}}(x) = \frac{C_{\theta_{\mathrm{ij}}^{tilt}}}{\sqrt{4x(1-x)}} f_{\theta_{\mathrm{ij}}^{tilt}}\left(\frac{\cos^{-1}(2x-1)}{2}\right) + T_1(\Theta)\delta(x), \tag{3.6}$$

defined for $\cos^2(\Theta) \leq x < 1$ and 0 otherwise. Furthermore, $C_{\theta_{\mathrm{ij}}^{tilt}}$ is a normalization constant and $f_{\theta_{\mathrm{ij}}^{tilt}}$ is the PDF of $\theta_{\mathrm{ij}}^{tilt}$, which is defined in general form to directly incorporate any probability distribution of $\theta_{\mathrm{ij}}^{tilt}$.

For $h_{r_{m_1}}$, we define $\Delta_{r_m}(a,b)$ as the probability that the random variable r_m is in the interval $(a,b]$. Thereby, $F_{h^2_{r_{m_1}}}(y)$ and $f_{h^2_{r_{m_1}}}(y)$ acquire the form of

$$F_{h^2_{r_{m_1}}}(y) = \Delta_{r_m}\left(\frac{y^{1/2}}{C_2} - \frac{C_1}{C_2}, A_1(y)\right), \tag{3.7}$$

$$f_{h^2_{r_{m_1}}}(y) = \frac{C_{r_{m_1}}}{2}\left[\frac{y^M f_{\Delta_{r_m}}\left(A_1(y)\right)}{(m+2)A_1(y)} - \frac{f_{\Delta_{r_m}}\left(A_2(y)\right)}{C_2 y^{1/2}}\right], \tag{3.8}$$

where $F_{h^2_{r_{m_1}}}(y)$ is defined for $C_1^2 \leq y \leq (\Delta h_{ij})^{-2(m+2)}$, equal to 0 for $y < C_1^2$, and 1 for $y > (\Delta h_{ij})^{-2(m+2)}$, whereas $f_{h^2_{r_{m_1}}}(y)$ is defined for $C_1^2 \leq y \leq (\Delta h_{ij})^{-2(m+2)}$ and 0 otherwise. $A_1(y) = \left(y^{\frac{-1}{m+2}} - \Delta h_{ij}^2\right)^{1/2}$, $A_2(y) = \frac{y^{1/2}}{C_2} - \frac{C_1}{C_2}$, $M = \frac{-(m+3)}{m+2}$, and $C_{r_{m_1}}$ is the normalization constant and $f_{\Delta_{rm}}$ is the PDF of r_m, which is defined in general form to directly incorporate any probability distribution of r_m.

For h_{p_1}, we assume that P_{ij} comes from a Poisson process [33], whose CDF and PDF are given as $F_{h^2_{p_1}}(z) = \frac{\Gamma((z+1),\epsilon)}{z!}$ and $f_{h^2_{p_1}}(z) = \exp\left[-\epsilon\mathbb{E}(p_v)z\right]$ for $z \geq 0$. $\Gamma(\cdot,\cdot)$ is the upper incomplete Gamma function, ϵ is the intensity parameter of the Poisson process, p_v is the probability that the LoS is blocked by an obstacle, and $\mathbb{E}(p_v)$ is the expected value of p_v [33].

By exploiting the independence of $h_{r_{m_1}}$, h_{p_1}, and $h_{\theta_{\mathrm{ij}}^{tilt}}$ [9], we find that the PDF of the LoS square-channel gain is given as

$$f_{h^2_{LoS}}(x) = \frac{C_l}{h_{c_1}^2}\int_{\mathcal{R}_y}\int_{\mathcal{R}_z} \frac{\exp\left[-\epsilon\mathbb{E}(p_v)z\right]}{yz}\left[\frac{f_{\Delta_{r_m}}\left(B(y,z)\right)}{(m+2)B(y,z)}(yz)^M - \frac{f_{\Delta_{r_m}}\left(\frac{(yz)^{\frac{1}{2}}-C_1}{C_2}\right)}{C_2(yz)^{\frac{1}{2}}}\right]$$
$$\times\left[f_{\theta_{\mathrm{ij}}^{tilt}}\left(C(x,y,z)\right)\left(\frac{4x}{h_{c_1}^2 yz} - \frac{4x^2}{\left(h_{c_1}^2 yz\right)^2}\right)^{-\frac{1}{2}} + P_1(x,y,z)\right]\mathrm{d}y\,\mathrm{d}z, \tag{3.9}$$

for $0 < x \leq 1$ and $T_1(\Theta)$ for $x = 0$. $C_l = 0.5 C_h C_{r_{m_1}} C_{\theta_{ij}^{tilt}}$ with C_h as the normalization constant, $\mathcal{R}_y$ and $\mathcal{R}_z$ are the set of y and z values for which the function to be integrated takes nonzero value, $B(y,z) = \left((yz)^{\frac{-1}{m+2}} - \Delta h_{ij}^2\right)^{1/2}$, $C(x,y,z) = 0.5\cos^{-1}\left(\frac{2x}{h_{c_1}^2 yz} - 1\right)$, and $P_1(x,y,z) = T_1(\Theta)\delta\left(\frac{x}{h_{c_1}^2 yz}\right)$.

From (3.4), the channel gain $h_{NLoS}^{(1)}$ can be expressed as the product of h_{c_2}, $h_{r_{m_2}}$, h_{p_2}, and $h_{\theta_{wj}^{tilt}}$. Hence, by proceedings as we did to obtain the PDF of $f_{h_{LoS}^2}$, we find that the PDF of the NLoS square-channel gain, $f_{h_{NLoS}^{(1)2}}(x)$, is given as

$$f_{h_{NLoS}^{(1)2}}(x) = \frac{C_n}{h_{c_2}^2}\int_{\mathcal{R}_y}\int_{\mathcal{R}_z} \frac{\exp\left[-\epsilon \mathbb{E}(p_v) z\right]}{yz}\left[D(y,z) f_{\Delta_{rm}}\left(D(y,z) - r_{\mathrm{e}}\right) - \frac{f_{\Delta_{rm}}\left(\frac{E(y,z)-C_3}{C_4}\right)}{C_4 E(y,z)}\right] \times \left[\left(\frac{4x}{h_{c_2}^2 yz} - \frac{4x^2}{\left(h_{c_2}^2 yz\right)^2}\right)^{-\frac{1}{2}} f_{\theta_{wj}^{tilt}}\left(\frac{\cos^{-1}\left(\frac{2x}{h_{c_2}^2 yz} - 1\right)}{2}\right) + P_2(x,y,z)\right] \mathrm{d}y\ \mathrm{d}z, \tag{3.10}$$

for $0 < x \leq 1$ and $T_2(\Theta)$ for $x = 0$, with $T_2(\Theta) = 1 - F_{\theta_{wj}^{tilt}}(\Theta)$. $F_{\theta_{wj}^{tilt}}$ and $f_{\theta_{wj}^{tilt}}$ denote the CDF and PDF of θ_{wj}^{tilt}, respectively, whereas $C_n = 0.5 C_h C_{r_{m_2}} C_{\theta_{wj}^{tilt}}$, $D(y,z) = \left(\frac{y}{h_{c_2}^2 z} - \Delta h_{wj}^2\right)^{-\frac{1}{2}}$, $E(y,z) = \left(\frac{y}{h_{c_2}^2 z}\right)^{\frac{1}{2}}$, and $P_2(x,y,z) = T_2(\Theta)\delta\left(\frac{x}{h_{c_2}^2 yz}\right)$.

From (3.5), the channel gain h_{sca} can be expressed as the sum of the products of h_{c_3}, $h_{r_{m_3}}$, and $h_{\theta_{S_n-j}}$. Since the channel component is the sum of multiple statistically independent dispersion components, it is possible to compute the PDF of the square-channel PDF as $f_{h_{sca}^2}(x) = \sum_{n=1}^{N} P(x_n) f_{h_{sca_n}^2}(x_n)$, where $P(x_n)$ is the probability that the n scatterer interacts with the optical link and reaches the receiver and $f_{h_{sca_n}^2}$ is the individual square-channel PDF for the n scatterer. Therefore, it is possible to define $f_{h_{sca_n}^2}$, and consequently $f_{h_{sca}^2}$ by following the same strategy used to derive $f_{h_{LoS}^2}$ and $f_{h_{NLoS}^{(1)2}}$. Hence, $f_{h_{sca}^2}$ is given as

$$f_{h_{sca}^2}(x) = \frac{C_s}{h_{c_3}^2}\sum_{n=1}^{N} P(x_n)\int_{\mathcal{R}_y}\left[\left(\frac{4x}{h_{c_3}^2 y} - \frac{4x^2}{\left(h_{c_3}^2 y\right)^2}\right)^{-\frac{1}{2}} \times f_{\theta_{S_n-j}}\left(\frac{\cos^{-1}\left(\frac{2x}{h_{c_3}^2 y} - 1\right)}{2}\right) + P_3(x,y,z)\right] \times \left[\frac{F(y) K_1 y^{\frac{5}{2}}\left(\frac{K_4 F(y) + K_5 y + y^{\frac{1}{2}}}{\frac{K_1}{4} y}\right)^{\frac{1}{2}}}{F(y) y + K_6 y^{\frac{5}{2}} + \left(-K_6 y^{\frac{1}{2}} + \frac{K_4}{2}\right) y^2}\right] f_{\Delta_{rm}}(G(y)) \mathrm{d}y\ \mathrm{d}z, \tag{3.11}$$

for $0 < x \leq 1$ and $T_3(\Theta)$ for $x = 0$, with $T_3(\Theta) = 1 - F_{\theta_{S_n-j}}(\Theta)$. $F_{\theta_{S_n-j}}$ and $f_{\theta_{S_n-j}}$ are the CDF and PDF of θ_{S_n-j}, respectively, $C_s = C_h C_{r_{m_3}} C_{\theta_{S_n-j}}$, $P_3(x,y,z) = T_3(\Theta)\delta\left(\frac{x}{h_{c_3}^2 y}\right)$,

$F(y) = \left(-K_2 y^2 + K_3 y^2 + y^{\frac{3}{2}}\right)^{\frac{1}{2}}$, $G(y) = \left(\frac{y^{-\frac{1}{2}} + K_5 y + K_4\left((K_3 - K_2)y^2 + y^{\frac{3}{2}}\right)^{\frac{1}{2}}}{\frac{K_1}{4} y}\right)^{\frac{1}{2}}$, and the respective values of the constants are: $K_1 = 4r_n^4$, $K_2 = r_n^6$, $K_3 = r_n^6 \cos^2(\beta_{\mathrm{i}-S_n})$, $K_4 = 2r_n^3 \cos(\beta_{\mathrm{i}-S_n})$, $K_5 = 2r_n^6 \cos(\beta_{\mathrm{i}-S_n}) - r_n^4 \Delta h_{\mathrm{ij}}^2 - r_n^6$, and $K_6 = 4r_n^9 \cos(\beta_{\mathrm{i}-S_n}) - 4r_n^9 \cos^3(\beta_{\mathrm{i}-S_n})$.

In order to obtain the PDF of the UM-VLC square-channel gain, $f_{h_m^2}$, we must obtain the expression of the square UM-VLC channel gain, h_m^2. Its derivation is obtained by applying basic mathematical operations in the following form:

$$h_m^2 = \left(h_{LoS} + h_{NLoS}^{(1)} + h_{sca}\right)^2, \tag{3.12}$$

$$h_m^2 = 2h_{LoS}h_{NLoS}^{(1)} + 2h_{LoS}h_{sca} + 2h_{NLoS}^{(1)}h_{sca} + h_{LoS}^2 + h_{NLoS}^{2(1)} + h_{sca}^2. \tag{3.13}$$

Due to the characteristic of the optical signal and its propagation behavior in the UM environment [33], we can deduce that for a given instantaneous time, the h_{LoS} component multiplied with each other component in eq. (3.13) will be annulled by their own temporary dispersion. Therefore $2h_{LoS}h_{NLoS}^{(1)} + 2h_{LoS}h_{sca} = 0$. However, the travel time of the $h_{NLoS}^{(1)}$ and h_{sca} components may be the same for some cases, which depend on the receiver position. Hence, this implies that the multiplication performed on the component $2h_{NLoS}^{(1)}h_{sca}$ is close to zero but not zero. In this context, the expression (3.13) can be rewritten as

$$h_m^2 = h_{LoS}^2 + h_{NLoS}^{2(1)} + h_{sca}^2 + 2h_{NLoS}^{(1)}h_{sca}. \tag{3.14}$$

Finally, to obtain $f_{h_m^2}$, we consider the expressions of $f_{h_{LoS}^2}$, $f_{h_{NLoS}^{(1)2}}$, $f_{h_{sca}^2}$, $f_{h_{NLoS}^{(1)}}$, and $f_{h_{sca}}$ by exploiting the independence among them. Hence, the occurrence of one does not affect the probability of occurrence of the other. Therefore, we apply the property of the sum of several probability density functions [6], and the following expression is obtained

$$f_{h_m^2}(x) = 2\left[f_{h_{LoS}^2}(x) \otimes f_{h_{NLoS}^{(1)2}}(x) \otimes f_{h_{sca}^2}(x) \otimes f_{h_{NLoS}^{(1)}}(x) f_{h_{sca}}(x)\right], \tag{3.15}$$

where $\otimes$ is the convolution operator.

3.2.3 Channel Estimation by the Least Squares Method

Imperfect CSI is a problem that occurs in the receiver of any wireless communication system, which is due to a channel estimation error. This is one of the main problems in achieving optimal detection of the received signal. For our study, we consider both perfect and imperfect CSI. In the case of the imperfect CSI, it is necessary to estimate the effect of the UM-VLC channel on the received optical signal since we assume that the optical receiver does not know the channel information. Therefore, we performed the channel estimation using the LS method [94]. This method allows us to obtain the estimated UM-VLC channel coefficients together with their estimation error. The mathematical analysis of the LS method is simple and its implementation complexity is low compared to other channel estimation methods in the literature [94].

We estimate the channel coefficients h_m by transmitting a sequence of independent pilot symbols, T_s, prior to the transmission of the data, according to the IEEE 802.15.7 standard

[25]. Therefore, the received signal vector, $\mathbf{r}_s$, is expressed as $\mathbf{r}_s = h_m\mathbf{s}_s+\mathbf{n}_s$, where $\mathbf{s}_s \in \mathbb{R}^{T_s\times 1}$ is the pilot symbol vector ($\mathbb{R}$ denotes the field of real numbers) and $\mathbf{n}_s = \mathbf{n}_{s(s)}+\mathbf{n}_{t(s)}$, is the additive noise vector, whose components are $\mathbf{n}_{s(s)} \sim \mathcal{N}(\mathbf{0}_{T_s},\sigma_s^2\mathbf{I}_{T_s})$, and $\mathbf{n}_{t(s)} \sim \mathcal{N}(\mathbf{0}_{T_s},\sigma_t^2\mathbf{I}_{T_s})$, being $\mathbf{0}_{T_s} \in \mathbb{R}^{T_s\times 1}$ the vector of zeros and $\mathbf{I}_{T_s} \in \mathbb{R}^{T_s\times T_s}$ the identity matrix.

The channel coefficient estimated by the LS method is obtained as $\hat{h}_{m_{ls}} = h_m + \xi_{ls}$, where $\xi_{ls} = \frac{\mathbf{s}_s^T\mathbf{n}_s}{\|\mathbf{s}_s\|^2}$ is the estimation error, such that $\xi_{ls} \sim \mathcal{N}(0,\Gamma_s)$ with $\Gamma_s = \frac{\|\mathbf{s}_s\|^2}{(\sigma_s^2+\sigma_t^2)}$, and $(\cdot)^T$ is the transpose operator.

To implement a consistent maximum likelihood (ML) rule at the receiver [94], the optimal decision for the UM-VLC system with perfect CSI is given as $\hat{s} = \underset{s}{\text{argmax}}\ (2rh_m - s^2)$. Whereas the decision rule for the system with imperfect CSI is given as $\hat{s} = \underset{s}{\text{argmax}}\ (2r\hat{h}_{m_{ls}} - s^2)$.

3.2.4 BEP Expression for Perfect CSI

The average BEP for the OOK modulation implemented in the UM-VLC system is given as $P_\text{e} = \int_0^\infty Q\left(\sqrt{\frac{\Gamma}{4}\varphi}\right) f_{h_m^2}(\varphi)\text{d}\varphi$ [97], where $\Gamma = \frac{A^2}{(\sigma_s^2+\sigma_t^2)}$, φ is the argument of the PDF. which represents the value h_m^2 takes, and $Q(\cdot)$ is the Q-function, which can be rewritten using the approximation $Q(\nu) \approx \frac{1}{12}\exp\left(\frac{-\nu^2}{2}\right) + \frac{1}{4}\exp\left(\frac{-2\nu^2}{3}\right)$ [24] as $Q\left(\sqrt{\frac{\Gamma}{4}\varphi}\right) = \frac{1}{12}\exp\left(-\frac{\Gamma}{8}\varphi\right) + \frac{1}{4}\exp\left(-\frac{\Gamma}{6}\varphi\right)$. By adopting the previous assumption in P_e, and integrating it in the interval $[h_{m(min)}, h_{m(max)}]$, where $h_{m(min)}$ and $h_{m(max)}$ depend on the ranges of the random variables values in h_m, the closed analytical expression for the BEP is given as

$$P_\text{e} = \left\{ \frac{\sqrt{\pi}}{8}\left[\frac{\text{erf}\left(\sqrt{\alpha_1\varphi}\right)}{3\sqrt{\alpha_1}} + \frac{\text{erf}\left(\sqrt{\alpha_2\varphi}\right)}{\sqrt{\alpha_2}}\right] f_{h_m^2}(\varphi)\right\}\Bigg|_{h_{m(min)}}^{h_{m(max)}}, \tag{3.16}$$

where $\alpha_1 = \Gamma/8$, $\alpha_2 = \Gamma/6$, and $\text{erf}(\cdot)$ is the error function.

3.2.5 BEP Expression for Imperfect CSI

Based on the sub-optimal structure of the VLC system with imperfect CSI, described in Section 3.2.3, the BEP for OOK modulation by using LS is given as

$$P_{\text{e},ls} = Pr\left\{r\hat{h}_{m_{ls}} < 0\right\} \tag{3.17}$$

$$= \int_0^\infty \left[Q\left(\sqrt{\frac{\Gamma}{4}\varphi}\right) + Q\left(\sqrt{\Gamma_s\varphi}\right) - 2Q\left(\sqrt{\frac{\Gamma}{4}\varphi}\right)Q\left(\sqrt{\Gamma_s\varphi}\right)\right] f_{h_m^2}(\varphi)\text{d}\varphi. \tag{3.18}$$

Assuming independence of the noise samples over time, n_m and ξ_{ls} are independent variables. Therefore, using the Q-function approximation [24], we obtain the closed expression of $P_{\text{e},ls}$

as

$$P_{\mathrm{e},ls} = P_{\mathrm{e}} + \left\{ \frac{\sqrt{\pi}}{8} \left[\frac{\mathrm{erf}\left(\sqrt{\alpha_3 \varphi}\right)}{3\sqrt{\alpha_3}} + \frac{\mathrm{erf}\left(\sqrt{\alpha_4 \varphi}\right)}{\sqrt{\alpha_4}} - \frac{\mathrm{erf}\left(\sqrt{\alpha_5 \varphi}\right)}{18\sqrt{\alpha_5}} - \frac{\mathrm{erf}\left(\sqrt{\alpha_6 \varphi}\right)}{6\sqrt{\alpha_6}} - \frac{\mathrm{erf}\left(\sqrt{\alpha_7 \varphi}\right)}{6\sqrt{\alpha_7}} - \frac{\mathrm{erf}\left(\sqrt{\alpha_8 \varphi}\right)}{2\sqrt{\alpha_8}} \right] f_{h_m^2(\varphi)} \right\} \Bigg|_{h_{m(\min)}}^{h_{m(\max)}}, \tag{3.19}$$

which is conditioned by the gain and the statistics of h_m^2, as well as by the statistics of n_m and ξ_{ls}. The respective constants' values are: $\alpha_3 = \Gamma_s/2$, $\alpha_4 = \Gamma_s/3$, $\alpha_5 = \Gamma/8 + \Gamma_s/2$, $\alpha_6 = \Gamma/8 + \Gamma_s/3$, $\alpha_7 = \Gamma/6 + \Gamma_s/2$, and $\alpha_8 = \Gamma/6 + \Gamma_s/3$.

3.3 Numerical Results and Discussion

In this Section, computer simulations are presented to validate the analytical expressions given in (3.16) and (3.19). To evaluate and analyze the effects of the variables that characterize the system, we simulated various UM-VLC scenarios using different random probability distributions; where $\theta_{\mathrm{ij}}^{tilt}$, θ_{wj}^{tilt}, and $\theta_{S_n-j}^{tilt}$ are characterized by $\mathcal{N}(30°,20°)$ or $\mathcal{U}[20°,40°]$, and r_m is given by $\mathcal{R}(2)$ m. or $\mathcal{U}[0,5]$ m., for both perfect and imperfect CSI [97]. The most important parameters used in the simulations and the UM scenario size are summarized in Table 3.1.

Table 3.1: Underground mining VLC scenario features and general simulation parameters.

Parameter	Value
Scenario features	
Scenario size ($w \times l \times h$)	($3 \times 6 \times 5$) m
LED position ($\mathrm{x_i}, y_\mathrm{i}, z_\mathrm{i}$)	(0.5,3,4.5) m
Maximum coverage radius, (r_m)	4 m
VLC transceiver parameters	
Average output optical power	10 W [10, 67]
FoV of the PD	60° [10, 67]
Gain of the optical filter	Unity Gain [10, 67]
Gain of the transmission band-pass filter	Unity Gain [10, 67]
LED and reflective element tilt and rotation angles ($\beta_\mathrm{i}, \alpha_\mathrm{i}, \beta_w, \alpha_w$)	U[90°, 180°] [10, 67]
LED semi-angle, ($\Phi_{\mathrm{i}1/2}$)	60° [10, 67]
Number of PDs	1
Number of scatterers, (N)	40 [10, 67]
Obstacle intensity parameter, (ϵ)	5 per minute [10, 67]
PD height	1.8 m
PD physical active area (A_p)	1 cm^2 [10, 67]
Reflective element area, (ΔA_w)	1 cm^2 [10, 67]
Reflective element position (x_w, y_w, z_w)	(3,3,2.5) m
Responsivity	0.53 A/W [29, 33]
Wall reflection coefficient, (ρ_w)	0.6 [10, 67]
Signal parameters	
Sampling rate	2 samples/bit [98]
Modulation scheme	OOK [98]
Transmission rate	100 kbps [98]
Optical watch	200 kHz [98]
Frame length	24717 bits [98]
Number of frames	122 [98]
Estimation sequence length	24 bits [98]

Figure 3.2 illustrates the BEP versus average SNR per symbol curves for the UM-VLC system with perfect CSI. The analytical BEP was obtained for different FoV values, by varying the probability distributions of r_m, $\theta_{\mathrm{ij}}^{tilt}$, θ_{wj}^{tilt}, and $\theta_{S_n-j}^{tilt}$. The analytical BEP curves obtained using (3.16) agree well with the simulated curves using Monte Carlo simulations. Furthermore, it is observed that the UM-VLC system performance degrades when the FoV decreases for any of the probability distributions of the involved variables.

Figure 3.3 depicts curves of the BEP versus average SNR per symbol for the UM-VLC system with imperfect CSI employing LS estimation and considering $\Gamma_s = 15$ dB [94]. As in Figure 3.2, the BEP increases when the FoV values decrease for all probability distributions analyzed. The analytical BEP curves obtained using (3.19) agree well with the simulated curves using Monte Carlo simulations. In general, the BEP of the UM-VLC system with imperfect CSI are lower compared to the UM-VLC system with perfect CSI. Finally, it is interesting to note that some BEP curves saturate for higher values of Γ due to lower values of Θ, specifically in the case of $\Theta = 45°$.

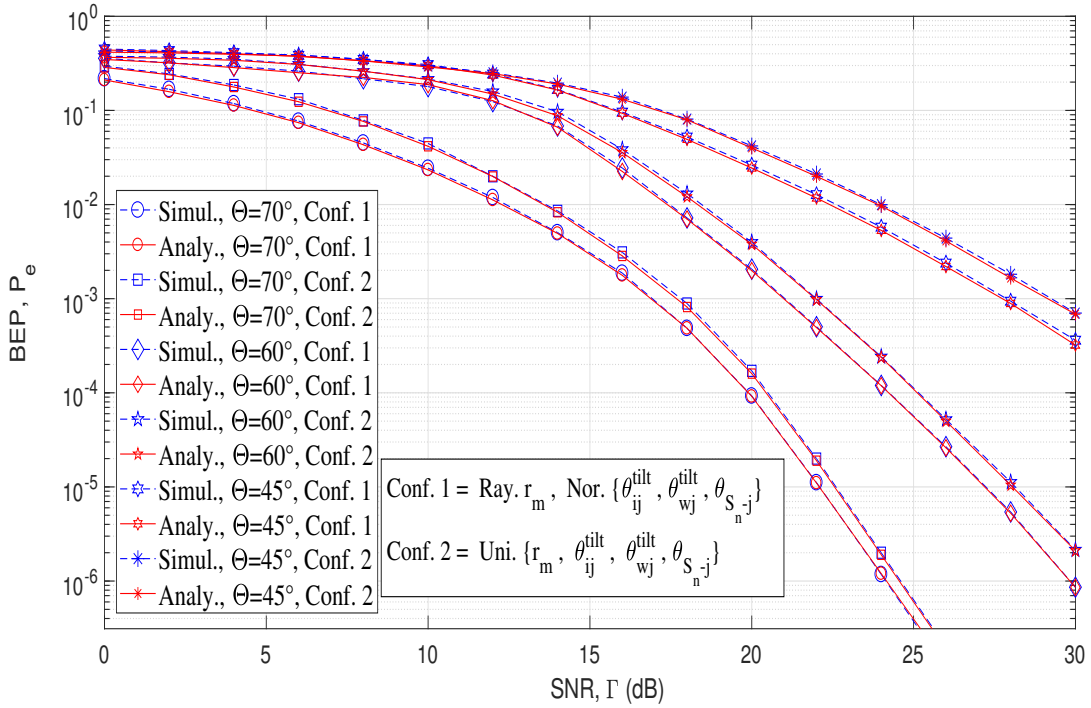

Figure 3.2: BEP versus the average SNR per symbol with perfect CSI.

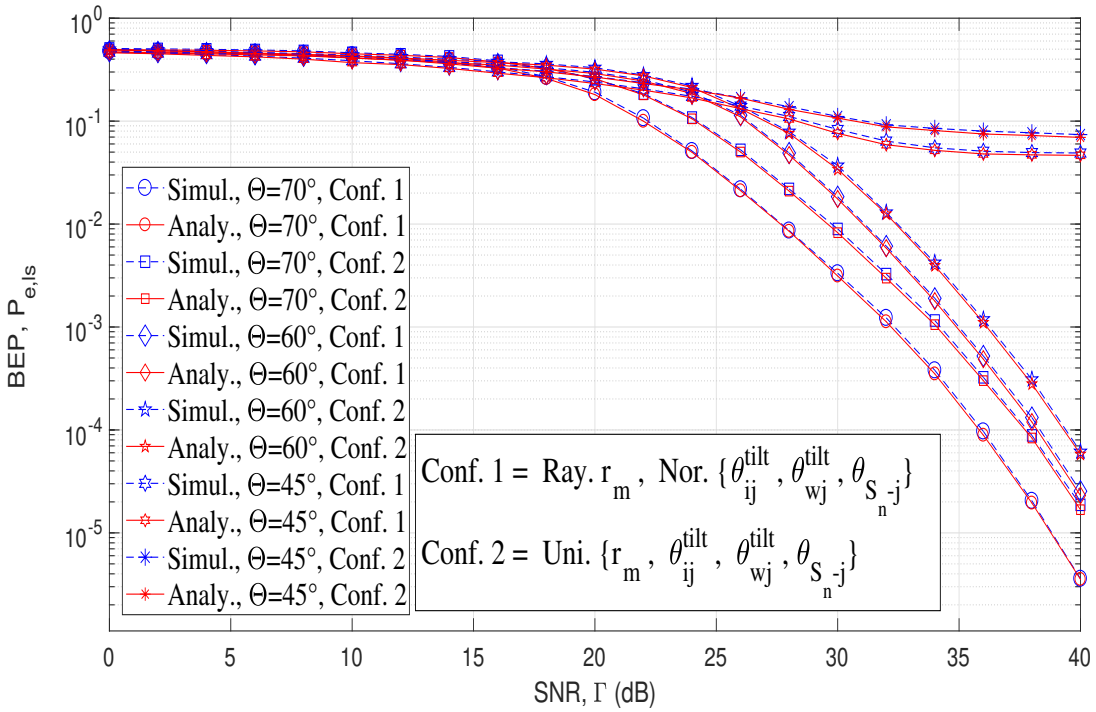

Figure 3.3: BEP versus the average SNR per symbol with imperfect CSI and $\Gamma_s = 15$ dB.

Finally, Figure 3.4 depicts the analytical curves of BEP versus Θ considering perfect and imperfect CSI employing LS estimation and several values of Γ and Γ_s. In general, it is

noted that with higher Θ values, the system performs better. Furthermore, the performance increases significantly for higher values of Γ and Γ_s, whereas for lower Θ, Γ, and Γ_s values, the performance of the system is almost identical. We can also observe that the saturation of some BEP curves tends to be prominent due to higher values of Γ_s.

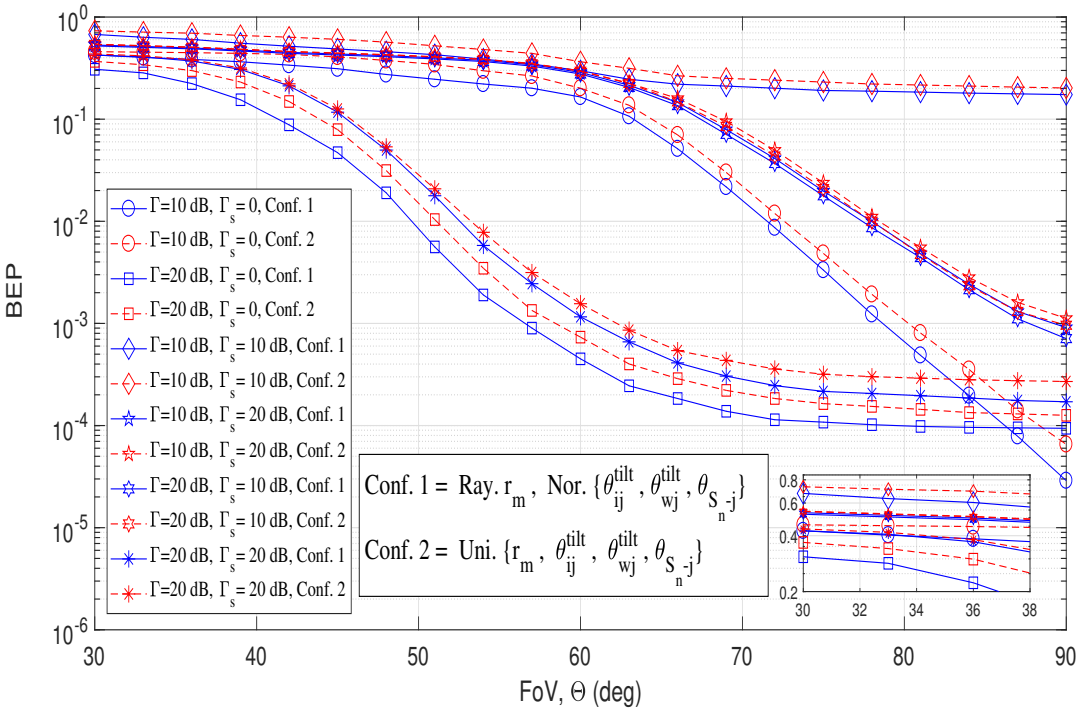

Figure 3.4: BEP versus FoV of the LED with perfect and imperfect CSI.

3.4 Conclusion

In this manuscript, statistical expressions for the UM-VLC square-channel gain components, as well as the analytical expressions for the BEP are obtained. A close agreement is observed between the analytical and simulated curves, which verifies the effectiveness of the analysis presented. The performance of the system mainly depends on the position and orientation of the receiver, as well as shadowing, which are analyzed using various PDF expressions. In general, the system performs better for higher values of FoV. We also note a slight dependence of the system considering perfect CSI and LS estimation for lower FoV values. Whereas for higher FoV values, the performance of the system depends on the precision of the channel estimation technique. In the case of the UM-VLC system with perfect CSI, a value of $\Theta = 70°$ generates the best performance in terms of BER for both random distributions of the variables of interest (Normal and Rayleigh). This effect is due to the direct dependence of the channel components with Θ. On the other hand, in the case of the UM-VLC system with imperfect CSI, the values of $\Theta = 70°$ and $\Theta = 45°$ generate the best and worst performance of the UM-VLC system, respectively. In this case, there is also a direct dependence in terms of the values of Γ and Γ_s used. The saturation of various BER curves is more prominent for a value of $\Gamma_s = 20$ dB, due to its limiting effect on the performance of the UM-VLC system.

As future work, the analysis of the UM-VLC MIMO system and the experimental validation of the theoretical expressions and analytical results found in this article are considered. This validation will be developed after implementing an experimental UM-VLC test-bed that emulates the physical characteristics of underground mines. In this sense, the experimental UM-VLC test-bed will be implemented using VLC transceivers, electro-optical components, and a prototype to emulate real conditions within UM tunnels.

3.5 Acknowledgements

This work was supported by ANID FONDECYT Regular No. 1211132, Doctoral Fellowship Grant from ANID PFCHA/Doctorado Nacional/2019-21190489, CODELCO: Concurso Piensa Minería 2021, UDLA Telecommunications Engineering Degree, SENESCYT "Convocatoria abierta 2014-primera fase, Acta CIBAE-023-2014", and Grupo de Investigación en Inteligencia Artificial y Tecnologías de la Información (IA&TI).

Chapter 4

An Enhanced VLC Channel Model for Underground Mining Environments Considering a 3D Dust Particle Distribution Model

Underground Mining is a hostile industry that generally requires a wireless communication system as a cross-cutting axis for its optimal operation. Therefore, in the last five years, it has been shown that, in addition to radio-frequency-based communication links, wireless optical communications, such as VLC, can be applied to UM environments. The application of VLC systems in underground mines, known as UM-VLC, must take into account the unique physical features of underground mines. Among the physical phenomena found in underground mines, the most important ones are the positioning of optical transmitters and receivers, irregular walls, shadowing, and a typical phenomenon found in tunnels known as scattering, which is caused by the atmosphere and dust particles. Consequently, it is necessary to use proper dust particle distribution models consistent with these scenarios to describe the scattering phenomenon in a coherent way in order to design realistic UM-VLC systems with better performance. Therefore, in this article, we present an in-depth study of the interaction of optical links with dust particles suspended in the UM environment and the atmosphere. In addition, we analytically derived a hemispherical 3D dust particle distribution model, along with its main statistical parameters. This analysis allows to develop a more realistic scattering channel component and presents an enhanced UM-VLC channel model. The performance of the proposed UM-VLC system is evaluated using computational numerical simulations following the IEEE 802.1.5.7 standard in terms of CIR, received power, SNR, RMS delay spread, and BER. The results demonstrate that the hemispherical dust particle distribution model is more accurate and realistic in terms of the metrics evaluated compared to other models found in the literature. Furthermore, the performance of the UM-VLC system is negatively affected when the number of dust particles suspended in the environment increases.

4.1 Introduction

Despite being an industry that generates a large part of Gross Domestic Product (GDP) for many countries worldwide, the UM work environment and its physical characteristics are considered dangerous and unsafe [1, 3]. External factors generated by the regular operation of the mine, such as toxic components, heavy metals, and dust particles make work in UM tunnels hostile. Therefore, to generate greater control of mining activity, it is necessary to establish reliable and stable communication systems in order to manage day-to-day communication, along with emergencies that may occur in this environment. However, the physical structure of UM tunnels is a challenge for the design and implementation of systems that allow stable and effective communication. [61].

Among the current communication systems applied to UM, wired communication systems (copper, coaxial, or fiber) are susceptible to damage by the working environment and are not reliable in UM tunnels. In terms of wireless communication systems, radio communication systems exhibit high signal attenuation due to electromagnetic interference in mining tunnels [60]. It is also important to mention that these environments need good lighting that meets international standards for safe work [59]. These challenges and disadvantages of the current technologies implemented in UM are presented as opportunities to research and develop complementary communication systems that guarantee efficient communication and optimize the lighting in UM environments simultaneously. Therefore, to address these communication and lighting problems in a single system, the concept of VLC has been introduced for UM communication [12, 63].

There are several benefits of applying VLC-based technologies in UM, such as unlicensed spectrum usage capacity ranging from 400 THz to 800 THz, cost versatility for VLC system components, environmental friendliness, and immunity to electromagnetic interference [64]. In terms of the VLC system and its elements, the basic components of a VLC system for any type of environment are a) LEDs, which are made up of cold light, and form lamps with a long useful life. The LED lamps can be located on the ceiling or walls of the UM tunnels. b) PDs that could be installed in machinery, devices that need to be controlled, or the helmet of the mining worker. This scenario creates a VLC link between devices or workers and the mining infrastructure, or also between devices, which favors the design of multiple applications. [67]. c) The channel model, which is an important step for an efficient, reliable, and robust VLC system design [8].

According to the specialized literature, with the process of modeling the communication channel realistically and efficiently, the overall performance of the communication system can be improved [62]. Furthermore, adequate modeling ensures a correct approach and contextualization of the problems that may arise in communication systems [63]. Specifically for VLC systems applied to underground mines, a VLC channel model that considers the physical characteristics that affect UM tunnels was proposed [10]. Here, the random orientation of optical transmitters and receivers, which impact directly the LoS and NLoS components, were considered in the mathematical model. In addition, the characterization of non-flat walls in tunnels and their reflection effects on the optical signal were considered. Finally, a shadowing pattern that considers the entry of objects into the UM tunnel and a scattering model based on a random distribution of dust particles around the PD on a 2D disk was

considered.

In indoor environments such as offices, homes, or hospitals, the effect that suspended dust particles can generate on the optical links is neglected. Consequently, VLC systems applied to these scenarios do not compromise their performance due to the scattering phenomenon. In contrast, in UM environments, drilling and rock excavation work produce a large amount of suspended dust. Therefore, it is a major challenge to efficiently model the scattering effect and include it in the overall UM-VLC channel model. It should be noted that the scatterer distribution model used in [10] is easy to develop and implement. However, it was presented as an initial basic model that must be improved to make it more realistic. Since scatterers are considered multi-path components in the UM-VLC channel model, the received multi-path signal plays an important role in VLC system performance analysis. Therefore, the development of more realistic scatterer distribution models around the behavior of the dust particles in the tunnel must be analyzed and studied. This will allow us to make the channel model presented in [10] more accurate and realistic in its representation of the UM tunnel.

In the following subsections, we first discuss various models of general scatterer distributions based on stochastic geometry proposed in the state of the art. Then, studies of the effects and influence of dust particles on the optical signal applied to several VLC systems are presented.

4.1.1 Works Related to General Scatterer Distribution Models

Several works related to scattering distribution models applied to general communication schemes are presented in [37]-[41]. In [37] and [38], a uniform distribution model that locates the scatterers in a 2D disk region centered on the optical receiver is presented. For the system modeling, the authors consider a mobile station as a receiver. Although the focus of the model presented is not VLC systems, this proposal could be applied to any type of technology based on wireless communication, which includes dust particles that generate scattering. In [40], the authors present a statistical analysis in terms of arrival time and arrival direction of a geometric channel model that considers a mobile transmitting station and scatterers distributed in a hemispheric area around a receiving base station. The results show that this scatterer distribution can be implemented in any multi-path wireless communication system. The manuscript presented in [41] introduces to the state of the art a Gaussian model of scatterer distribution. The authors mention that this model is applicable to multi-path wireless communication systems due to its spatial and temporal properties. The demonstrated statistical results are presented in terms of arrival angle and arrival time. Finally, the work in [39] proposes a general channel model for any communication system that includes scattering particles. This three-dimensional model is based on stochastic geometry, where a Gaussian distribution of scatterers located around an arbitrary point within a spheroid is assumed. Furthermore, the transmitter and receiver are considered to be located at the focal points of this spheroid. Statistics in terms of the arrival angle and the arrival time of the model are obtained. Being a generalized channel model, this proposal could be extrapolated to wireless communication systems in indoor environments, in order to evaluate their performance.

As we can see in the analyzed literature, a large part of the proposed scatterer distribution models can be implemented in any type of multi-path wireless communication system, both

indoors and outdoors. This advantage implies that they can also be extrapolated to VLC systems applied to underground mines.

4.1.2 Scatterer Distribution Models Applied to Optical Communication Systems

After an in-depth literature review, it can be seen that there are some works that present scatterer distribution models applied to optical communication systems [10, 42, 99]-[103]. In [99] and [100], a spread spectrum wireless dispersion model based on an NLoS optical component is presented. The paradigm of these works is based on the fact that air molecules and suspended aerosols build NLoS optical communication links caused by scattering when using carriers in the infrared light band. References [42] and [101] are the pioneering research by including and modeling the effect of scattering in indoor VLC environments. To model scattering, several particles are randomly placed in a 2D ellipse or ring shape. Finally, the complete VLC channel model is derived by the arithmetic add of the LoS channel component and the channel components produced by scattering. In [102], the authors propose a 3D Regular-Shaped Geometry-Based Stochastic Model (RS-GBSM) for vehicular VLC Multiple-Input Single-Output (MISO) channels. The distribution proposed combines a two-sphere model and an elliptic-cylinder model. The results of this work demonstrate the relationship between the communication range and the elevation angle in the proposed model on the received optical power. The authors in [10] present a novel channel model that includes in its analysis influential factors in the UM-VLC system. Among the characteristics considered are the random orientation of the LED and PD, irregular walls that produce reflections with random directions, shadowing caused by machinery and scattering caused by suspended dust particles. Although the VLC channel model presented considers important components of the UM environment, the scatterer distribution model implemented is simplistic. This model is based on the assumption that the dust particles are distributed within a two-dimensional disk-shaped area. Therefore, this scheme should be improved to have a more accurate and realistic UM-VLC channel model. Finally, the most recent work on the study of dust particles and their influence on VLC systems applied to underground coal mines is presented in [92]. The focus of this manuscript is based on the influence of coal dust particles and the scattering model. Furthermore, the impact of coal dust particles on visibility and attenuation is analyzed for visible light transmission. Although the work analyzes the effect of scatterers (dust particles) on the performance of the VLC system, the article does not present a specific mathematical and analytical model of scatterer distribution for the tunnel environment. A VLC channel component produced by the interaction of light with scatterers is also not specified.

As observed in the state of the art analysis of scatterer models applied to optical communications systems, the consideration and implementation of dust particles distributions that closely emulate their behavior in UM environments and their effect on VLC systems. Neither an exhaustive analysis on the interaction of light bonds with the atmosphere and dust particles in UM tunnels has been made. Based on these premises and opportunities to improve the existing state-of-the-art UM-VLC channel models, the main contributions of this work are presented below:

1. An in-depth analysis of the absorption and scattering parameters in the UM environ-

ment and the interaction of the incident light in the VLC system with the dust particles and the atmosphere of the UM environment was performed.

2. A novel 3D dust particle distribution model based on a hemispherical region, along with its mathematical parameters and its statistics based on the joint distribution of the arrival time and the arrival angle of the scattering down-link were developed and analytically proposed.
3. A more accurate and realistic UM-VLC channel component produced by dust particles (scattering), which enhances the general UM-VLC channel model, was derived and presented.
4. The performance of the proposed enhanced UM-VLC channel model was examined, evaluated, and compared with a state-of-the-art UM-VLC channel model in terms of CIR, received power, SNR, RMS delay spread, and BER.

4.2 Underground Mining VLC System Model

In this article, we consider a SISO UM-VLC down-link system, as shown in Figure 4.1. This scenario includes the following characteristics, which are common in UM environments: a) a randomly positioned and oriented LED between the ceiling and wall of the mining tunnel, which serves as an optical transmitter, b) a PD located and randomly oriented at a height determined by the common position of devices on the tunnel, which serves as an optical receiver. c) Irregular walls, which generate random reflections of the optical signal that directly affect the non-LoS component of the UM-VLC channel d) Random shadowing produced by heavy machinery, which can partially or totally block the LoS or non-LoS channel components, e) scattering produced by dust particles, which are generated by the work environment of a mining tunnel [10]. Under this context, this article focuses its study on the interaction of dust particles and the atmosphere with the light beam in the UM-VLC system, its basic absorption and scattering parameters, and the analysis of the dust particles distribution that best adapts to the UM environment, in order to obtain a better UM-VLC channel model component produced by dust particles (scattering) in the scenario.

In this work, the LED transmission is based on the PHY-I mode together with the OOK modulation, which is described in the IEEE 802.1.5.7 standard. On the other hand, the PD reception employs asynchronous symbol-by-symbol detection. [104, 105]. Under this context, the received signal, r, is expressed as [104, 105]

$$r = h_m \otimes s + n_m, \tag{4.1}$$

where s denotes the transmitted symbol, h_m represents the instantaneous UM-VLC channel-gain coefficient, n_m stands for the noise affecting the UM-VLC system, and $\otimes$ is the convolution operator. Where n_m=n_s+n_t, $n_s \sim \mathcal{N}(0,\sigma_s^2)$, and $n_t \sim \mathcal{N}(0,\sigma_t^2)$, being σ_s^2 and σ_t^2 the variances of the shot noise, n_s, and thermal noise, n_t, respectively [104].

Based on the phenomena and features previously mentioned, the characterization of h_m can be written as [10]

$$h_m = h_{LoS} + h_{NLoS}^{(1)} + h_{sca}, \tag{4.2}$$

where h_{LoS}, $h_{NLoS}^{(1)}$, and h_{sca} represent the channel gains of the LoS link, the NLoS link, which represents the light reflections on the tunnel walls, and a component produced by

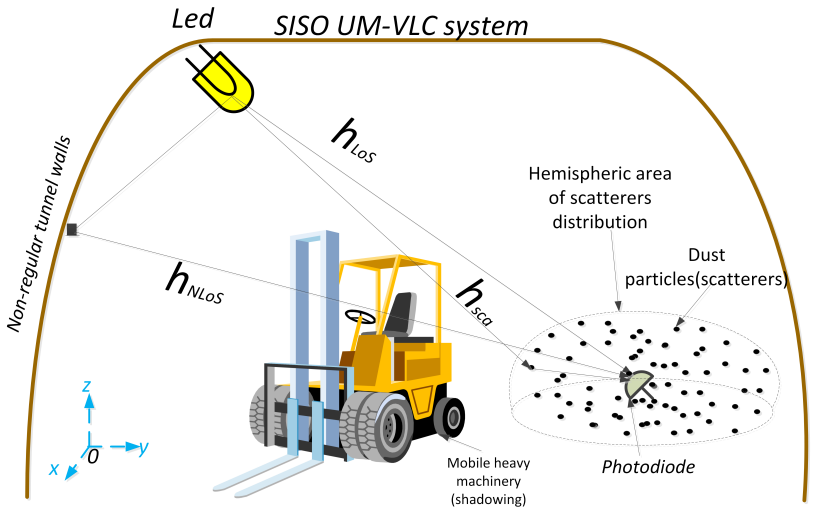

Figure 4.1: Geometry of the channel components that make up the SISO UM-VLC system.

the scattering, respectively. We must consider that the shadowing phenomenon harmfully affects the h_{LoS} and $h^{(1)}_{NLoS}$ components, which is included in them as a coefficient that takes values between 0 and 1 to indicate a partial or total blocking of the link. The analytical and mathematical derivation together with the justification of the variables included in the components of the UM-VLC channel model are presented in detail for in-depth verification in [10].

In the next section we will analyze in depth the scattering phenomenon that occurs in the UM scenario and we will present the proposed 3D dust particle distribution model, which is based on a hemispheric area around the user's helmet.

4.3 Analysis of the Scattering Phenomenon in Underground Mines and Distribution of Dust Particles

In UM environments, the work of people and machinery to drill, crush and fly rock generates large amounts of suspended dust particles. Therefore, it is necessary to first analyze the interaction of the light beam with the dust particles, then generate a dust particle distribution model to finally model the scattering effect and introduce it as a component in the complete UM-VLC channel model.

4.3.1 Atmospheric and Dust Particles Scattering and Absorption Parameters in UM

The distribution and concentration of dust particles suspended in mining tunnels have a strong impact on the propagation of the optical signal and, consequently, on the performance of the VLC system. In general, dust particles can generate two phenomena: a) absorption of light when dust particles combine with water vapors and the light beam hits them, b) scattering of light when dust particles consist only of coal or other organic matter and the light beam hits them. Both events can generate severe attenuation of the optical link. Therefore,

the relationship between the intensity of the incident light and the intensity of the transmitted light, which can be considered as the intensity attenuation, can be expressed as follows

$$I_R = I_T(\alpha_T, \beta_T) \exp\left(-\frac{1.5CLK_{\mathrm{e}}}{\mathrm{d}}\right), \tag{4.3}$$

where C is the number of suspended particles in the unit volume, also called dust particle concentration, α_T and β_T represent the rotation and tilt angles of the LED respectively, L is the light path, d denotes the Euclidean distance between the LED and PD, and K_{e} is the light attenuation coefficient, which is represented with the expression $K_{\mathrm{e}} = k_{sca} + k_{abs}$, being k_{sca} the scattering coefficient and k_{abs} the absorption coefficient. Furthermore, C is a dynamic parameter that can be modeled as an exponential function in terms of the visibility of the UM environment (V) under the expression $C = 4050V^{-1.016}$.

If we consider the basic theory of light atmospheric transmission, k_{sca} and k_{abs} allow us to determine the average distance that a photon travels before being scattered or absorbed, respectively. This consideration can be applied to mining tunnels since dust particles can be assumed as aerosols of various sizes. Under this context, the effect of scattering and absorption produced by the interaction of light with dust particles can be modeled under the paradigms of the Rayleigh and Mie theory, respectively [99, 100]. Therefore, k_{sca} and k_{abs} are the sum of molecule and aerosol scattering and absorption coefficients, represented as

$$k_{sca} = k_{sca}^{Ray} + k_{sca}^{M\mathrm{ie}}, \tag{4.4}$$

$$k_{abs} = k_{abs}^{Ray} + k_{abs}^{M\mathrm{ie}}, \tag{4.5}$$

where k_{sca}^{Ray} and $k_{sca}^{M\mathrm{ie}}$ represent the Rayleigh and Mie scattering coefficients respectively, and k_{abs}^{Ray} and $k_{abs}^{M\mathrm{ie}}$ are the Rayleigh and Mie absorption coefficients respectively. Since the composition of air molecules and dust particles is relatively constant in low-altitude UM areas, k_{sca}^{Ray} is given by

$$k_{sca}^{Ray} = \frac{(m_s^2 - 1)^2(6 + 3\delta)24\pi^3}{(m_s^2 + 2)^2(6 - 7\delta)\lambda^4 N_s}, \tag{4.6}$$

where N_s is the molecular number density for air in UM, λ is the wavelength of the transmitted light beam, δ is the depolarization factor, and m_s is the refractive index, which at the level of the mining tunnels is expressed as

$$(m_s^2 - 1) \times 10^8 = 8060.51 + \frac{2480990}{132.274 - \lambda^{-2}} + \frac{17455.7}{39.32957 - \lambda^{-2}}. \tag{4.7}$$

On the other hand, k_{abs}^{Ray} is a combination of different types of light absorption produced by gases such as O_2, O_3, CO_2, among others, which are typical in UM environments. The absorption of light produced by these gases at different wavelengths can be represented through the Atmospheric Radiation Transport Model (MODTRAN), as shown in [106].

In terms of $k_{sca}^{M\mathrm{ie}}$ and $k_{abs}^{M\mathrm{ie}}$, these coefficients can be modeled based on the Mie theory through a dust particle size distribution with arbitrary form $n(r_{\mathrm{d}})$, which is expressed as

$$k_{sca}^{M\mathrm{ie}} = \int_0^\infty \pi r_{\mathrm{d}}^2 Q_{sca}(r_{\mathrm{d}}, \lambda, m) n(r_{\mathrm{d}}) \mathrm{d}r_{\mathrm{d}}, \tag{4.8}$$

$$k_{abs}^{Mie} = \int_0^\infty \pi r_{\mathrm{d}}^2 Q_{abs}(r_{\mathrm{d}}, \lambda, m) n(r_{\mathrm{d}}) \mathrm{d}r_{\mathrm{d}}, \tag{4.9}$$

where r_{d} is the dust particle radius, m is the complex refractive index of dust particles, and Q_{sca} and Q_{abs} are the scattering and absorption coefficients respectively, which can be obtained as follows

$$Q_{sca}(r_{\mathrm{d}}, \lambda, m) = \frac{2}{\mathrm{d}_s^2} \sum_{n=1}^{\infty} (2n+1) \left(|a_n|^2 + |b_n|^2 \right), \tag{4.10}$$

$$Q_{abs}(r_{\mathrm{d}}, \lambda, m) = \frac{2}{\mathrm{d}_s^2} \left[\sum_{n=1}^{\infty} (2n+1) \left(a_n + b_n \right) - \sum_{n=1}^{\infty} (2n+1) \left(|a_n|^2 + |b_n|^2 \right) \right], \tag{4.11}$$

where $\mathrm{d}_s = 2\pi r_{\mathrm{d}}/\lambda$. Furthermore, a_n and b_n can be expressed as

$$a_n = \frac{\left[\psi_n(m\mathrm{d}_s) \psi_n(\mathrm{d}_s) \right] (m-1)}{\left[\psi_n(m\mathrm{d}_s) \xi_n(\mathrm{d}_s) \right] (m-1)}, \tag{4.12}$$

$$b_n = \frac{\left[\psi_n(m\mathrm{d}_s) \psi_n(\mathrm{d}_s) \right] (1-m)}{\left[\psi_n(m\mathrm{d}_s) \xi_n(\mathrm{d}_s) \right] (1-m)}, \tag{4.13}$$

where $\psi_n(\mathrm{d}_s) = \mathrm{d}_s j_n(\mathrm{d}_s)$ and $\xi_n(\mathrm{d}_s) = \mathrm{d}_s h_n^{(1)}(\mathrm{d}_s)$ with $j_n(\mathrm{d}_s)$ and $h_n^{(1)}(\mathrm{d}_s)$ as the spherical Bessel function and spherical first kind Hankel function, respectively.

4.3.2 Analysis of the Interaction of Incident Light with Suspended Dust Particles

In UM tunnels, when a light beam interacts with an air molecule (Rayleigh scattering) or a suspended dust particle (Mie scattering), the path that this light beam follows until it reaches the optical receiver is modified. The variable that describes this change is the deflection angle θ_s, as can be seen in the geometric pattern of the scattering effect in Figure 4.2. θ_s is determined by the angular distribution of scattering, namely the scattering phase function $p(\theta_s)$. Specifically, the generalized Rayleigh scattering phase function is expressed as

$$p_{ray}(\theta_s) = \frac{3\left[1 + 3\gamma + (1-\gamma) cos^2(\theta_s)\right]}{16\pi(1+2\gamma)}, \tag{4.14}$$

where $\gamma = \delta/(2-\delta)$ is an atmospheric parameter. On the other hand, the Mie scattering phase function can be represented by the generalized Henyey-Greenstein function as follows:

$$p_{mie}(\theta_s) = \frac{1-g^2}{4\pi} \left[\frac{1}{\sqrt{(1+g^2-2g cos(\theta_s))^3}} + \frac{g(3cos^2(\theta_s)-1)}{2\sqrt{(1+g^2)^3}} \right], \tag{4.15}$$

where g is an asymmetric atmospheric factor expressed as

$$g = \frac{\int_0^\infty G(r_{\mathrm{d}}, \lambda, m) n(r_{\mathrm{d}}) \mathrm{d}r_{\mathrm{d}}}{\int_0^\infty n(r) \mathrm{d}r_{\mathrm{d}}}, \tag{4.16}$$

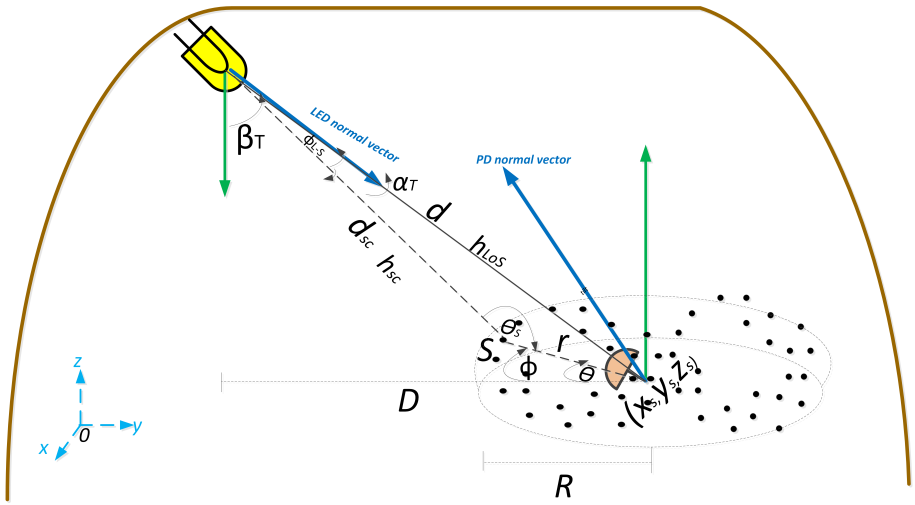

Figure 4.2: Proposed hemispherical scatterers spatial distribution around the PD for the downlink Cartesian/spherical coordinates relating the LED, an arbitrary dust particle, and the PD.

and G is obtained by

$$G(r_{\mathrm{d}}, \lambda, m) = \frac{4}{\mathrm{d}_s^2 Q_{sca}} \sum_{n=1}^{\infty} \left[\frac{n(n+2)}{n+1} (a_n a_{n+1} + b_n b_{n+1}) + \frac{2n+1}{n(n+1)} (a_n b_n) \right]. \tag{4.17}$$

Finally, to consider the entire effect of the interaction of the light beam with dust particles and air molecules, the joint effect of Rayleigh and Mie scattering must be modeled as a Bernoulli distribution. Therefore, the total scattering phase function $p_{total}(\theta_s)$ along with its respective PDF are expressed as

$$p_{total}(\theta_s) = \frac{k_{sca}^{Ray}}{k_{sca}} p_{ray}(\theta_s) + \frac{k_{sca}^{\mathrm{Mie}}}{k_{sca}} p_{\mathrm{mie}}(\theta_s), \tag{4.18}$$

$$f_{sca}(\theta_s) = p_{total}(\theta_s) \sin(\theta_s). \tag{4.19}$$

4.3.3 The 3D Dust Particles Distribution Model

In this subsection, we present the 3D dust particles distribution model. Figure 4.2 shows the three-dimensional geometric outline of the UM scenario that relates the LED, the distribution of the dust particles (scatterers) around the receiver, and the PD. Although only one scatter is shown in the Figure 4.2 for better understanding, there are N dust particles around the receiver. Consequently, the expressions obtained are applied to the total number of scatterers that make up the distribution. In this context, for a better description of the scenario, the following preliminary and general assumptions about dust particles were considered:

1. An optical link (transmission path) from the LED to the PD interacts with a single dust particle, being considered an SB scattering model.
2. Suspended dust particles in the UM environment are spherical and uniformly distributed in the mining tunnel, which theoretically tends to infinite.

3. Dust particles behave as reflective isotropic scatterers with similar scatterer coefficients and uniform random phases.

Based on the features, behavior, and distribution of dust particles in UM tunnels and as a baseline to establish a scattering component included in the UM-VLC channel model, we present a random and independently distributed scatterer distribution within a hemispheric 3D region. This distribution is spatially located around the helmet of the mining worker where the PD is located, which is the central point of the hemispheric area as shown in Figure 4.2.

For simplicity and mathematical convenience, the spatial distribution function of the hemispheroid will be derived considering initially, a uniform general spherical probability distribution/density function, which is expressed as follows

$$f_{x,y,z}^{(sp)}(x_s, y_s, z_s) = \frac{(a+1)r^a}{4\pi R^{(a+1)}}, \tag{4.20}$$

where R is the sphere radius, r is the distance from the scatterer S to the PD, and $a \geq 0$ is the shape factor. In our case, to obtain a spherical 3D shape, we consider a value of $a = 2$. Therefore expression (4.20) is reformulated as follows

$$f_{x,y,z}^{(sp)}(x_s, y_s, z_s) = \frac{3r^2}{4\pi R^3}. \tag{4.21}$$

It is important to mention that outside the spherical region where the scatterers are distributed $f_{x,y,z}^{(sp)} = 0$. The distribution denoted in expression (4.21) can be easily transformed to derive the corresponding distribution for the hemispheric case considering the following premises:

- $f_{x,y,z}^{(sp)} = 0$ for all underground azimuth angle (ϕ). Therefore, $\phi \notin [0, \pi]$.
- $f_{x,y,z}^{(sp)}/2$ for any distribution parameterized by ϕ. Therefore, $\phi \in [\pi, 2\pi]$.

In this context, the PDF of the 3D hemispherical distribution of the dust particles is defined as

$$f_{x,y,z}^{(he)}(x_s, y_s, z_s) = \frac{3r^2}{2\pi R^3}. \tag{4.22}$$

4.3.4 Joint Distribution of the Arrival Time and the Arrival Angle of the Scattering Downlink Link

As mentioned above, although there are N scatterers uniformly distributed within the hemispheric region, for our analysis, a scatterer (denoted by S) is considered in a random position (x_s, y_s, z_s) in the Cartesian coordinates and (r,θ,ϕ) in the spherical coordinates, where $r \geq 0$ the elevation angle (θ) is defined for $0 \leq \theta \leq \pi$ and ϕ is defined for $\pi \leq \phi \leq 2\pi$.

Cartesian-Spherical Coordinates Transformations

As can be seen in Figure 4.2, an arbitrary scatterer will have spherical coordinates (r,θ,ϕ). Therefore, based on the geometric characteristics of the stage and for convenience in handling

the notation, the spherical coordinates related to the Cartesian coordinates (x_s, y_s, z_s) are expressed as follows

$$(x_s, y_s, z_s) = (r\cos\phi, r\sin\phi\cos\theta, r\sin\phi\sin\theta), \tag{4.23}$$

$$r = \sqrt{x_s^2 + y_s^2 + z_s^2}, \tag{4.24}$$

$$\theta = \arctan\left(\frac{z_s}{y_s}\right), \tag{4.25}$$

$$\phi = \arccos\left(\frac{x_s}{r}\right) = \arccos\left(\frac{x_s}{\sqrt{x_s^2 + y_s^2 + z_s^2}}\right). \tag{4.26}$$

Furthermore, based on the premise that any Cartesian-defined PDF function can be expressed in terms of spherical coordinates, we can restructure the $f^{(he)}_{x,y,z}(x_s, y_s, z_s)$ expression as follows

$$f^{(he)}_{r,\theta,\phi}(r,\theta,\phi) = \left.\frac{f^{(he)}_{x,y,z}(x_s, y_s, z_s)}{|J(x_s, y_s, z_s)|}\right|_{\substack{x_s = r\cos\phi \\ y_s = r\sin\phi\cos\theta \\ z_s = r\sin\phi\sin\theta}}, \tag{4.27}$$

where $J(x_s, y_s, z_s)$ is the Jacobian transformation given by

$$J(x_s, y_s, z_s)\Big|_{\substack{x_s = r\cos\phi \\ y_s = r\sin\phi\cos\theta \\ z_s = r\sin\phi\sin\theta}} = \begin{vmatrix} \frac{\delta x_s}{\delta r} & \frac{\delta x_s}{\delta\theta} & \frac{\delta x_s}{\delta\phi} \\ \frac{\delta y_s}{\delta r} & \frac{\delta y_s}{\delta\theta} & \frac{\delta y_s}{\delta\phi} \\ \frac{\delta z_s}{\delta r} & \frac{\delta z_s}{\delta\theta} & \frac{\delta z_s}{\delta\phi} \end{vmatrix}^{-1} = -(r^2\sin\phi)^{-1}. \tag{4.28}$$

Hence, by evaluating expression (4.27) and including expression (4.28) in it, we obtain the expression of $f^{(he)}_{r,\theta,\phi}$ independent of θ as follows

$$f^{(he)}_{r,\theta,\phi}(r,\theta,\phi) = r^2\sin\phi f^{(he)}_{x,y,z}(x_s, y_s, z_s) = r^2\sin\phi f^{(he)}_{x,y,z}(r\cos\phi, r\sin\phi\cos\theta, r\sin\phi\sin\theta). \tag{4.29}$$

Derivation of the Arrival Time and Arrival Angle Joint PDF

By defining τ as the arrival time of the signal that travels from the LED to the PD, The total length of the optical communication path from the LED to the dust particle and then to the PD is given by

$$r + \mathrm{d}_{sc} = c\tau, \tag{4.30}$$

where d_{sc} is the distance between scatterer S and the LED and c is the speed of light. By using consine law and trigonometric equations, r can be given as

$$\mathrm{d}_{sc} = \sqrt{D^2 + r^2 - 2Dr\sin\theta\cos\Phi}, \tag{4.31}$$

where D is the separation distance between the LED and the PD on the y-axis. Hence, r can be obtained from (4.30) and (4.31) as

$$r = \frac{(c\tau)^2 - D^2}{2\,(c\tau - D\sin\theta\cos\Phi)}, \tag{4.32}$$

The variable τ can be incluided in the expression (4.27) in order to determinate the arrival time and arrival angle joint PDF, $f^{(he)}_{\tau,\theta,\phi}(\tau,\theta,\phi)$, which is expressed as

$$f^{(he)}_{\tau,\theta,\phi}(\tau,\theta,\phi) = \left.\frac{r^2\sin\phi f^{(he)}_{x,y,z}(x_s,y_s,z_s)}{|J(r,\theta,\phi)|}\right|_{r=\frac{(c\tau)^2-D^2}{2(c\tau-D\sin\theta\cos\Phi)}}. \tag{4.33}$$

where the Jacobian transformation $J(r,\theta,\phi)$ is given by

$$J(r,\theta,\phi) = \left|\frac{\delta r}{\delta\tau}\right|^{-1} = \frac{2(c\tau+D\sin\theta\cos\phi)^2}{c\left[(c\tau)^2+2c\tau D\sin\theta\cos\phi+D^2\right]}. \tag{4.34}$$

Substituting (4.34) into (4.33), we can obtain $f^{(he)}_{\tau,\theta,\phi}(\tau,\theta,\phi)$ as

$$f^{(he)}_{\tau,\theta,\phi}(\tau,\theta,\phi) = \frac{c\left[(c\tau)^2-D^2\right]^2\left[(c\tau)^2+2c\tau D\sin\theta\cos\phi+D^2\right]\sin\phi}{8(c\tau+D\sin\theta\cos\phi)^4} f^{(he)}_{x,y,z}(x_s,y_s,z_s). \tag{4.35}$$

Finally, by replacing the expression of r (equation (4.32)) in (4.21) and including this result within (4.35), we can obtain the joint PDF of the arrival time and the arrival angle only in terms of the variables of interest τ, θ, and ϕ as follows

$$f^{(he)}_{\tau,\theta,\phi}(\tau,\theta,\phi) = \frac{c\left[(c\tau)^2-D^2\right]^2\left[(c\tau)^2+2c\tau D\sin\theta\cos\phi+D^2\right]\sin\phi}{8(c\tau+D\sin\theta\cos\phi)^4} \times \frac{3r^2}{2\pi R^3}, \tag{4.36}$$

$$f^{(he)}_{\tau,\theta,\phi}(\tau,\theta,\phi) = \frac{3c\left[(c\tau)^2-D^2\right]^4\left[(c\tau)^2+2c\tau D\sin\theta\cos\phi+D^2\right]\sin\phi}{64\pi(c\tau+D\sin\theta\cos\phi)^4\left(c\tau-D\sin\theta\cos\Phi\right)^2 R^3}. \tag{4.37}$$

4.3.5 UM-VLC Channel Component Produced by Scattering

We assume that each scatterer S introduces a coefficient G. This coefficient can be determined mathematically as $G = \overline{\rho}(\lambda)/N$ [10]. However, since the interaction of light with dust particles is probabilistic, it is necessary to include in this gain the PDF of the total scattering phase function. Therefore, G is redefined as

$$G(\theta_s) = \frac{\overline{\rho}(\lambda) f_{sca}(\theta_s)}{N}. \tag{4.38}$$

Since the interaction of light with dust particles is considered as a VLC channel component produced by the optical signal reflection until it reaches the receiver and based on the typical Lambertian VLC channel modeling, the mathematical expressions for the DC gain and the CIR of the UM-VLC channel component produced by dust particles can be written as

$$H_{sca} = \lim_{N\to\infty}\sum_{n=1}^{N}\frac{A_p(m+1)G(\theta_s)}{2\pi(r+\mathrm{d}_{sc})^2}\cos^m(\phi_{L-S})\cos(\theta)rect\left(\frac{\theta}{\Theta}\right), \tag{4.39}$$

$$h_{sca}(t) = \lim_{N\to\infty} \sum_{n=1}^{N} \frac{A_p(m+1)G(\theta_s)}{2\pi(r+\mathrm{d}_{sc})^2} \cos^m(\phi_{L-S}) \cos(\theta) rect\left(\frac{\theta}{\Theta}\right) \delta\left(t - \frac{r+\mathrm{d}_{sc}}{c}\right), \quad (4.40)$$

where A_p is the PD physical active area, $m = -1/log_2\left[cos(\Phi_{1/2})\right]$ represents the Lambertian mode number of the LED, which is a function of semi-angle at half power ($\Phi_{1/2}$) of the LED, Θ is the PD FoV, ϕ_{L-S} is the radiance angle measured between the normal vector to the LED surface and the vector from the LED to the scatterer S, and $\delta(\cdot)$ is a unit-area Dirac delta function.

Furthermore, the total power received by the PD due to the luminous intensity emitted by the LED can be described as

$$P_r = R_{PD} P_t h_m + n_m, \quad (4.41)$$

where R_{PD} is the PD responsivity, and P_t is the emitted optical power by the LED.

Finally, The SNR is computed by using the metric P_r, whose expression is given as

$$SNR = \frac{P_r^2}{\sigma_s^2 + \sigma_t^2}, \quad (4.42)$$

4.4 Results and Discussions

In this section, we simulate, implement, and present theoretical results obtained by computer software in terms of multiple evaluation parameters of wireless communication systems based on the proposed theoretical channel model in order to examine the capacity, behavior, and performance of the UM-VLC system. Furthermore, we make a fair comparison with the UM-VLC channel model and its scenario developed in [10]. Among the parameters that are validated are the CIR, the received power, the RMS delay spread, the SNR, and the BER. Both the parameters of the simulation model that were used in this manuscript as well as the description of the UM scenario are presented in Table 4.1.

Table 4.1: UM-VLC system simulation parameters.

UM simulation scenario	**Values**	**References**
Tunnel Parameters		
Dimensions $(w \times l \times h)$	$(3 \times 6 \times 5)$ m	
Coordinates of the LED (x, y, z)	$(0.5 \times 3 \times 4.5)$ m	
Coordinates of the PD (x, y, z)	$(1 \times 3 \times 1.8)$ m	
Channel parameters		
Absorption coefficient, (Q_{abs})	1.3	[103]
Atmospheric parameter, γ	0.017	[10]
Atmospheric parameter, g	0.72	[10]
Atmospheric parameter, f	0.5	[10]
AWGN power spectral density (A/Hz)	2.5×10^{-23}	[25]
LED rotation angle, α_{i} (°)	45	[105]
LED tilt angle, β_{i} (°)	45	[105]
Noise bandwidth (MHz)	100	[107]
PD rotation angle, α_{i} (°)	45	[105]
PD tilt angle, β_{i} (°)	45	[105]
Scatterer reflection coefficient, ρ_s	0.1	[103]
Scattering coefficient, (Q_{sca})	0.4	[103]
Sphere radius, R (m)	1	[41, 42]
Wall reflection coefficient, ρ_w	0.6	[105]
Wall rotation angle, α_w (°)	U[0,180]	[105]
Wall tilt angle, β_w (°)	U[0,180]	[105]
VLC transceiver parameters		
Average transmitted power, P_t (W)	5	[103]
Band-pass filter of transmission	1	[12]
Dust concentration, C (mg/m^3)	15	[99, 100]
Dust particle radius, r_{d} (μm)	U[0.2,2]	[99, 100]
FoV, Θ (°)	70	[103]
Gain of the optical filter	1	[103]
Lambertian mode number, m	1	[41, 42]
LED wavelength, λ (nm)	580	[103]
Modulation type	OOK	[15]
Modulation bandwidth (MHz)	50	[15]
Modulation index	0.3	[15]
Optical filter bandwidth (nm)	340 to 694.3	[103]
Optical filter center wavelength (nm)	580 ± 2	[103]
Optical filter full width half max (nm)	10 ± 2	[103]
Physical active area, A_p (cm^2)	1	[12]
Reflective element area, ΔA_w (cm^2)	1	[10]
Refractive index, m_s	1.5	[12]
Responsivity, R_{PD} (A/W)	0.53	[12]
Semi-angle at half power, $\Phi_{\mathrm{i}1/2}$ (°)	60	[103]

4.4.1 Channel Impulse Response

Using LoS, NLoS, and scattering ray tracing methodology, we determine the detected power and path lengths from the LED to the PD for each ray. Then, these data are processed to produce the UM-VLC CIR curves.

In the context of analyzing the effect on the complete UM-VLC channel model of the number of dust particles in the hemispherical distribution, Figure 4.3 shows the CIR for different values of N. Figure 4.3(a) compares the UM-VLC CIRs for values of 40 and 60 dust particles with the UM-VLC reference scenario developed in [10]. We can observe that with the value of 60 dust particles considered in the hemispherical distribution, there is a decrease in the magnitude of the UM-VLC CIR and a greater temporal dispersion of its components compared to the curve for N=40. If we compare both curves with the UM-VLC reference scenario, we notice a decrease in the magnitude of the CIRs due to the more precise modeling of the scattering that is achieved with the hemispherical distribution of dust particles. On the other hand, Figure 4.3(b) compares the UM-VLC CIRs for N values of 100, 150, and 200 dust particles. We can notice that for the values of N=150 and N=200 the maximum values of the UM-CIR are similar. Therefore, it could be considered that for values greater than 150 dust particles, the UM-VLC CIR has similar behavior. This is because the scattering component is not the only factor that is influencing the CIR. The full UM-VLC channel model is influenced by random LED and PD orientations, non-regular walls, and shadowing. As a general finding, it could be considered that when we increase the value of N, the light scattering affects the LoS component to a greater extent, in terms of magnitude and time.

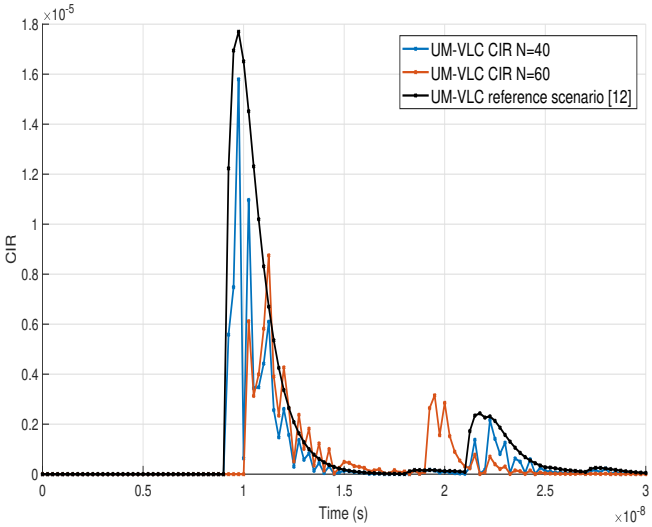

(a)

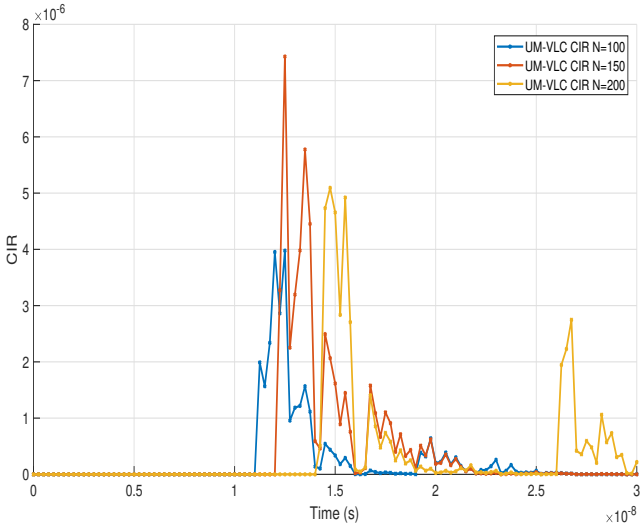

(b)

Figure 4.3: UM-VLC CIR curves for (**a**) 40 and 60 dust particles in the hemispheric area, and UM-VLC reference scenario [10], and (**b**) 100, 150, and 200 dust particles in the hemispheric area.

The specific approach and analysis of the scattering component based on the variation of N values are presented in Figure 4.4. Here, N was varied between values of 20 and 200 dust particles in order to observe their behavior and differences in the CIR curves. It is possible to notice that for all the values of N chosen, the temporal behavior of the CIR curves is the same. Therefore, we can denote that the hemispherical distribution has the same behavior regardless of the value of N. However, and confirming the finding in Figure 4.3, we can observe that for values of N greater than 120, the CIR curves have similar magnitudes, which vary between them by a factor of 0.2×10^{-9}. For a better comparative interpretation of the CIRs curves shown in Figure 4.4, we can verify the maximum magnitude values of the

CIRs by varying N in Table 4.2.

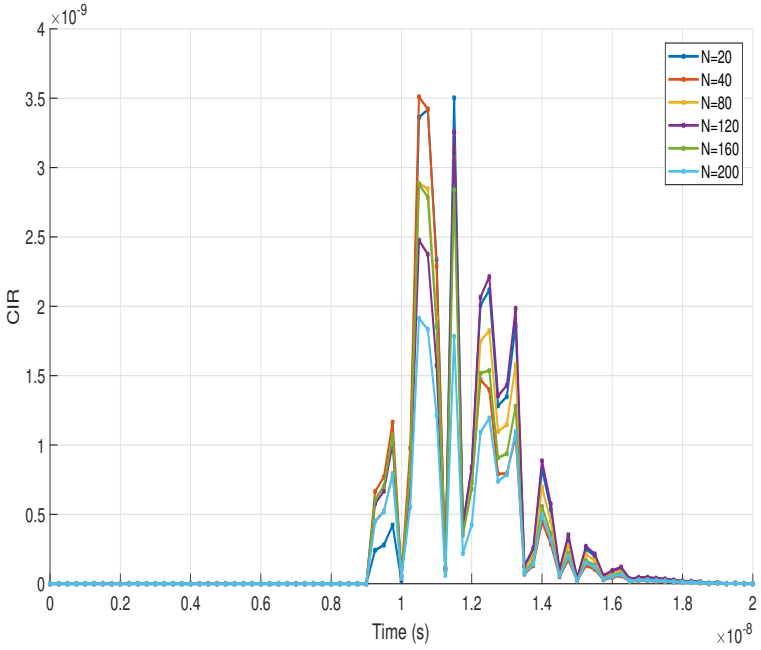

Figure 4.4: CIR of the scattering component with different values of N in the evaluated UM scenario.

Table 4.2: Maximum CIR values for each value of N

N	CIR maximum value
20	$3.53\times10^{-}9$
40	$3.45\times10^{-}9$
80	$3.18\times10^{-}9$
120	$2.83\times10^{-}9$
160	$2.55\times10^{-}9$
200	$2.23\times10^{-}9$

4.4.2 Received Power

Figure 4.5 shows the empirical CDFs of the power received by the PD in the UM scenario for values of N between 40 and 200, which is computed based on the equation (5.13). Furthermore, in each graph, we insert the power received distribution in the UM scenario. We evaluate the received power by keeping the z coordinate of the PD with a value of 1.8 m because it is a typical position value of communication devices in these scenarios. Also, P_t is set to 5 W, to provide constant illumination in the tunnel.

Compared with the CDF and distribution of the received power obtained in the work presented in [10] (see Figure 4.5(f)), the maximum and minimum values of the received power obtained in this study for all the values of N are smaller. This finding implies that the

derived hemispherical dust particle distribution model presents a greater similarity with a real UM scenario since the negative effect of scattering on the received power is more noticeable. In fact, if we compare the CDFs and distributions of received power for the chosen values of N, we can notice that if we increase the value of N, the effect on the decrease of the received power is greater, even though the power distribution remains quite irregular for all values of N.

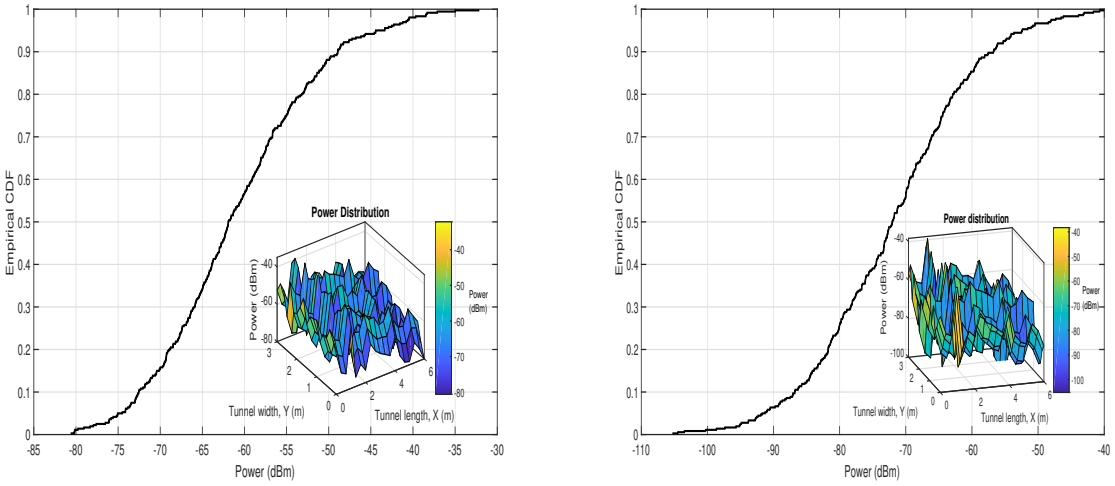

(a)

(b)

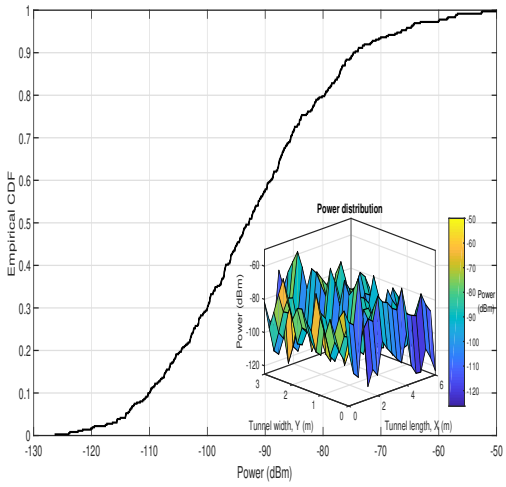

(c)

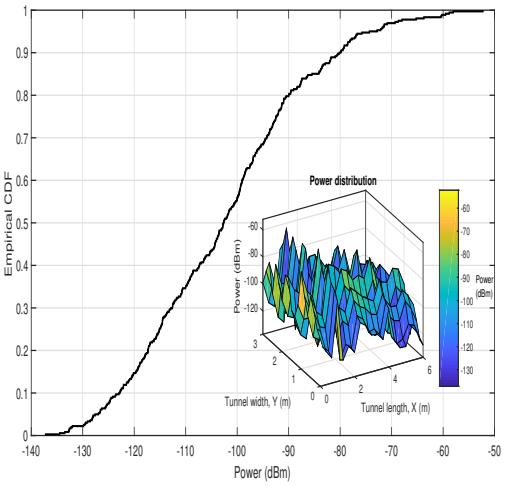

(d)

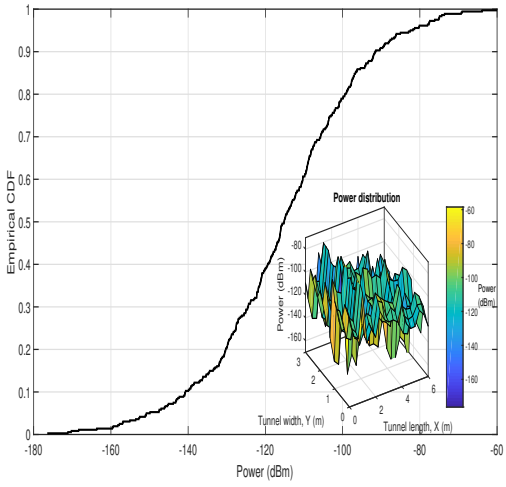

(e)

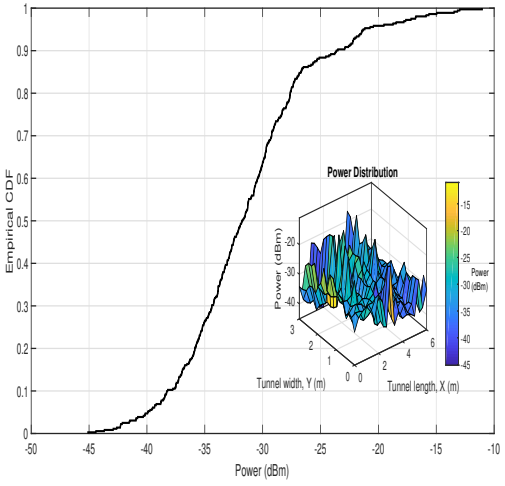

(f)

Figure 4.5: Empirical CDF and distribution of the received power in the UM-VLC scenario with (**a**) 40, (**b**) 60, (**c**) 100, (**d**) 150, (**e**) 200 dust particles in the hemispheric area, and (**f**) UM-VLC reference scenario [10].

4.4.3 Signal to Noise Ratio

The complete UM-VLC model and the effect on it of the scattering channel component together with the presented hemispherical distribution is also evaluated by implementing the SNR metric, which is calculated based on equation (4.42) and presented as empirical CDF curves. As we can see in the expression (4.42), the received power is used to compute the SNR. Therefore, the dependence of the SNR on the received power and its trend is reflected in the CDFs curves obtained. In this context, Figure 4.6 shows the empirical CDFs of the SNR for different N values between 40 and 200 dust particles.

Based on these curves, several important findings are highlighted. We observe that the best SNR performance of the UM-VLC system is obtained when N=40 and the worst performance is obtained when N=200. This reaffirms the idea based on the results of the previous subsections, which implies that as the value of N increases, the performance of the UM-VLC system decreases. However, for values of N=100 and N=150 and for an SNR between 27 and 29 dB, the CDF curves have similar behavior. This behavior allows us to infer that, between these SNR values, the effect of increasing dust particles is not decisive. We must also remember that not only scattering channel component is evaluated, but we also evaluate the UM-VLC channel with all the environmental factors that affect it.

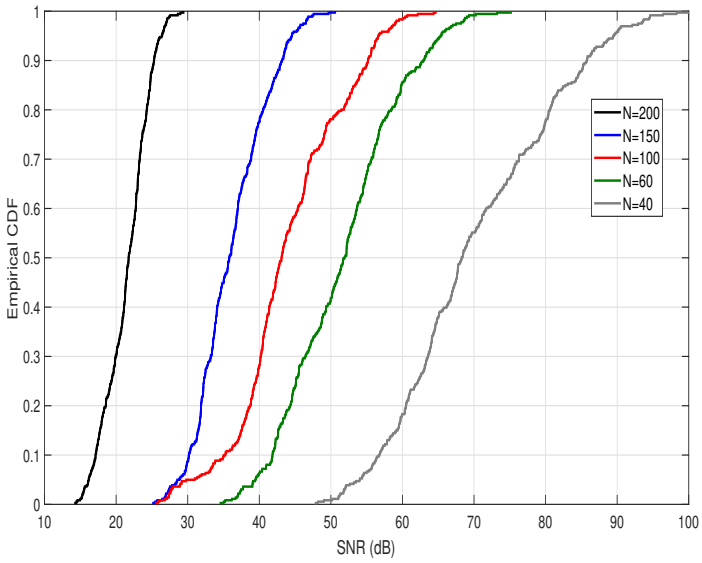

Figure 4.6: Empirical CDF of the SNR obtained for different values of N in the hemispheric area of the UM-VLC scenario evaluated.

4.4.4 Delay Spread

The RMS delay spread is a fundamental metric in wireless communications, which allows us to measure the effect of multi-path propagation in this type of system. In our case, it will allow us to evaluate the multi-path effect of the UM-VLC channel components in the UM environment since this model has components that generate temporal dispersion, which degrades the channel bandwidth. The irregular tunnel walls and dust particles in the environment generate multiple random reflections and scattering of the original light signal.

These effects cause splitting of the signal that propagates through the channel in different paths and distances, which arrive at the PD in a different period of time and induce a delay. The time difference between the arrival of signals at the PD and the particular delay after the arrival of the first light signal, which is usually the LoS component, is declared as excess delay τ_p.

The temporal dispersion has a direct relation with the UM-VLC CIR. Therefore, the RMS delay spread of the UM-VLC channel can be expressed as

$$D_{RMS} = \sqrt{\frac{\sum_{p=0}^{P}(\tau_p - \mu_{RMS})^2 \; h_{mp}^2}{\sum_{p=0}^{P} h_{mp}^2}}, \tag{4.43}$$

where h_{mp}^2 represents the sum of samples numeric of all the channel components that form it with a maximum number of samples P and the mean delay spread μ_{RMS}, which is given by [41]

$$\mu_{RMS} = \frac{\sum_{p=0}^{P} \tau_p \; h_{mp}^2}{\sum_{p=0}^{P} h_{mp}^2}. \tag{4.44}$$

The behavior of the RMS delay spread metric is plotted in terms of empirical CDFs and distributions in the UM-VLC scenario by varying the N values between 40 and 200 dust particles, as can be seen in Figure 4.7. If we compare the result of RMS delay spread obtained in work [10] (see Figure 4.7(f)), with any of the curves and distributions obtained in Figure 4.7, we can notice that the numerical values obtained in this manuscript for any value of N are higher. This finding would also contribute to the deduction that the model of hemispherical dust particles presented in this work is closer to the reality of the UM-VLC scenario because the light signal has a more evident time delay. Although all RMS delay spread distributions for all N values share the same random trend in the UM scenario, we can observe that the higher the N values, the RMS delay spread values also tend to grow.

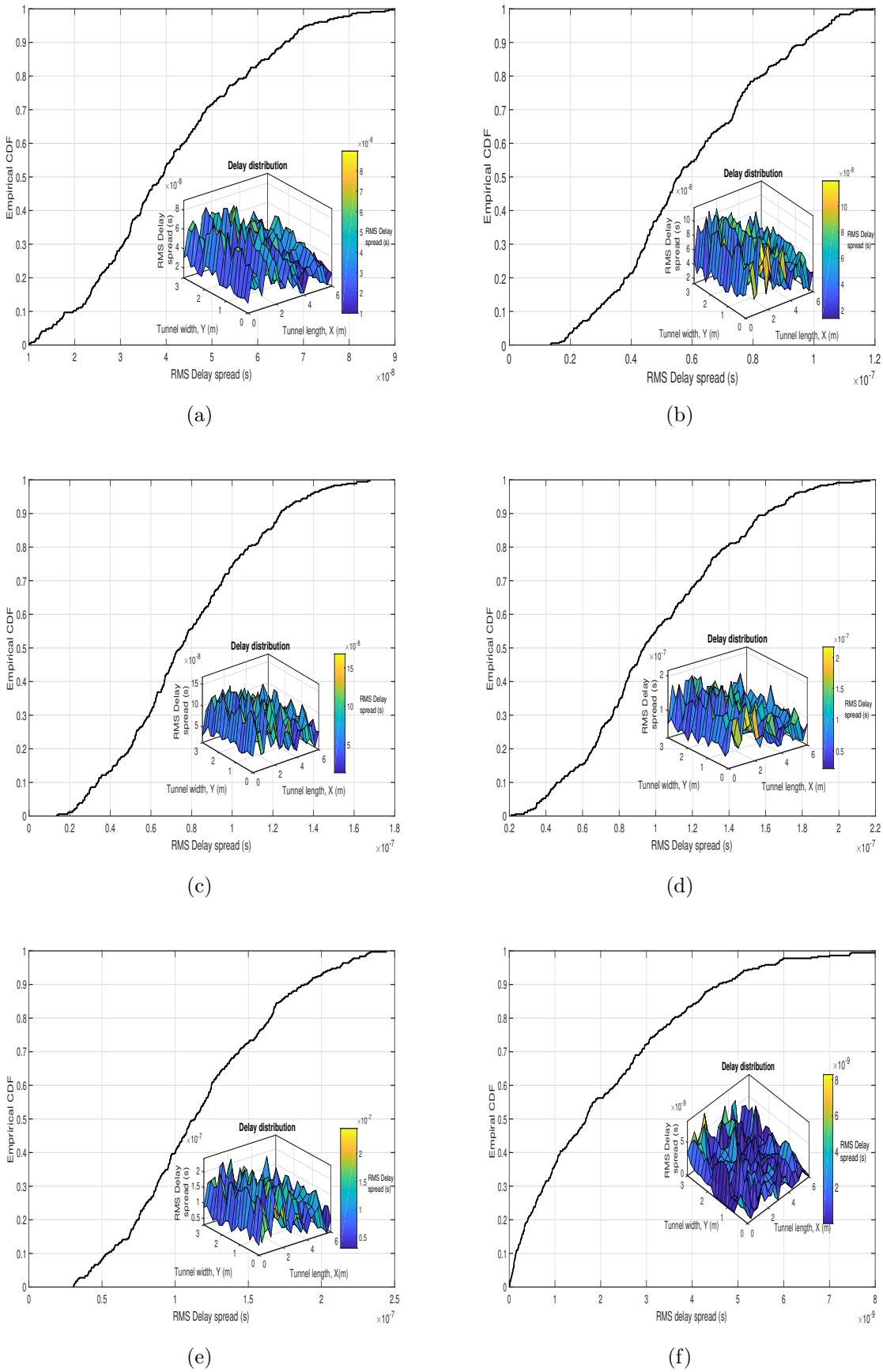

Figure 4.7: Empirical CDF and distribution of the RMS Delay spread in the UM-VLC scenario with (**a**) 40, (**b**) 60, (**c**) 100, (**d**) 150, (**e**) 200 dust particles in the hemispheric area, and (**f**) UM-VLC reference scenario [10].

4.4.5 Bit Error Rate

A very important metric that allows us to evaluate the performance of the complete UM-VLC system is the BER. By using this metric we can find the number of bits that have been altered by the effects of the mining environment, including the effect of scattering by dust particles. This evaluation is carried out using Monte Carlo simulations and integrating the features of the UM tunnel and the UM-VLC channel model. the LED transmission is based on the PHY-I mode together with the OOK modulation, which is described in the IEEE 802.1.5.7 standard. On the other hand, the PD reception employs asynchronous symbol-by-symbol detection [104, 105].

Figure 4.8 shows the BER curves obtained for different values of N applied to the hemispherical distribution of dust particles in the UM-VLC scenario and the UM-VLC reference scenario [10]. It is important to emphasize that the curve obtained from the UM-VLC reference scenario is the one that presents the best performance, due to the fact that the implemented scattering model is basic and unrealistic (2D disk-shaped distribution model) [10]. However, if we compare the curves determined with the UM-VLC model using the hemispherical distribution of dust particles, we can clearly see in Figure 5.5 that the BER curve with the best performance is the one that implements a value of N=40. This result was quite expected by all the factors analyzed in the previous subsections. On the other hand, for values of N=150 and N=200, the system presents the worst performance in terms of BER. This result allows to reinforces the criterion of the dependence of the UM-VLC system performance in terms of the number of dust particles that exist in the proposed hemispherical distribution model. Finally, it was verified that the performance of the UM-VLC system not only depends on the scattering phenomenon, but also on the other physical variables proper to the general UM-VLC channel model.

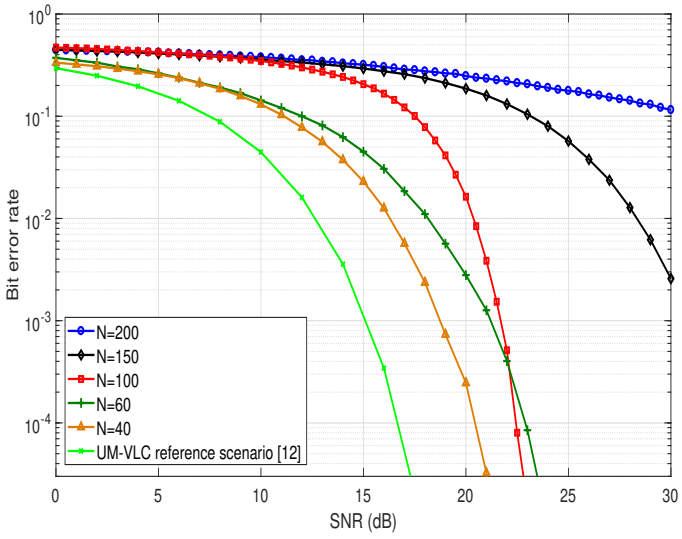

Figure 4.8: BER curves for different values of N in the hemispheric area of the evaluated UM-VLC scenario and the UM-VLC reference scenario [10].

4.5 Conclusions

In this paper, we present an analysis of a SISO UM-VLC system with dust particles suspended in the UM environment and atmospheric parameters. Furthermore, and as the main contribution of this manuscript, we propose a hemispherical 3D dust particle distribution model that more accurately represents the UM hostile environment. The mathematical modeling and the derivation of the statistical parameters of this scatter distribution model allows to present a more coherent scattering channel component produced by the dust particles and to establish a precise and compact general mathematical model of the UM-VLC channel. The performance of the dust particle distribution analytical framework and the improvement of the UM-VLC channel model are evaluated and verified in a UM-VLC system based on computational numerical simulations based on the IEEE 802.1.5.7 standard by varying the number of distributed dust particles in terms of CIR, received power, SNR, RMS delay spread, and BER. The findings based on the CIR are relevant to verify that the temporal dispersion for any number of dust particles is higher compared to similar works in the literature. However, when comparing the curves with values of N=150 and N=200, we observe that they are very similar (approximately between 4 $\times 10^{-6}$ and 5 $\times 10^{-6}$ at their maximum values). These results demonstrate that as the amount of suspended dust particles increases, the CIR decreases in magnitude. The results of the received power, SNR, and RMS delay spread are presented as empirical CDFs and distributions in the UM scenario by varying the number of dust particles. These findings reaffirm that the 3D hemispherical dust particle distribution model derived in this article describes more accurately the UM scenario with respect to basic dust particle distributions found in the literature. This is due to the fact that the real interaction of the light with the scatterers, in general, worsens the performance of the UM-VLC system since the power received and the SNR decrease, and greater time delays are generated. Finally, the system has a better performance in terms of BER when fewer dust particles are considered. On the other hand, the worst performance of the curves occurs for values of N=150 and N=200. These findings reinforce the criteria that the system performance depends directly on the number of dust particles found in the distribution implemented in the UM-VLC scenario.

By presenting a more accurate UM-VLC channel model through the enhancement of the channel component produced by scattering, as future work, it is necessary to present solutions that mitigate the problems generated in the UM-VLC system when there is a greater amount of dust particles. Among these solutions are reception mechanisms based on machine learning and angular diversity receivers. Furthermore, we will validate experimentally the UM-VLC channel model including the scattering components and the distribution of dust particles proposed in this article. This experimental test-bed will have all the features of a UM tunnel to verify the behavior of the VLC system in this environment. Furthermore, and as future work, a deeper statistical development (second-order statistics and probability distributions) of the hemispherical distribution of dust particles, the behavior of dust particles when interacting with light, and the UM-VLC scattering channel model component should be evaluated and analyzed.

4.6 Acknowledgements

This work was supported by CODELCO: Concurso Piensa Minería 2021, SENESCYT "Convocatoria abierta 2014-primera fase, Acta CIBAE-023-2014", UDLA Telecommunications Engineering Degree, FICA, UDLA, Competition for Research Regular Projects, year 2021, code LPR21-02, Universidad Tecnológica Metropolitana, and Fondef ID21I10191. This work was partially funded by UCM-IN-21200 internal grant.

Chapter 5

A Novel and Adaptive Angle Diversity-based Receiver for 6G Underground Mining VLC Systems

VLC is considered an enabling technology for future 6G wireless systems. Among the many applications in which VLC systems are used, one of them is harsh environments such as UM tunnels. However, these environments are subject to degrading environmental and intrinsic challenges for optical links. Therefore, current research should focus on solutions to mitigate these problems and improve the performance of UM-VLC systems. In this context, this article presents a novel solution that involves an improvement to the ADRs based on the adaptive orientation of the PDs in terms of the RSSR scheme. Specifically, this methodology is implemented in a hemidodecahedral ADR and evaluated in a simulated UM-VLC scenario. The performance of the proposed design is evaluated using metrics such as received power, user data rate, and BER. Further, our approach is compared with state-of-the-art ADRs implemented with fixed PDs and with the ToA reception method. An improvement of at least 60% in terms of the analyzed metrics compared to state-of-the-art solutions is obtained. Therefore, the numerical results demonstrate that the hemidodecahedral ADR, with adaptive orientation PDs, enhances the received optical signal. Furthermore, the proposed scheme improves the performance of the UM-VLC system due to its optimum adaptive angular positioning, which is done according to the strongest optical received signal power. By improving the performance of the UM-VLC system, this novel method contributes to further consideration of VLC systems as potential and enabling technologies for future 6G deployments.

5.1 Introduction

UM environments pose a series of risks and safety issues that can affect the mine workers during their activities. These issues can be produced by the UM tunnels features, the potentially toxic components, and high temperature, among others [108]. The factors that intervene in these scenarios require establishing reliable communication between the workers and the mining infrastructure, in order to constantly verify their status and support critical applications

for a correct mining operation. For example, localization systems in UM must be designed to work in real-time, monitoring the well-being of each miner and allowing a fast response to any emergency [109]. Furthermore, the external factors of UM tunnels constitute not just a rough environment for the workers, but also an important difficulty to design communication systems. Electromagnetic interference and noise, and signal fading are factors that compromise traditional communication systems. Consequently, a poor BER, delay spread, and limited rate of receiving data impact the operation of such systems [110]. A potential and feasible solution to mitigate these issues can be found in VLC, which uses visible light to establish the communication link. In this context, and according to the progress and use of operating frequencies of 4G and 5G technologies, it is expected that 6G will operate with frequency bands above 50 GHz. Therefore, the use of VLC-based schemes could be a good option as part of the technologies to be deployed in 6G since it operates in the range from 430 THz to 790 THz [111].

There are several advantages of VLC systems over RF communication systems, which also justifies to include VLC as part of the enabling technologies to be considered in the upcoming 6G standard. First, the spectrum is unlicensed and has a wide spectral range that would allow it to achieve high data transmission rates. Second, the light itself can be used as both illumination and communication, which achieves a reduction of costs while satisfying the underground mine norms. Third, the communication link is more secure, because of the reduced coverage range. Despite these benefits, the environmental roughness of UM provokes several challenges from VLC systems. While the literature of VLC indoor systems is extensive [112], the UM-VLC systems do not consider assumptions that are normally used in VLC indoor systems; such as negligible scattering, perpendicular walls, orthogonal transmitters, and receivers, or the lack of shadowing due to mobile objects.

Among other problems identified in the literature in UM-VLC schemes are the low light coverage that exists in tunnels due to the low density of optical transmitters and the effect produced when the optical receivers are in the overlapping area of two adjacent optical cells [94]. These problems decrease the SINR of the receivers considerably, due to poor signal propagation and the existence of strong interference produced by the phenomenon of ICI, which severely degrades the performance of the systems. Furthermore, specifically in UM environments, there are some SINR fluctuations, which are caused by NLoS components, which are due to reflections of the optical signal on irregular tunnel walls. This problem also reduces the system efficiency [60].

In the literature, there are several solutions to efficiently mitigate optical signal propagation issues. Recently, a particular technique, based on the ADR, has been introduced in indoor VLC environments [61]. An ADR consists of multiple narrow FoV PDs which, when combined, result in a large overall FoV and coverage as a single PD. Each of the narrow-FoV PDs can be selected or combined using signal-combining schemes, thereby mitigating the effect of poor signal propagation and reducing the interference effect of ICI-producing signals. Another feature of these PD arrangements is to assume that the PDs orientation is fixed. However, limiting the PDs orientation also limits the flexibility of the applications and does not allow achieving better signal reception. Consequently, due to the hostility of the UM environments towards the VLC system, it is necessary to optimize the orientation and positioning of the PDs in the ADRs to improve the received signal and increase the system

efficiency.

According to the orientation mechanisms reviewed in the literature, the orientation of PDs is commonly estimated by proximity, fingerprints [113], ToA [114], and Received Signal Strength (RSS) mechanisms [92, 97]. In this sense, algorithms based on RSS are the most used due to their high precision and low synchronization requirement. Specifically, one of these is the RSSR algorithm, which estimates the orientation of the target (the PD, in this case) depending on the received optical power. This parameter is affected by the relative distance and angles between the LED and the PD. However, the inherent challenge is to determine the influence of the relative angle between the LED and the PD in the RSSR method, since the PD orientation is commonly random and unknown in practice. Since the study of VLC systems applied to underground mines is considered a new area of application, these solutions have not been tested in these scenarios either.

In the context of these challenges, in the next Subsection, we will present and discuss the most relevant optical receiver orientation methods and algorithms in the state of the art and related works.

5.1.1 Works Related to Receiver Orientation Algorithms and Methods

In general, receiving orientation algorithms are also applied for the location of receivers in a VLC scenario. For example, in [7], a hybrid RSS+Angle of Arrival (AoA) indoor positioning algorithm implemented in VLC is discussed. The interesting feature of this study is that ICI exists in the scenario, so the authors mitigate this problem using a unique frequency address. On the other hand, the authors in [9], present a mathematical model for a 3D positioning system in VLC. For this, they first derive the channel gain as a function of the source and receiver location in Cartesian coordinates. Then, they develop a cost function based on channel gain. In the experimental scenario, they consider receiver tilt, which is similar to UM-VLC environments. The results show that the proposed 3D method is more accurate compared to the 2D method. Along the same lines, the study carried out in [33] proposes a complete location and orientation solution for both the physical layer and the link layer of an indoor VLC system. The authors apply an RSS-based triangulation method for receptor location. In order to separate the optical signal in the receiver, the position of each LED is encoded with a unique location identification using Optical Orthogonal Codes (OOC). In this work, the impact of receiver orientation is also included. Although these works present certain slightly similar characteristics in the VLC scenario applied to underground mines, they do not consider all the variables of a mining tunnel. They also do not use RSS algorithms to orient receivers according to the best channel gain or power received, but rather present the solutions to locate a receiver in the indoor scenario.

Under these precedents, few works have investigated the application of methods based on RSS or RSSR to efficiently target a PD or array of PDs and achieve better performance in the VLC system. In [6], the authors employ an array-based receiver of multidirectional PDs pointing in different directions and propose a 3D localization algorithm together with the array of PDs. This work uses the relative orientations of the PDs with respect to the receiver and the RSSR to mitigate the influence of the absolute orientation of the receiver. Although

the work applies reception diversity to estimate PD positions, its focus is the location of the receiver, so it does not optimize its orientation. Furthermore, the applied scenario is an indoor VLC system. Other works only analyze the use of arrays of PDs called ADRs in UM environments in order to improve the reception of the optical signal in these scenarios since it is highly affected by the hostility of the tunnel features and the physical phenomena that occur in the tunnel [22, 93, 94]. However, the ADRs keep the position and orientation of the PDs fixed. This solution alone, although it improves the quality of the reception, in certain locations of the UM tunnel requires mechanisms that automate the orientation of the PDs to obtain a better-received power. In [115], an in-depth analysis of VLC-based localization systems in which forward-facing algorithms are applied is presented. The authors present pioneering and more advanced articles specifically applied to VLC, where they are analyzed and classified according to localization techniques, types of transmitters and receivers, and multiplexing techniques. However, there is still the opportunity to apply these methods in UM-VLC systems. Finally, in [116], a high-coverage algorithm termed enhanced Camera Assisted Received Signal Strength Ratio (eCA-RSSR) positioning algorithm is proposed for Visible Light Positioning (VLP) systems. The basic idea of eCA-RSSR is to utilize visual information captured by the camera to estimate first the incidence angles of visible lights. Based on the incidence angles, eCA-RSSR utilizes the RSSR calculated by the PD to estimate the ratios of the distances between the LEDs and the receiver. The results of the work show that applications based on RSSR implemented in VLC systems have great acceptance and potential application for other environments.

After reviewing the state of the art and analyzing the opportunities for improving solutions in optical signal reception in UM environments, in this article, we propose an adaptive orientation receiver based on an ADR and RSSR orientation scheme adapted to a UM-VLC system with a view to establishing itself as a technology part of the 6G standard. As a base case, we use the hemidodecahedral ADR as a receiver along with the RSSR algorithm in the ADR to obtain the estimate of the optimal angle of incidence and orient the ADR in that direction. The proposed method consists of two phases: the reception of the optical signal by the PDs in the ADR to be compared between them and the estimation of the angle of incidence from the RSSR. The proposed solution allows the improvement of the performance of the UM-VLC system without the limitation of the knowledge of the receiver orientation with an emphasis on the best efficiency of the basic metrics for the evaluation of 6G technologies. Indeed, the proposed solution is evaluated in a UM scenario through computational simulations. Furthermore, it is compared with the pyramidal and hemidodecahedral ADRs of fixed PDs and with the ToA method through the received power, BER, and user data rate metrics. Therefore, the main contributions of this work are presented below:

1. A theoretical analysis and design of an ADR structure with adaptive orientation is proposed in this work. Furthermore, the methodology to estimate the optimum angle of incidence on the receiver, along with its main mathematical expressions are derived.
2. A feasible and practical solution to improve the reception of the optical signal based on the adaptive orientation of the PDs in an ADR using an incidence angle estimation method through the RSSR tool.
3. The evaluation and performance comparison of the presented solution with other typical receiver structures in a UM-VLC scenario in terms of important possible metrics for

6G technologies; such as received power, BER, and user data rate.

5.2 VLC System Model Applied to Underground Mining Environments

VLC systems applied to underground mines have marked differences compared to VLC systems applied to non-mining indoor environments. Among the features included in the modeling for UM-VLC systems are the angular positioning of LEDs and PDs, non-regular walls, and scattering and shadowing phenomena. Therefore, based on the work developed in the mining channel quote, in this Section we briefly describe the components of the VLC system applied to the underground mine, its components and characteristics.

5.2.1 Optical Transmitters and Receivers

As is widely known, in VLC systems we assume that LEDs are a point source of light that follows a Lambertian pattern of radiation. In terms of position and orientation, LEDs in underground mines do not mount directly to the ceiling or point vertically downward. Therefore, in our work we consider a set of I LEDs as optical transmitters. Furthermore, the physical position and the normal vector of an LED i, where $\mathrm{i} = 1, 2, ..., I$, are denoted by $(x_{\mathrm{i}}^T, y_{\mathrm{i}}^T, z_{\mathrm{i}}^T)$ and $\boldsymbol{n}_{\mathrm{i}}^{tilt}$, respectively, as we can see in Fig. 5.1.

On the other hand, we assume PDs as optical receptors, which will be located in an ADR that we will define in the Section 5.3. The PDs are composed of a non-imaging concentrator (lens) and a physical active area A_p. In terms of position and orientation, when we install a PD in a mine worker's helmet, it does not always point vertically upwards, due to the very nature of the worker's movement. Furthermore, the physical position and the normal vector of an PD j, where $j = 1, 2, ..., J$, are denoted by (x_j^R, y_j^R, z_j^R) and $\boldsymbol{n}_j^{tilt}$, respectively, as we can see in Fig. 5.1.

We assume that all LEDs have the same generalized Lambertian radiation pattern; therefore, the radiation intensity pattern $R\mathrm{i}(\phi_{\mathrm{i}j}^{tilt})$ and the term $\cos(\phi_{\mathrm{i}j}^{tilt})$ can be modeled as follows [23]:

$$R\mathrm{i}(\phi_{\mathrm{i}j}^{tilt}) = \begin{cases} \frac{m+1}{2\pi}\cos^m(\phi_{\mathrm{i}j}^{tilt}) & \text{if } -\pi/2 \leq \phi_{\mathrm{i}j}^{tilt} \leq \pi/2 \\ 0 & \text{otherwise} \end{cases}, \tag{5.1}$$

$$\cos(\phi_{\mathrm{i}j}^{tilt}) = \frac{V_{\mathrm{i}-j} \cdot \boldsymbol{n}_{\mathrm{i}}^{tilt}}{\|V_{\mathrm{i}-j}\|\|\boldsymbol{n}_{\mathrm{i}}^{tilt}\|}, \tag{5.2}$$

where $\phi_{\mathrm{i}j}^{tilt}$ is the radiance angle with respect to the normal vector to the LED i, the vector from LED i to PD j is denoted by $V_{\mathrm{i}-j}$, the notation $\|\cdot\|$ denotes the 2-norm, and $\cdot$ represents the product dot operation. Also, for vector concepts, $\|V_{\mathrm{i}-j}\| = \mathrm{d}_{\mathrm{i}j}$, where $\mathrm{d}_{\mathrm{i}j}$ is the Euclidean distance between the LED i and PD j, $\|\boldsymbol{n}_{\mathrm{i}}^{tilt}\|=1$, and $\boldsymbol{n}_{\mathrm{i}}^{tilt}$ can be represented in terms of α_{i} and β_{i} as $\boldsymbol{n}_{\mathrm{i}}^{tilt} = [\sin(\beta_{\mathrm{i}})\cos(\alpha_{\mathrm{i}}), \sin(\beta_{\mathrm{i}})\sin(\alpha_{\mathrm{i}}), -\cos(\beta_{\mathrm{i}})]$, where β_{i} is the tilt angle with respect to the z-axis, which takes values in range of $[90°, 180°)$ and α_{i} is the rotation angle with respect to the x-axis, which is defined in the interval $[0°, 360°)$. Furthermore,

$V_{\mathrm{i}-j} = \left[x_j^R - x_{\mathrm{i}}^T, y_j^R - y_{\mathrm{i}}^T, -\Delta h_{\mathrm{i}j}\right]$, assuming that Δh_{ij} is the difference height between LED i and PD j, that is z_{i}^T-$z_j^R = \Delta h_{\mathrm{i}j}$.

In the receptor side, the effective collection area of the PD j and the term $\cos(\theta_{\mathrm{i}j}^{tilt})$ acquire the form of [23]

$$A_{eff}(\theta_{\mathrm{i}j}) = \begin{cases} A_p cos(\theta_{\mathrm{i}j}^{tilt}) & \text{if } -\Theta/2 \leq \theta_{\mathrm{i}j}^{tilt} \leq \Theta/2 \\ 0 & \text{otherwise} \end{cases}, \tag{5.3}$$

$$\cos(\theta_{\mathrm{i}j}^{tilt}) = \frac{V_{j-\mathrm{i}} \cdot \boldsymbol{n}_j^{tilt}}{\|V_{j-\mathrm{i}}\| \|\boldsymbol{n}_j^{tilt}\|}, \tag{5.4}$$

where $\theta_{\mathrm{i}j}^{tilt}$ is the incidence angle with respect to the normal vector to the PD j, $V_{j-\mathrm{i}}$ is the vector from PD j to LED i, $\|V_{j-\mathrm{i}}\| = \mathrm{d}_{\mathrm{i}j}$, $\|\boldsymbol{n}_j^{tilt}\|=1$, $\boldsymbol{n}_j^{tilt} = [\sin(\beta_j)\cos(\alpha_j), \sin(\beta_j)\sin(\alpha_j), \cos(\beta_j)]$, where β_j is the tilt angle with respect to the z-axis, which takes values in range of $[0°, 90°)$, and α_j is the rotation angle with respect to the x-axis that can be valued in range of $[0°, 180°)$, $V_{j-\mathrm{i}} = \left[x_{\mathrm{i}}^T - x_j^R, y_{\mathrm{i}}^T - y_j^R, \Delta h_{\mathrm{i}j}\right]$, and Θ is the FoV of the PD. The gain of the optical concentrator can be written as $g(\theta_{\mathrm{i}j}) = \eta^2/sin^2(\Theta)$, being η the internal refractive index of the concentrator.

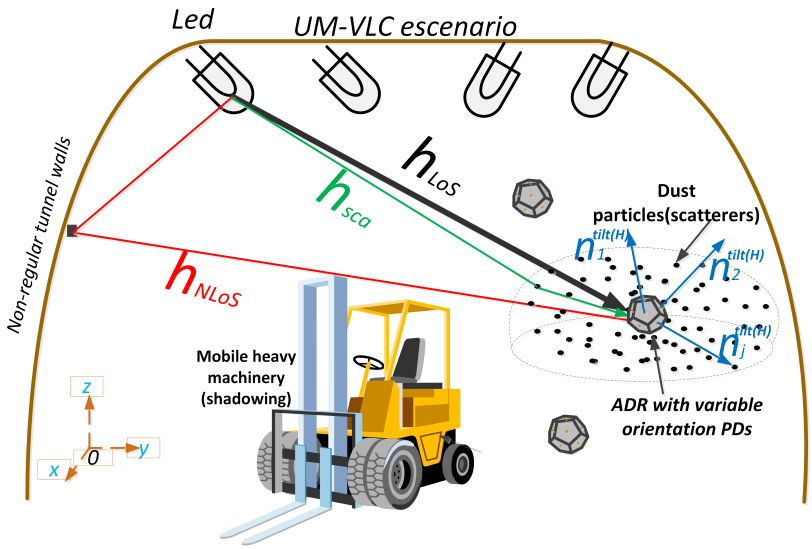

Figure 5.1: UM-VLC propagation scenario with the geometry of optical channel components.

5.2.2 Channel DC Gain

Based on the work done in [23], the UM-VLC channel is modeled by integrating three optical components: the LoS component, the NLoS component, and the scattering component. The LoS component is obtained directly from the LED lighting that falls on the PD. Thus, the LoS link depends on the LED and PD parameters as seen above. In addition, due to the UM infrastructure, in which large machinery and vehicles move through the tunnels, the effect of shadowing within the expression of the UM-VLC channel is considered. This UM scenario

with its components is outlined in Fig. 5.1. By integrating these factors, the DC gain of the LoS optical wireless channel is formulated as follows:

$$H_{LoS,\mathrm{i},j} = \frac{(m+1)A_p}{2\pi \mathrm{d}_{\mathrm{i}j}^{m+3}} \left\{ \left[x_j^R - x_{\mathrm{i}}^T, y_j^R - y_{\mathrm{i}}^T, -\Delta h_{\mathrm{i}j} \right] \cdot [\sin(\beta_{\mathrm{i}})\cos(\alpha_{\mathrm{i}}), \sin(\beta_{\mathrm{i}})\sin(\alpha_{\mathrm{i}}), -\cos(\beta_{\mathrm{i}})] \right\}^m \times \left\{ \left[x_{\mathrm{i}}^T - x_j^R, y_{\mathrm{i}}^T - y_j^R, \Delta h_{\mathrm{i}j} \right] \cdot [\sin(\beta_j)\cos(\alpha_j), \sin(\beta_j)\sin(\alpha_j), \cos(\beta_j)] \right\} G(\theta_{\mathrm{i}j}^{tilt}) rect(\frac{\theta_{\mathrm{i}j}^{tilt}}{\Theta}) P_{\mathrm{i}j}. \tag{5.5}$$

where $rect(\frac{\theta_{\mathrm{i}j}^{tilt}}{\Theta}) = 1$ for $0 \leq \theta_{\mathrm{i}j}^{tilt} \leq \Theta$ and 0 otherwise, $G(\theta_{\mathrm{i}j})$=$T_s(\theta_{\mathrm{i}j})$ $g(\theta_{\mathrm{i}j})$ represents the combined gain of the optical filter and optical concentrator, respectively, and $P_{\mathrm{i}j}$ is a weighting function introduced to consider the random shadowing, which describes the probability that the LoS optical link is not blocked.

On the other hand, as a result of obstacles, and the non-flat and irregular walls of the tunnels, a diffuse component of the transmitted light is reflected by these elements. This effect generates the NLoS component of the VLC channel, termed as H_{NLoS}. A common model for diffuse reflection is the Lambertian reflectance where light is reflected with equal radiance in all directions. However, this NLoS component differs from the NLoS component of non-mining indoor scenarios. The main differences are in the normal vectors of the non-planar walls, which are not orthogonal to the reflective area of the wall, called w. Therefore, these normal vectors ($\boldsymbol{n}_w^{tilt}$) can be described in terms of the tilt angle with respect to the z-axis denoted as β_w, which belongs to the range of $[0°, 180°)$ and the rotation angle with respect to the x-axis denoted as α_w and takes values in range of $[0°, 180°)$.

The incidence angle with respect to the normal vector to the reflective element w and the radiance angle of the light component reaching the reflective element w are symbolized with $\theta_{\mathrm{i}w}^{tilt}$ and ϕ_{wj}^{tilt}, respectively. The angles of incidence and radiance are denoted by θ_{wj}^{tilt} and ϕ_{wj}, respectively, which are measured with respect to the light component that is reflected in the reflective element w and reaches PD j. The effect of the non-flat walls is noticeable in terms of the following cosines: $\cos(\phi_{\mathrm{i}w}^{tilt})$, $\cos(\theta_{\mathrm{i}w}^{tilt})$, $\cos(\phi_{wj}^{tilt})$ and $\cos(\theta_{wj}^{tilt})$ in the following form:

$$\cos(\phi_{\mathrm{i}w}^{tilt}) = \frac{V_{\mathrm{i}-w} \cdot \boldsymbol{n}_{\mathrm{i}}^{tilt}}{\|V_{\mathrm{i}-w}\| \|\boldsymbol{n}_{\mathrm{i}}^{tilt}\|}, \tag{5.6}$$

here, $V_{\mathrm{i}-w}$ is the vector from LED i to w, $\|V_{\mathrm{i}-w}\| = \mathrm{d}_{\mathrm{i}w}$, where $\mathrm{d}_{\mathrm{i}w}$ is the Euclidean distances between LED i and the reflective element w, and $V_{\mathrm{i}-w} = \left[x_w^S - x_{\mathrm{i}}^T, y_w^S - y_{\mathrm{i}}^T, -\Delta h_{\mathrm{i}w} \right]$, assuming that the position of w is (x_w^S, y_w^S, z_w^S), and $\Delta h_{\mathrm{i}w}$ is the difference height between LED i and w.

$$\cos(\theta_{\mathrm{i}w}^{tilt}) = \frac{V_{w-\mathrm{i}} \cdot \boldsymbol{n}_w^{tilt}}{\|V_{w-\mathrm{i}}\| \|\boldsymbol{n}_w^{tilt}\|}, \tag{5.7}$$

where $V_{w-\mathrm{i}}$ is the vector from w to LED i, $\|V_{w-\mathrm{i}}\| = \mathrm{d}_{\mathrm{i}w}$, $\|\boldsymbol{n}_w^{tilt}\|$=1, $\boldsymbol{n}_w^{tilt}$ can be represented in terms of α_w and β_w, that is $\boldsymbol{n}_w^{tilt} = [\sin(\beta_w)\cos(\alpha_w), \sin(\beta_w)\sin(\alpha_w), \cos(\beta_w)]$ and $V_{w-\mathrm{i}} = \left[x_{\mathrm{i}}^T - x_w^S, y_{\mathrm{i}}^T - y_w^S, \Delta h_{\mathrm{i}w} \right]$.

$$\cos(\phi_{wj}^{tilt}) = \frac{V_{w-j} \cdot \boldsymbol{n}_w^{tilt}}{\|V_{w-j}\| \|\boldsymbol{n}_w^{tilt}\|}, \tag{5.8}$$

where V_{w-j} is the vector from w to PD j, $\|V_{w-j}\|$=d_{wj}, where d_{wj} is the Euclidean distance between reflective element w and PD j, and $V_{w-j} = \left[x_j^R - x_w^S, y_j^R - y_w^S, -\Delta h_{wj}\right]$, assuming that Δh_{wj} is the difference height between w and PD j.

$$\cos(\theta_{wj}^{tilt}) = \frac{V_{j-w} \cdot \boldsymbol{n}_j^{tilt}}{\|V_{j-w}\|\|\boldsymbol{n}_j^{tilt}\|}, \tag{5.9}$$

where V_{j-w} is the vector from PD j to w, $\|V_{j-w}\| = \mathrm{d}_{wj}$, and $V_{j-w} = \left[x_w^R - x_j^R, y_w^S - y_j^R, \Delta h_{wj}\right]$.

By including the effect of non-regular walls in the UM-VLC channel model and also consider the shadowing effect, the DC gain of the NLoS optical wireless channel can be calculated by adding all the components arriving at the PD j after being reflected in a surface namely

$$\begin{aligned} H_{NLoS,\mathrm{i},j}^{(1)} = \frac{(m+1)A_p}{2\pi} \sum_{w=1}^{W} \frac{\Delta A_w \rho_w}{\mathrm{d}_{\mathrm{i}w}^{m+3}\mathrm{d}_{wj}^4} \left\{\left[x_w^S - x_{\mathrm{i}}^T, y_w^S - y_{\mathrm{i}}^T, -\Delta h_{\mathrm{i}w}\right] \cdot [\sin(\beta_{\mathrm{i}})\cos(\alpha_{\mathrm{i}}), \sin(\beta_{\mathrm{i}})\sin(\alpha_{\mathrm{i}}), -\cos(\beta_{\mathrm{i}})]\right\}^m \\ \times \left\{\left[x_{\mathrm{i}}^T - x_w^S, y_{\mathrm{i}}^T - y_w^S, \Delta h_{\mathrm{i}w}\right] \cdot [\sin(\beta_w)\cos(\alpha_w), \sin(\beta_w)\sin(\alpha_w), \cos(\beta_w)]\right\} \\ \times \left\{\left[x_j^R - x_w^S, y_j^R - y_w^S, -\Delta h_{wj}\right] \cdot [\sin(\beta_w)\cos(\alpha_w), \sin(\beta_w)\sin(\alpha_w), \cos(\beta_w)]\right\} \\ \times \left\{\left[x_j^R - x_w^S, y_j^R - y_w^S, -\Delta h_{wj}\right] \cdot [\sin(\beta_j)\cos(\alpha_j), \sin(\beta_j)\sin(\alpha_j), \cos(\beta_j)]\right\} G(\theta_{wj}^{tilt}) rect(\frac{\theta_{wj}^{tilt}}{\Theta}) P_{\mathrm{i}w} P_{wj}, \end{aligned} \tag{5.10}$$

where ΔA_w denotes the w^{th} area of the considered reflective element w, whose reflection coefficient is represented by ρ_w, and W is the total number of reflective elements considered in the scenario. In addition, $P_{\mathrm{i}w}$ and P_{wj} are the weighted functions that consider the shadowing effect. These functions are obtained through the same statistical process to obtain $P_{\mathrm{i}j}$ and they represent possible blockages in the optical link between LED i and the reflective element w, and the optical link between w and PD j, respectively.

The last optical component that is included in the UM-VLC channel is the one produced by scattering. This phenomenon is caused by dust particles generated by the work of an underground mine. Therefore, its effect on the UM-VLC channel is direct in terms of magnitude and temporal dispersion. Based on the mathematical expression of the typical Lambertian channel model, the DC gain of the scattering optical wireless channel produced by scattering on the optical path LED i-S_n-PD j, which corresponds to the light beam that travels from the LED i, interacts with the local scatterrer S_n and reaches the PD j, can be written as [23]

$$H_{sca,\mathrm{i},j} = \lim_{N\to\infty} \sum_{n=1}^{N} \frac{A_p(m+1)G_n(\mu)}{2\pi D_{\mathrm{i}-n-j}^2} \cos^m(\phi_{\mathrm{i}-S_n}) \cos(\theta_{S_n-j}) rect\left(\frac{\theta_{S_n-j}}{\Theta}\right), \tag{5.11}$$

where $G_n(\mu)$ is a coefficient introduced by each scatterer S_n, θ_{S_n-j} represents the angle between the vector from the n^{th} scatterer of a set of N scatterers to PD j and $\boldsymbol{n}_j^{tilt}$, $\phi_{\mathrm{i}-S_n}$ is the radiance angle measured between $\boldsymbol{n}_{\mathrm{i}}^{tilt}$ and the vector from LED i to PD j, and the path length $D_{\mathrm{i}-n-j}$ represents the total distance that light travels from the LED i via S_n to the PD j. This path length can be expressed as $D_{\mathrm{i}-n-j} = \mathrm{d}_{\mathrm{i}-S_n} + r_n$, where $\mathrm{d}_{\mathrm{i}-S_n}$ is the distance of the transmitted optical link between the LED i and S_n and r_n is the distance from the n^{th} local scatterer to PD j.

Finally, the overall DC channel gain for UM-VLC systems is the sum of the LoS, NLoS and scattering components, namely

$$H_{miner,\mathrm{i},j} = H_{LoS,\mathrm{i},j} + H^{(1)}_{NLoS,\mathrm{i},j} + H_{sca,\mathrm{i},j}. \tag{5.12}$$

5.2.3 Receiver Optical Power

For the UM-VLC system, we denote as P_t the optical power transmitted by a single LED. For simplicity, we assume that all LEDs in set I transmit the same P_t. Therefore, the optical power received at PD j from LED i is expressed as

$$P_{r,\mathrm{i},j} = R_{PD} P_t H_{miner,\mathrm{i},j} + N_j, \tag{5.13}$$

where $P_{r,\mathrm{i},j}$ is the power received of PD j, R_{PD} is the PD responsivity, and N_j is the additive noise in PD j that includes two types of noise that particularly affect UM environments, shot noise and thermal noise whose variances are denoted as σ^2_{shot} and $\sigma^2_{thermal}$ respectively.

As mentioned in the contributions of the work, one of the objectives of this research is to study the impact of a adaptive orientation receiver applied to the presented UM-VLC system. As such, we will focus on a proposal which will allow us to obtain better system performance in terms of the power received at the receiver through the RSSR parameter. This proposal is based on an array of multidirectional PDs, which exploits the angular diversity of the array and the random orientation of the receiver located on the top of the mining workers' helmets. The following section presents a rigorous mathematical analysis of the proposed receptor structure.

5.3 Adaptive Orientation Receiver

In an effort to improve the performance of VLC systems applied to underground mines and inspired by the characteristics of strong light directionality required in VLC, we propose a solution based on an adaptive orientation receiver.

5.3.1 Adaptive Orientation Receiver Structure

Basically an adaptive orientation receptor consists of multiple PDs connected to a single signal processing chain as shown in Fig. 5.2. We can see that this receiver structure only requires a single TIA, which considerably reduces energy consumption in the optical signal reception and processing stage. In order to present a generalized model, we consider the set of PDs J defined in subsection 5.2.1. For illustrative and demonstrative purposes, these PDs are installed in a hemidodecahedron geometric structure, which is described in detail in Section 4.4. However, our solution can be applied to any geometric structure (pyramidal, hemispherical, etc). Therefore, initially, the PDs point in different directions according to their position in the receiver of hemidodecahedral structure that is installed in the helmet of the mining worker, as we can see in Fig. 5.2.

For ease, we assume that all PDs in the receiver have the same optical characteristics, except for their position and pointing direction. In practice, even though the geometric

structure is physically small, there are unavoidable differences between the positions of the PDs in the receiver. This causes variations between the distance from the LEDs to each PD. However, the distances among PDs are significantly small compared to the distance from the LEDs to the receiving geometric structure, so they are not considered. In addition, we consider that the orientation that the receiver takes will be based on the received power of the LoS component of the total UM DC channel gain, because it contributes with the largest magnitude optical power.

We denote the location of the hemidodecahedric structure as (x^H, y^H, z^H), which according to the assumptions considered will be the common location for all PDs in the receiving structure. Consequently, we can affirm that (x^H, y^H, z^H)=(x_j^R, y_j^R, z_j^R) $\forall j \in [1, J]$, $V_{\mathrm{i}-j} \approx V_{\mathrm{i}} =$ $(x_{\mathrm{i}}^T, y_{\mathrm{i}}^T, z_{\mathrm{i}}^T)$-$(x^H, y^H, z^H)$, $\|V_{\mathrm{i}-j}\| = \mathrm{d}_{\mathrm{i}j} \approx \mathrm{d}_{\mathrm{i}}$, where d_{i} is the Euclidean distance from LED i to the receiving structure. Based on these mathematical considerations, we can approximately rewrite and expand expression (5.13) as

$$
\begin{aligned}
P_{r,\mathrm{i},j} &\approx R_{PD} P_t H_{miner,\mathrm{i},j} + N_j \\
&\approx R_{PD} P_t \left[H_{LoS,\mathrm{i},j} + H^{(1)}_{NLoS,\mathrm{i},j} + H_{sca,\mathrm{i},j} \right] + N_j \\
&\approx R_{PD} P_t H_{LoS,\mathrm{i},j} + R_{PD} P_t H^{(1)}_{NLoS,\mathrm{i},j} + R_{PD} P_t H_{sca,\mathrm{i},j} + N_j \\
&\approx R_{PD} P_t \frac{(m+1) A_p}{2\pi \mathrm{d}_{\mathrm{i}}^{m+3}} \left(V_{\mathrm{i}} \cdot \boldsymbol{n}_{\mathrm{i}}^{tilt} \right)^m \left(V_{\mathrm{i}} \cdot \boldsymbol{n}_j^{tilt} \right) G(\theta_{\mathrm{i}j}^{tilt}) P_{\mathrm{i}} + R_{PD} P_t H^{(1)}_{NLoS,\mathrm{i}} + R_{PD} P_t H_{sca,\mathrm{i}} + N_H \\
&\approx \frac{C}{\mathrm{d}_{\mathrm{i}}^{m+3}} \left(V_{\mathrm{i}} \cdot \boldsymbol{n}_{\mathrm{i}}^{tilt} \right)^m \left(V_{\mathrm{i}} \cdot \boldsymbol{n}_j^{tilt} \right) P_{\mathrm{i}} + R_{PD} P_t H^{(1)}_{NLoS,\mathrm{i}} + R_{PD} P_t H_{sca,\mathrm{i}} + N_H, \qquad (5.14)
\end{aligned}
$$

where C=$\frac{(m+1)A_p}{2\pi} R_{PD} P_t G(\theta_{\mathrm{i}j}^{tilt})$ is a constant, P_{i} is the weighing function that describes the probability that the LoS link between the LED i and the entire receiving structure is blocked, $H^{(1)}_{NLoS,\mathrm{i}}$ and $H_{sca,\mathrm{i}} + N_H$ are the NLoS channel and scattering components between the LED i and the receiver structure respectively, and N_H is the additive noise in the receiver structure.

As mentioned in this section, we will focus mainly on the UM LoS channel component, i.e., the former component of $P_{r,\mathrm{i},j}$. Therefore our analysis and algorithm that we propose below is based on that assumption.

5.3.2 Adaptive Receptor Orientation Scenario

In the proposed algorithm, we assume that there are at least two LEDs within the hemidodecahedral geometric arrangement FoV, which consists of six PDs, five on its lateral faces and one on its upper face, as we can see in Fig. 5.2. However, to generalize with any geometric arrangement, we need at least three PDs, that is, $I \geq 2$ and $J \geq 3$. We also consider that the FOV of the receiving structure is the intersection of the FoV of all the PDs that compose it. We also assume that each LED takes turns transmitting its $(x_{\mathrm{i}}^T, y_{\mathrm{i}}^T, z_{\mathrm{i}}^T)$ and $\boldsymbol{n}_{\mathrm{i}}^{tilt}$ in its assigned time slot through visible light when the optical signal emitted by the LED is within the FoV of the PD, the PD receives the signal and also measures the corresponding received signal power.

As we noted in expression (5.14), the position, rotation and tilt of the LEDs and PDs directly affect the UM-VLC channel and therefore the received power. However, since the LEDs are fixedly installed, we will focus on the positioning of the PDs in the receiver struc-

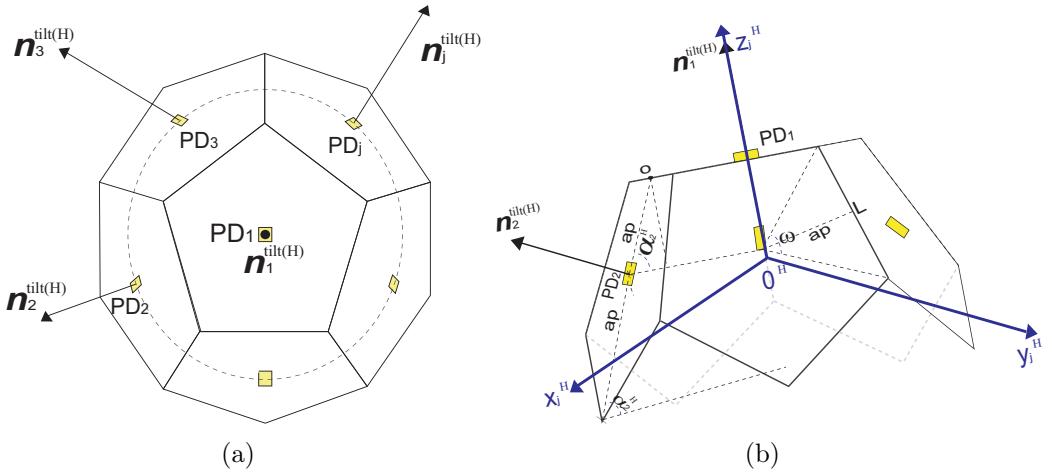

Figure 5.2: General structure of the hemi-dodecahedron ADR with adaptive orientation PDs. **(a)** top view and **(b)** side view.

ture. This positioning affects the incidence angle, as we observe in expression (5.4), with the α_j and β_j angles. Therefore, in the algorithm that we propose, we will first estimate the θ_{ij}^{tilt}, to then obtain the α_j and β_j values, and finally estimate the orientation that the receiving structure must follow.

As illustrated in Fig. 5.1, we employ a Cartesian coordinate system with respect to the tunnel to specify positions of the elements of the system. On the other hand, to estimate θ_{ij}^{tilt}, we need to know the relationships among the different orientations that PDs can take in the receiving structure. However, these orientations are random and unknown if we based on the coordinate system with respect to the tunnel. This problem occurs because the receiving structure can rotate and tilt randomly by the movement of the mining worker's head. In contrast, PDs are initially fixed with respect to the hemidodecahedral receptor structure. Thus, it is necessary to introduce a secondary Cartesian coordinate system with respect to the receiving structure, to specify the PDs orientations.

Based on the system distribution in Fig. 5.1 and 5.2, the origin point of the secondary coordinate system, O^H, is the center of the hemidodecahedron. The x^H-y^H plane coincides with the bottom plane of the hemidodecahedron and the positive axis x^H coincides with the normal direction of the hemidodecahedron. By convention, the inclination angles of the PDs in the geometric structure start from zero. To distinguish and differentiate the vector and position notations with respect to the main coordinate system, in the secondary coordinate system we use the superscript "^{H}" for the respective representation. Therefore, the positions (x_i^T, y_i^T, z_i^T), (x_j^R, y_j^R, z_j^R), and (x^H, y^H, z^H), and the vectors $\boldsymbol{n}_i^{tilt}$, $\boldsymbol{n}_j^{tilt}$, and d_{ij} in the main coordinate system are represents by the positions (x_i^H, y_i^H, z_i^H), (x_j^H, y_j^H, z_j^H), and (x^H, y^H, z^H), and the vectors $\boldsymbol{n}_i^{tilt(H)}$, $\boldsymbol{n}_j^{tilt(H)}$, and d_{ij}^H in the secondary coordinate system.

Considering these details and based on the receptor hemidodecahedron geometry, (x^H, y^H, z^H)=$(0, 0, 0)$, (x_j^H, y_j^H, z_j^H) and $\boldsymbol{n}_j^{tilt(H)}$ are represented as

$$(x_j^H, y_j^H, z_j^H) = \left(ap\left[1 + cos(\alpha_j^H)\right] cos(\beta_j^H), ap\left[1 + cos(\alpha_j^H)\right] \sin(\beta_j^H), \frac{ap\left[1 + cos(\alpha_j^H)\right]}{tan(\alpha_j^H)} \right), \tag{5.15}$$

$$\boldsymbol{n}_j^{tilt(H)} = \left[\sin(\beta_j^H)\cos(\alpha_j^H), \sin(\beta_j^H)\sin(\alpha_j^H), \cos(\beta_j^H)\right], \tag{5.16}$$

$$\alpha_j^H = \begin{cases} 0°, & \text{if } j = 1 \\ \alpha_j, & \text{if } j = 2, \ldots, 6, \end{cases} \tag{5.17}$$

$$\beta_j^H = \frac{2\pi(j-1)}{5} \qquad for \;\; 2 \leq j \leq 6, \tag{5.18}$$

where ap is the apothem of the hemidodecahedron and is represented by $ap = \frac{L}{2tan(\omega/2)}$, with L as the length of the sides of the hemidodecahedron lateral surfaces and w as its central angle. The angles α_j^H and β_j^H are are the angles of rotation and tilt of each PD j with respect to the secondary coordinate system respectively.

5.3.3 Methodology Used to Estimate the Angle of Incidence

To obtain the proper orientation that the receiving geometric structure will be given, we must have a fairly accurate estimate of the direction of the LoS optical link. Therefore, the suitable variable to estimate is the angle of incidence. In this research, we propose the estimation of $\theta_{\mathrm{i}j}^{tilt}$ based on the RSSR metric implemented and analyzed from the reference of the secondary coordinate system.

According to the mathematical expression of received power derived in (5.14), we define in a general way that the approximate RSSR between PD j and any PD q, where j and q belong to the set of PDs J corresponding to the receiving geometric structure, is expressed as

$$\frac{P_{r,\mathrm{i},j}}{P_{r,\mathrm{i},q}} \approx \frac{\frac{C}{\mathrm{d}_\mathrm{i}^{m+3}} \left(V_\mathrm{i} \cdot \boldsymbol{n}_\mathrm{i}^{tilt}\right)^m \left(V_\mathrm{i} \cdot \boldsymbol{n}_j^{tilt}\right) P_\mathrm{i} + R_{PD} P_t H_{NLoS,\mathrm{i}}^{(1)} + R_{PD} P_t H_{sca,\mathrm{i}} + N_H}{\frac{C}{\mathrm{d}_\mathrm{i}^{m+3}} \left(V_\mathrm{i} \cdot \boldsymbol{n}_\mathrm{i}^{tilt}\right)^m \left(V_\mathrm{i} \cdot \boldsymbol{n}_q^{tilt}\right) P_\mathrm{i} + R_{PD} P_t H_{NLoS,\mathrm{i}}^{(1)} + R_{PD} P_t H_{sca,\mathrm{i}} + N_H}, \tag{5.19}$$

In order to obtain simplified analytic expressions based on the direction cosines of the incidence angles between LED i and PDs j and q together with their normal vectors, and expressing them as a function of the Cartesian secondary coordinate system with respect to the receiver, we can rewrite Eq. (5.19) as

$$\frac{P_{r,\mathrm{i},j}}{P_{r,\mathrm{i},q}} \approx \frac{\cos(\theta_{\mathrm{i}j}^{tilt})}{\cos(\theta_{\mathrm{i}q}^{tilt})} = \frac{\boldsymbol{n}_j^{tilt(H)} \cdot \mathrm{d}_{\mathrm{i}j}^H}{\boldsymbol{n}_q^{tilt(H)} \cdot \mathrm{d}_{\mathrm{i}q}^H}, \tag{5.20}$$

where $\mathrm{d}_{\mathrm{i}j}^{H}$ and $\mathrm{d}_{\mathrm{i}q}^{H}$ can be considered approximately equal since they would be almost the same distance from LED i. Therefore, we will define this general distance as $\mathrm{d}_{\mathrm{i}}^{H}$. As mentioned before, to generalize, we define $J \geq 3$ PDs. Therefore, we can obtain for each LED in the system (L 1) independent RSSR equations similar to expression (5.20). For simplicity in the calculations, we consider the RSSR between the first PD and the other PDs in the array to obtain the following expression:

$$\frac{P_{r,\mathrm{i},j}}{P_{r,\mathrm{i},1}} \approx \frac{\boldsymbol{n}_j^{tilt(H)} \cdot \mathrm{d}_{\mathrm{i}}^{H}}{\boldsymbol{n}_1^{tilt(H)} \cdot \mathrm{d}_{\mathrm{i}}^{H}}. \tag{5.21}$$

This expression can be restructured as

$$\left(\boldsymbol{n}_j^{tilt(H)} - \frac{P_{r,\mathrm{i},j}}{P_{r,\mathrm{i},1}} \boldsymbol{n}_1^{tilt(H)}\right)^T \mathrm{d}_{\mathrm{i}}^{H} = 0. \tag{5.22}$$

Since the module of $\mathrm{d}_{\mathrm{i}}^{H}$ does not directly influence the equation, only the direction of of $\mathrm{d}_{\mathrm{i}}^{H}$ is needed. Therefore, we can define the independent RSSR set of equations in matrix form as

$$\mathbf{A}_{\mathrm{i}} \triangleq \begin{bmatrix} \left(\boldsymbol{n}_2^{tilt(H)} - \frac{P_{r,\mathrm{i},2}}{P_{r,\mathrm{i},1}} \boldsymbol{n}_1^{tilt(H)}\right)^T \\ \vdots \\ \left(\boldsymbol{n}_L^{tilt(H)} - \frac{P_{r,\mathrm{i},L}}{P_{r,\mathrm{i},1}} \boldsymbol{n}_1^{tilt(H)}\right)^T \end{bmatrix}_{(L-1)\times 3}, \tag{5.23}$$

$$\mathbf{x}_{\mathrm{i}} \triangleq \mathrm{d}_{\mathrm{i}}^{H}. \tag{5.24}$$

We can express these matrices as a group of homogeneous linear Eqs. defined as

$$\mathbf{A}_{\mathrm{i}}\mathbf{x}_{\mathrm{i}} = 0; \quad subject\ to\ ||\mathbf{x}_{\mathrm{i}}|| = 1. \tag{5.25}$$

Finally, we obtain the linear solution of (5.25) by applying the method of least squares ($\hat{x}_{\mathrm{i}}$). This expression is given by the eigenvector corresponding to the smallest eigenvalue of $\mathbf{A}_{\mathrm{i}}^T\mathbf{A}_{\mathrm{i}}$. Furthermore, since $0 \leq \theta_{\mathrm{i}j}^{tilt} \leq \Theta$, we can infer that $\cos(\theta_{\mathrm{i}j}^{tilt}) \geq 0$. Therefore, the estimate incidence angle can be calculated as

$$\hat{\theta_{\mathrm{i}j}^{tilt}} = \arccos\left(|\boldsymbol{n}_j^{tilt(H)}\hat{\mathbf{x}}_{\mathrm{i}}|\right). \tag{5.26}$$

With the estimate $\hat{\theta_{\mathrm{i}j}^{tilt}}$ value and through mechanical rotation mechanisms, we can optimally orient the PD structure so that it can maximize the power received by the LED.

5.4 Results and Discussion

In this Section, we simulate and present graphical results based on numerical simulations using the Monte Carlo method in Matlab. The findings obtained are based on evaluation

metrics of traditional wireless communication systems. These parameters together with the application of the UM-VLC system allow us to examine the capacity, behavior, and performance of the adaptive orientation receiver solution presented. Furthermore, to validate and compare our proposal with typical state-of-the-art solutions, we make a fair comparison with pyramidal and hemidodecahedral ADRs with fixed PDs and with the ToA method. Among the metrics used to evaluate the presented solution are the power received and the user data rate distributed in the scenario together with the BER. Both the parameters of the simulation model that were used in this manuscript as well as the description of the UM-VLC scenario are presented in Table 5.1.

Table 5.1: UM-VLC system simulation parameters.

UM Simulation Scenario	**Values**	**Ref.**
Tunnel Parameters		
Dimensions ($w \times l \times h$), m	$(3 \times 6 \times 5)$	
Coordinates of the LED (x, y, z), m	$LED_1 = (3, 1.5, 4.5)$, $LED_2 = (3, 3, 4.5)$, $LED_3 = (3, 4.5, 4.5)$, $LED_4 = (-3, 6, 4.5)$	
Channel and element parameters		
AWGN power spectral density (A/Hz)	2.5×10^{-23}	[25]
LED rotation angle, (°)	45	[60]
LED tilt angle, (°)	45	[60]
Noise bandwidth (MHz)	100	[107]
Wall reflection coefficient, ρ_w	0.6	[60]
Wall rotation angle, (°)	U[0,180]	[60]
Wall tilt angle, (°)	U[0,180]	[60]
VLC transceiver parameters		
Average transmitted power, P_t (W)	5	[103]
Band-pass filter of transmission	1	[94]
FoV, Θ (°)	70	[103]
Gain of the optical filter	1	[103]
Lambertian mode number, m	1	[41, 42]
LED wavelength, λ (nm)	580	[103]
Modulation type	OOK	[67]
Modulation bandwidth (MHz)	50	[67]
Modulation index	0.3	[67]
Optical filter bandwidth (nm)	340 to 694.3	[103]
Optical filter center wavelength (nm)	580 ± 2	[103]
Optical filter full width half max (nm)	10 ± 2	[103]
Physical active area, A_p (cm^2)	1	[94]
Reflective element area, ΔA_w (cm^2)	1	[23]
Refractive index, m_s	1.5	[94]
Responsivity, R_{PD} (A/W)	0.53	[94]
Semi-angle at half power, (°)	60	[103]

5.4.1 Distribution of the Received Power

Figure 5.3 shows the distribution of the power received by the hemidodecahedral ADR with PDs with adaptive orientation, with a fixed orientation, and with the ToA method as well as the distributions for pyramidal ADRs with fixed PDs and with the ToA method. These distributions are calculated based on equations 14 and 21. We evaluate the received power by keeping the coordinate z of the ADRs with a value of 1.8 m because it is a typical position value of the communication devices in these scenarios. Also, P_t is set to 5 W, to provide constant lighting in the UM tunnel.

In the first instance, we can see that by implementing the ToA method in the hemidodecahedral ADR, we improve the power received compared to the same ADR with fixed PDs by 20%. In addition, by implementing this method in the pyramidal ADR and comparing it with its pair with fixed PDs, we also improve the power received by 10%. However, if we compare them with our proposal and take as a precedent that the hemidodecahedral ADR by itself improves the efficiency of the received signal with respect to the pyramidal ADR, we can observe that the presented proposal (Figure 5.3(a)) presents the best performance in terms of the evaluated metric compared to its evaluative ADR peers. Indeed, we have power values between -45.3 dBm and -81.2 dBm for the hemidecahedral ADR with PDs with adaptive orientation. This effect of improvement of the received power is due to the automatic orientation that the PDs have in the array. Therefore, wherever the ADR is in the UM-VLC scenario, it will always point its PDs in the direction that maximizes the power gain.

5.4.2 Distribution of the User Data Rate

The user data rate is a metric that allows us to validate the maximum and minimum data transfer values that are received by the ADRs. Figure 5.4 shows the UDR distribution for the proposed solution based on the adaptive orientation of PDs in the hemidodecahedral ADR comparing it with the ADRs with the ToA method and fixed PDs. We can clearly see that, as with the received power, the best system performance is achieved with the proposal presented in this article in terms of the UDR. As we can see in the Figure 5.4(a), UDR values between 19.2 Mbps and 185.4 Mbps are obtained, having full coverage in the UM-VLC scenario. In table 5.2 we can also verify the improvement percentage of our solution compared to state-of-the-art solutions. These results allow us to deduce and re-validate that the improvement in the system performance is due to the fact that, in addition to the quantity and distribution of PDs in the hemidodecahedral geometry, this ADR architecture is better used and optimized in conjunction with the adaptive orientation PDs methodology according to the better reception of the optical signal.

5.4.3 Bit Error Rate

An important metric that evaluates the complete UM-VLC system performance including the proposed solution is the BER. By using this metric we can find the number of bits that have been altered either by the effects of the UM environment or by inefficiency in receiving solutions. This evaluation is carried out using Monte Carlo simulations and by considering the LED transmission base on the PHY-I mode with the OOK modulation [60, 104].

Figure 5.5 shows the BER curves obtained for the hemidodecahedral solution with adap-

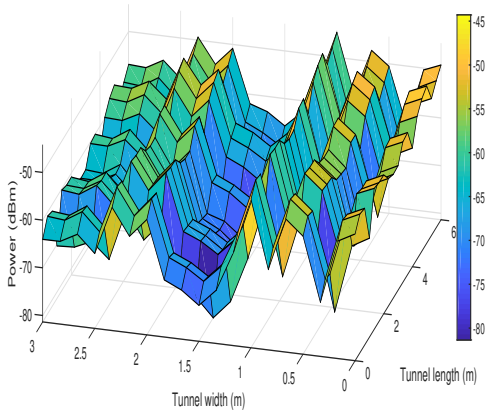

(a)

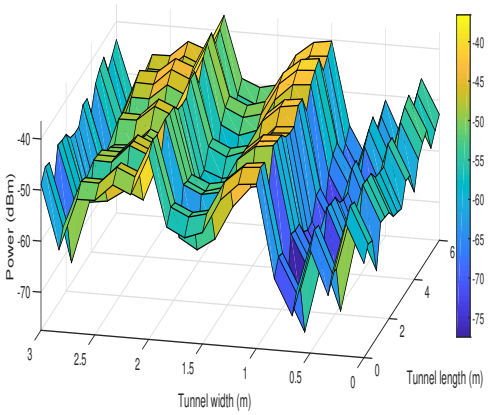

(b)

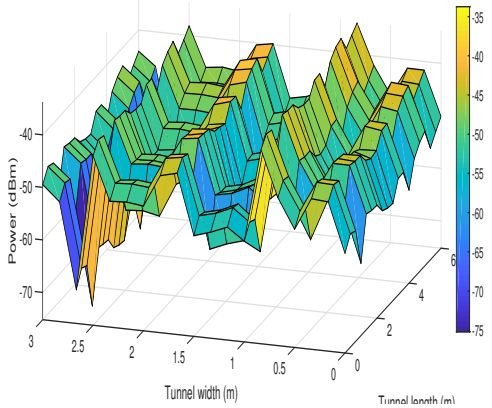

(c)

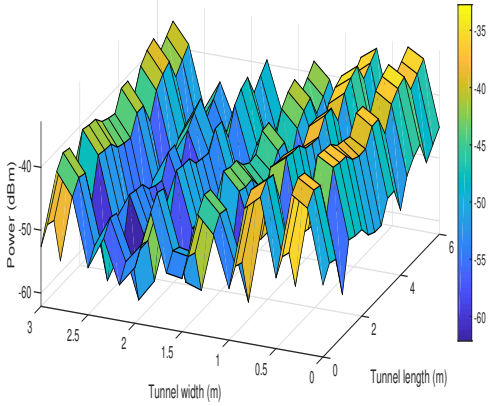

(d)

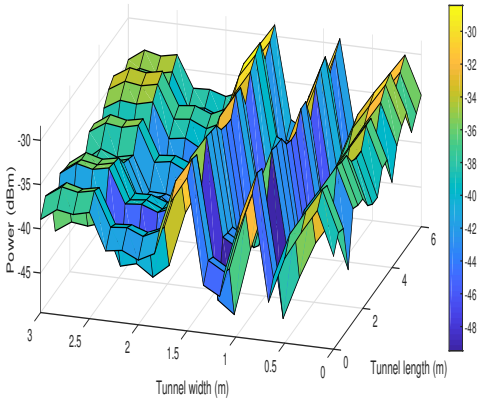

(e)

Figure 5.3: (**a**) hemidodecahedral ADR with PDs with adaptive orientation, (**b**) hemidodecahedral ADR with PDs fixed, (**c**) hemidodecahedral ADR with the ToA method, (**d**) pyramid ADR with the ToA method, and (**e**) pyramid ADR with the PDs fixed.

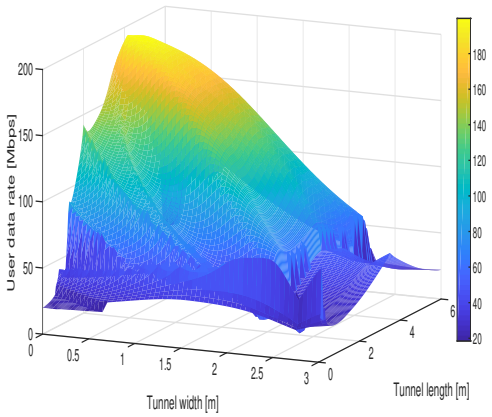

(a)

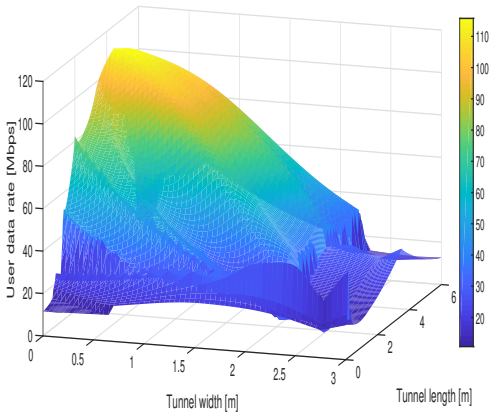

(b)

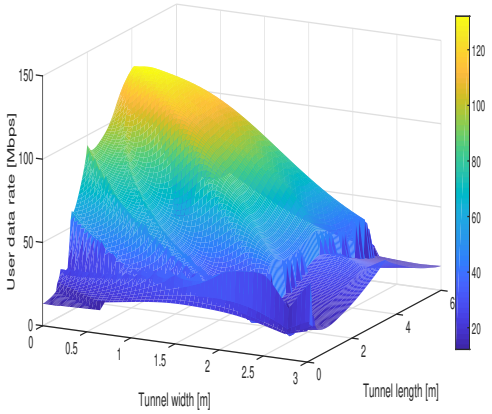

(c)

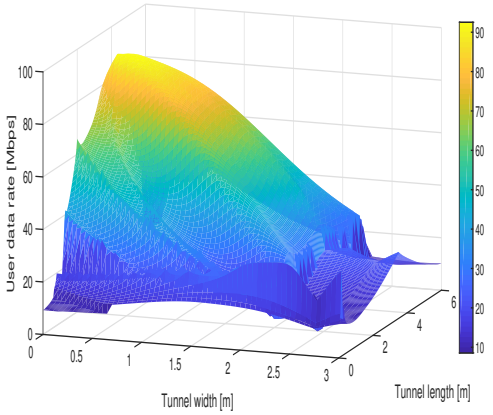

(d)

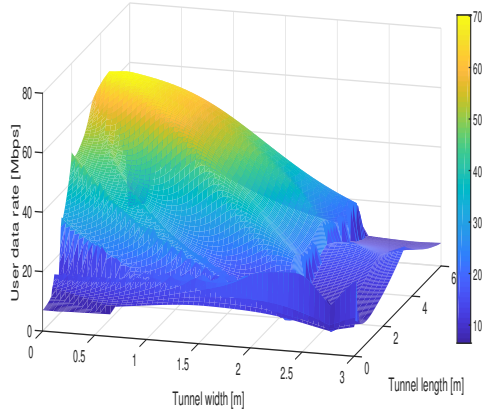

(e)

Figure 5.4: (**a**) hemidodecahedral ADR with adaptive orientation PDs, (**b**) hemidodecahedral ADR with PDs fixed, (**c**) hemidodecahedral ADR with the ToA method, (**d**) pyramid ADR with the ToA method, and (**e**) pyramid ADR with fixed PDs.

Table 5.2: Percentage improvement in the user data rate of the proposed solution compared to state-of-the-art solutions.

State-of-the-art solutions	**Hemidodecahedral ADR with PDs with adaptive orientation**
Hemidodecahedral ADR with PDs fixed	61.1%
Hemidodecahedral ADR with the ToA method	50.4%
Pyramid ADR with the ToA method	101.3%
Pyramid ADR with the PDs fixed	160.2%

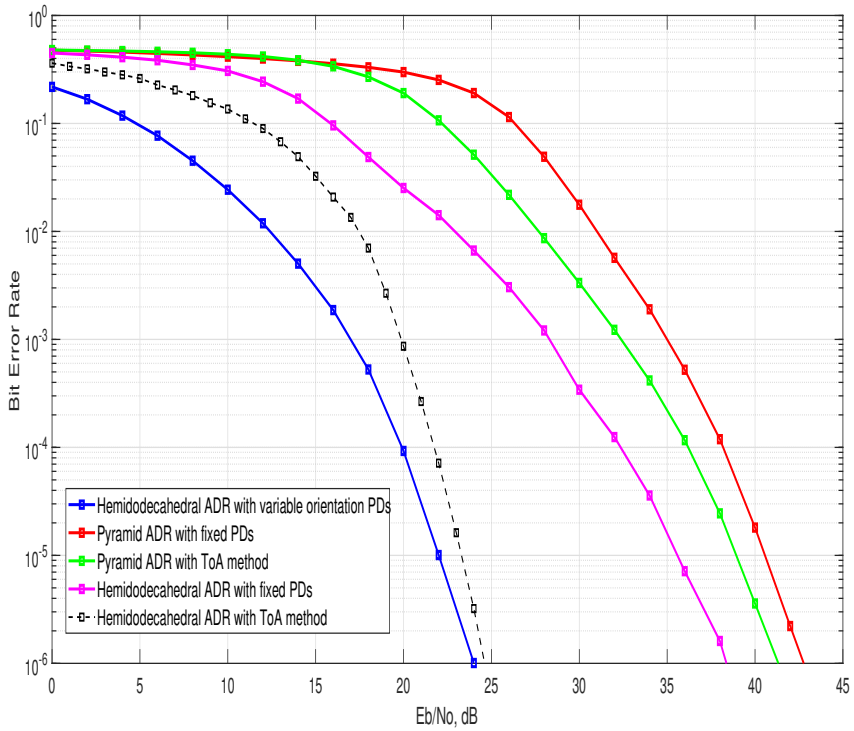

Figure 5.5: BER curves for the hemidodecahedral ADR with adaptive orientation PDs and the state-of-the art ADRs architectures.

tive orientation PDs and the ADRs of the state of the art in the proposed UM-VLC scenario. It is important to note that, like the other metrics previously analyzed, the curve that describes the BER of the solution presented in this article is the one that presents the best performance. Indeed, we can verify that when compared to the pyramidal ADR, its performance based on BER improves notably. This gain is due to the orientation and positioning efficiency of the PDs in the hemidodecahedral ADR due to the implemented methodology. This result would also allow us to deduce that the proposed solution mitigates to a certain extent the harmful effects of the UM-VLC environment, which drastically degraded the BER. Furthermore, given the automatic oriented granularity of the PDs in the ADR, the ICI produced is mitigated since the interference caused by LEDs whose received power is not optimal is minimized.

5.5 Conclusions

This article presents a novel and adaptive angle diversity-based receiver for 6G UM-VLC Systems. The performance of the adaptive orientation solution based on the RSSR scheme, which is implemented in a hemidodecahedral ADR is verified. The architecture and methodology of the proposed solution was analyzed mathematically and geometrically in the reception stage of an UM-VLC scheme through computational simulations. The evaluation was performed in terms of received power, user data rate, and BER, and its numerical results were compared with the pyramidal and hemidecahedral ADRs solutions with fixed PDs and considering the ToA orientation method. The findings derived from the described metrics demonstrate that the solution proposed in this manuscript perform better than typical ADRs in UM-VLC schemes, consequently, improves the fulfillment of the communication goals of the UM-VLC system. Specifically, for the user data rate distribution in the UM-VLC scenario, the solution proposed in this article presents an improvement of over 50% with respect to the state-of-the-art solutions used for comparison in this work. On the other hand, when we analyze the BER curves, the proposed solution enhances the BER of the system compared to typical ADR solutions. Therefore, the enhancement of the system is due to the mitigation of ICI, and the external factors that affect the UM-VLC environment due to the efficient, as well as adaptive and automatic orientation that the PDs have in the hemidodecahedral ADR. The improvement in signal reception performance implies an improvement in the operation of the UM-VLC system, which increases the chances of being considered as part of the enabling technologies for 6G wireless communications systems.

As future work, a physical and experimental implementation and validation of the solution presented in this manuscript will be considered along with electromechanical mechanisms that generate the automatic adaptive orientation of the PDs. Furthermore, the behavior and performance of the created solution will be verified in other VLC environments based on specific channel models for these environments.

5.6 Acknowledgements

This work was supported by Project FONDECYT Regular 1211132. This work was partially supported by CODELCO: Concurso Piensa Minería 2021; SENESCYT "Convocatoria abierta 2014-primera fase, Acta CIBAE-023-2014"; UDLA Telecommunications Engineering Degree

FICA, UDLA; Competition for Research Regular Projects, year 2021, code LPR21-02; UCM-IN-21200 internal grant, Universidad Tecnológica Metropolitana, and Fondef ID21I10191.

Chapter 6

Conclusions

6.1 General Conclusions

I proposed a novel channel model that incorporates essential factors that influence the quality of the VLC link in underground mines. First, I included features such as an arbitrary positioning and orientation of the optical transmitter and receiver, tunnels with irregular walls, shadowing by large machinery, and scattering by dust clouds are considered. Second, I integrated these factors into a single modeling framework that lends itself to the derivation of compact mathematical expressions for the overall DC gain, the impulse response, the root mean square delay spread, and the received power of the proposed VLC channel model. Then, I validated the analytical results by computer simulations. I demonstrated with these results that the rotation and tilt of the transmitter and receiver, as well as the tunnels' irregular walls, have a notorious influence on the magnitude and temporal dispersion of the VLC channel's LoS and NLoS components. Furthermore, I also observed that the shadowing reduces the LoS component's magnitude significantly. Finally, the findings also showed that scattering by dust particles contributes slightly to the total VLC channel gain, although it generates a large temporal dispersion of the received optical signal.

I derived analytical expressions of the statistical distribution of the underground mining visible light communication square-channel gain considering scattering, shadowing, and a random position and orientation of the receiver. I employed these expressions to compute the system's bit error probability considering shot and thermal noises, on-off keying modulation, as well as perfect and imperfect channel state information at the receiver side. I validated the results obtained for the BEP by computer simulations for various UM-VLC scenarios. I observed a close agreement between the analytical and simulated curves. Furthermore, I demonstrated that the performance of the UM-VLC system improves by increasing the FoV and/or SNR. Indeed, for an FoV value of 45° for both the UM-VLC system with perfect CSI and imperfect CSI, I obtained the best performance in terms of BEP. On the other hand, in terms of the UM-VLC system with imperfect CSI, I noted that the BEP curves saturate for higher values of SNR due to lower values of FoV, specifically in the case of 45°. Finally, I also observed that the performance of the UM-VLC system increases significantly for higher values of SNR, specifically in the case of 20 dB.

I presented an in-depth study of the interaction of optical links with dust particles suspended in the UM environment and the atmosphere. Then, I analytically derived a hemispherical 3D dust particle distribution model, along with its main statistical parameters. I developed and derived a more realistic scattering channel component and an enhanced UM-VLC channel model. I evaluated the performance of the proposed UM-VLC system using computational numerical simulations following the IEEE 802.1.5.7 standard in terms of CIR, received power, SNR, RMS delay spread, and BER. I demonstrated that the hemispherical dust particle distribution model is more accurate and realistic in terms of the metrics evaluated if this distribution model is compared with other typical models found in the literature. Finally, I observed that the performance of the UM-VLC system is negatively affected when the number of dust particles suspended in the environment increases.

I designed a novel solution that involves an improvement to the Angle Diversity Receivers based on the adaptive orientation of the Photo-Diodes in terms of the Received Signal Strength Ratio scheme. I implemented this methodology in a hemidodecahedral ADR and then I adapted this architecture in a simulated UM-VLC scenario. I evaluated the performance of the proposed design using metrics such as received power, user data rate, and Bit Error Rate. Further, I compared this approach with state-of-the-art ADRs implemented with fixed PDs and with the ToA reception method. I observed that there is an improvement of at least 60% in terms of the analyzed metrics compared to state-of-the-art solutions. Therefore, these numerical results demonstrated that the hemidodecahedral ADR, with adaptive orientation PDs, enhances the received optical signal. I demonstrated that the proposed scheme improves the performance of the UM-VLC system due to its optimum adaptive angular positioning, which is done according to the strongest optical received signal power. Finally, I highlighted that by improving the performance of the UM-VLC system, this novel method could contribute to further consideration of VLC systems as potential and enabling technologies for future 6G deployments.

6.2 Future Work

In addition to future work topics presented in the conclusion section of each main chapter, an interesting extension of this work includes two approaches that are summarized below:

UM-VLC System Simulation Approach

The mechanisms and models derived in this thesis presented will be verified by using realistic conditions for in-depth validation and performance evaluations. To account for realistic conditions, the simulated environments will integrate hardware-in-the-loop techniques, in which the channel is fed with real-time effects that emulate the expected conditions of the VLC channel in UM environments, as we can see in Figure 6.1. The hardware-in-the-loop settings will be adjusted according to data resulting from the experimental test bed and will be implemented using the specialized SDR equipment, namely to create channel impairments such as scattering, shadowing, and attenuation as well as to re-create the actual characteristics of a VLC link in UM environments.

The use of hardware-in-the-loop techniques to properly recreate the link conditions to

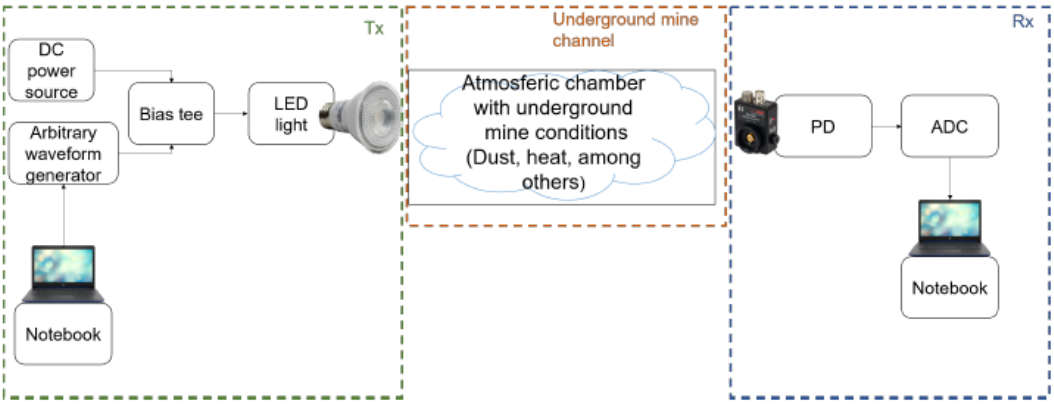

Figure 6.1: Block diagram of the proposed experimental setup.

UM environments by using SDRs will allow evaluation of the VLC link in applications such as positioning and localization, sensor network monitoring, and UM-IoT. It is important to point out that VLC will be used for the downlink, whereas RF-based technologies could be used for the uplink due to RF systems do not interfere with VLC systems and vice versa.

UM-VLC System Experimental Validation

In order to perform an experimental demonstration of the channel characteristic's effects on the VLC link for underground mines, an experimental test bed will be implemented using VLC transceivers, electro-optical components, and a UM tunnel prototype to emulate the physical characteristics of underground mines, as we can see in Figure 6.1. The experimental test bed will be adopted to validate the channel impulse response and bit error rate BER metrics of the UM-VLC channel model. Furthermore, the experimental test bed will be used to collect data and to construct empirical channel models subject to diverse environmental conditions. These data will be used to adjust the settings of the hardware-in-the-loop techniques in our system simulations. The experimental test bed to be implemented in the project follows the design principles in the facilities of the Czech Technical University in Prague and it is depicted in Figure 6.2. The proposed platform is composed of three components: VLC transmitter, a laboratory chamber to emulate the underground mine conditions, and the VLC receiver.

The transmitter is composed of an Arbitrary Waveform Generator (AWG) Tektronix, which generates the modulated waveform to be used for the system. This makes the test bed completely flexible for different modulation schemes, bandwidths, and data rates, among others. The bias tee combines the modulated waveform with the DC current bias. A commercial LED light is used to transmit the signal. During the test bed, two AWGs will be used to finally have four VLC sources. In order to emulate the atmospheric conditions of the underground mine, an atmospheric chamber must be built. In this chamber, traditional mine conditions such as extreme heat, objects (shadowing), dust in suspension (scattering), and irregular walls, among others will be emulated. The chamber is made by a hermetic acrylic square coupled with heater fans, a glycerine machine, optical dust sensors, and temperature sensors as shown in Figure 6.2. To demodulate the received signal, the IM/DD scheme finally

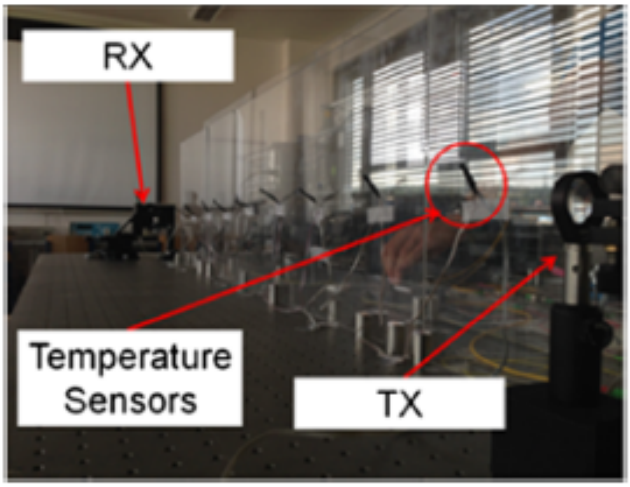

Figure 6.2: Proposed experimental atmospheric chamber.

uses a PD at the receiver side to sense the changes in the optical power. The received signal is digitalized by using an oscilloscope, which sends the data to the notebook. The VLC signal is processed offline by exploiting Matlab or other programming platforms.

Under this experimental test-bed methodology, we will be able to validate the results obtained in this work along with the relevant metrics obtained from the UM-VLC system and channel model.

Theoretical Validations and Derived Developments

A deeper statistical development (second-order statistics and probability distributions) of the hemispherical distribution of dust particles, the behavior of dust particles when interacting with light, and the component of the UM-VLC scattering channel should be considered as future work. In addition to the BER metric analyzed in this thesis, the SER will be considered in order to present solutions based on convolutional coding, reducing the effect of isolated errors. On the other hand, electronic simulations of the elements of the reception stage will be implemented to evaluate various configurations, induced noise levels, and bandwidth, among others. Finally, it will be interesting to evaluate the possibility that this work is a basis for new application environments of VLC systems and their consequent theoretical and experimental developments, such as greenhouse environments, and industrial environments, among others. These future works will allow us to compare the results with the solutions already proposed in this thesis.

Bibliography

[1] M. T. Diogo, "European legal framework related to underground mining and tunnelling concerning commission directive (eu) 2017/164, 31 january establishing a fourth list of indicative occupational exposure limit values," *International Journal of Mining Science and Technology*, 2020.

[2] A. Ranjan, Y. Zhao, H. B. Sahu, and P. Misra, "Opportunities and challenges in health sensing for extreme industrial environment: Perspectives from underground mines," *IEEE Access*, vol. 7, pp. 139181–139195, 2019.

[3] S. Yarkan, S. Guzelgoz, H. Arslan, and R. R. Murphy, "Underground mine communications: A survey," *IEEE Communications Surveys Tutorials*, vol. 11, no. 3, pp. 125–142, 2009.

[4] P. H. Pathak, X. Feng, P. Hu, and P. Mohapatra, "Visible light communication, networking, and sensing: A survey, potential and challenges," *IEEE Communications Surveys & Tutorials*, vol. 17, no. 4, pp. 2047–2077, 2015.

[5] X. Qiu, J. Wei, J. Li, C. Li, and C. Wei, "A novel identification system based on visible light communication," in *22nd Wireless and Optical Communication Conference*, IEEE, may 2013.

[6] Y. Zhai and S. Zhang, "Visible light communication channel models and simulation of coal workface energy coupling," *Mathematical Problems in Engineering*, vol. 2015, pp. 1–10, 2015.

[7] J. Wang, A. Al-Kinani, W. Zhang, C.-X. Wang, and L. Zhou, "A general channel model for visible light communications in underground mines," *China Communications*, vol. 15, pp. 95–105, sep 2018.

[8] A. Al-Kinani, C. Wang, L. Zhou, and W. Zhang, "Optical wireless communication channel measurements and models," *IEEE Communications Surveys Tutorials*, vol. 20, no. 3, pp. 1939–1962, 2018.

[9] J. Wang, A. Al-Kinani, W. Zhang, and C.-X. Wang, "A new VLC channel model for underground mining environments," in *13th International Wireless Communications and Mobile Computing Conference (IWCMC)*, IEEE, jun 2017.

[10] P. P. Játiva, C. A. Azurdia-Meza, I. Sánchez, F. Seguel, D. Zabala-Blanco, A. D. Firoozabadi, C. A. Gutiérrez, and I. Soto, "A vlc channel model for underground mining environments with scattering and shadowing," *IEEE Access*, vol. 8, pp. 185445–185464, 2020.

[11] P. Palacios Játiva, C. A. Azurdia-Meza, I. Sánchez, D. Zabala-Blanco, A. Dehghan Firoozabadi, I. Soto, and F. Seguel, "An enhanced vlc channel model for underground mining environments considering a 3d dust particle distribution model," *Sensors*, vol. 22, no. 7, p. 2483, 2022.

[12] P. Palacios Játiva, M. Román Cañizares, C. A. Azurdia-Meza, D. Zabala-Blanco, A. Dehghan Firoozabadi, F. Seguel, S. Montejo-Sánchez, and I. Soto, "Interference mitigation for visible light communications in underground mines using angle diversity receivers," *Sensors*, vol. 20, no. 2, p. 367, 2020.

[13] M. Improvement, "New emergency response act of 2006 (miner act), pub," *L. No. 108-236 (S 2803)*, 2006.

[14] U. I. Minhas, I. H. Naqvi, S. Qaisar, K. Ali, S. Shahid, and M. A. Aslam, "A WSN for monitoring and event reporting in underground mine environments," *IEEE Systems Journal*, vol. 12, pp. 485–496, mar 2018.

[15] Z. Ghassemlooy, *Optical wireless communications : system and channel modelling with MATLAB*. Boca Raton, FL: CRC Press, 2018.

[16] P. Palacios, C. A. Azurdia-Meza, M. Román-Cañizares, S. Céspedes, and S. Montejo-Sánchez, "Performance enhancement of vlc-based systems using diversity combining schemes in the receiver," in *IEEE 11th Latin-American Conference on Communications (LATINCOM)*, IEEE, nov 2019.

[17] W. Picking, "Primer piloto 5g en la minería chilena." https://webpicking.com/primer-piloto-5g-en-la-mineria-chilena/, 2020.

[18] R. Minero, "Codelco implementó piloto para incorporar tecnología 5g en radomiro tomic." https://www.reporteminero.cl/noticia/noticias/2020/12/codelco-implemento-piloto-para-incorporar-tecnologia-5g-en-radomiro-tomic, 2020.

[19] M. Magazine, "Sweden's first 5g network for industry goes live." https://www.miningmagazine.com/communications/news/1358410/swedens-first-5g-network-for-industry-goes-live, 2019.

[20] M. Weekly, "Full 5g adoption in mining still years away." https://www.miningweekly.com/article/full-5g-adoption-in-mining-still-years-away-2020-08-24/rep$_{\text{i}}$d : 3650, 2020.

[21] M. Obeed, A. M. Salhab, M. Alouini, and S. A. Zummo, "On optimizing vlc networks for downlink multi-user transmission: A survey," *IEEE Communications Surveys Tutorials*, vol. 21, no. 3, pp. 2947–2976, 2019.

[22] A. D. Firoozabadi, C. Azurdia-Meza, I. Soto, F. Seguel, N. Krommenacker, D. Iturralde, P. Charpentier, and D. Zabala-Blanco, "A novel frequency domain visible light communication (VLC) three-dimensional trilateration system for localization in underground mining," *Applied Sciences*, vol. 9, p. 1488, apr 2019.

[23] D. Iturralde, C. Azurdia-Meza, N. Krommenacker, I. Soto, Z. Ghassemlooy, and N. Becerra, "A new location system for an underground mining environment using visible light communications," in *2014 9th International Symposium on Communication Systems, Networks & Digital Sign (CSNDSP)*, IEEE, jul 2014.

[24] D. Iturralde, F. Seguel, I. Soto, C. Azurdia, and S. Khan, "A new VLC system for localization in underground mining tunnels," *IEEE Latin America Transactions*, vol. 15, pp. 581–587, apr 2017.

[25] Z. Chen, D. Tsonev, and H. Haas, "Improving SINR in indoor cellular visible light communication networks," in *IEEE International Conference on Communications (ICC)*, IEEE, jun 2014.

[26] C. Chen, W.-D. Zhong, H. Yang, S. Zhang, and P. Du, "Reduction of SINR fluctuation in indoor multi-cell VLC systems using optimized angle diversity receiver," *Journal of Lightwave Technology*, vol. 36, pp. 3603–3610, sep 2018.

[27] C. Chen, D. Tsonev, and H. Haas, "Joint transmission in indoor visible light communication downlink cellular networks," in *IEEE Globecom Workshops (GC Wkshps)*, IEEE, dec 2013.

[28] C. Chen, S. Videv, D. Tsonev, and H. Haas, "Fractional frequency reuse in DCO-OFDM-based optical attocell networks," *Journal of Lightwave Technology*, vol. 33, pp. 3986–4000, oct 2015.

[29] A. Nuwanpriya, S.-W. Ho, and C. S. Chen, "Indoor MIMO visible light communications: Novel angle diversity receivers for mobile users," *IEEE Journal on Selected Areas in Communications*, vol. 33, pp. 1780–1792, sep 2015.

[30] Z. Chen, D. A. Basnayaka, X. Wu, and H. Haas, "Interference mitigation for indoor optical attocell networks using an angle diversity receiver," *Journal of Lightwave Technology*, vol. 36, pp. 3866–3881, sep 2018.

[31] N. Saha, R. K. Mondal, and Y. M. Jang, "Receiver performance improvement utilizing diversity in MIMO VLC," in *International Conference on ICT Convergence (ICTC)*, IEEE, oct 2013.

[32] Z. Chen, N. Serafimovski, and H. Haas, "Angle diversity for an indoor cellular visible light communication system," in *IEEE 79th Vehicular Technology Conference (VTC Spring)*, IEEE, may 2014.

[33] J. Wang, A. Al-Kinani, J. Sun, W. Zhang, and C.-X. Wang, "A path loss channel model for visible light communications in underground mines," in *IEEE/CIC International Conference on Communications in China (ICCC)*, IEEE, oct 2017.

[34] J. Wang, A. Al-Kinani, W. Zhang, and C. Wang, "A new vlc channel model for underground mining environments," in *2017 13th International Wireless Communications and Mobile Computing Conference (IWCMC)*, pp. 2134–2139, 2017.

[35] M. M. Cespedes and A. G. Armada, "Characterization of the visible light communications during the construction of tunnels," in *2019 16th International Symposium on Wireless Communication Systems (ISWCS)*, IEEE, aug 2019.

[36] S. Riurean, O. Stoicuta, M. Leba, A. Ionica, and Á. Rocha, "Underground channel model for visible light wireless communication based on neural networks," in *World Conference on Information Systems and Technologies*, pp. 293–305, Springer, 2020.

[37] A. Borhani and M. Pätzold, "Time-of-arrival, angle-of-arrival, and angle-of-departure statistics of a novel simplistic disk channel model," in *2011 5th International Conference on Signal Processing and Communication Systems (ICSPCS)*, pp. 1–7, 2011.

[38] A. Borhani and M. Patzold, "A unified disk scattering model and its angle-of-departure and time-of-arrival statistics," *IEEE Transactions on Vehicular Technology*, vol. 62, no. 2, pp. 473–485, 2013.

[39] Y. Sun, C. Gong, Z. Xu, and Y. Zhan, "Link gain and pulse width broadening evaluation of non-line-of-sight optical wireless scattering communication over broad spectra," *IEEE Photonics Journal*, vol. 9, no. 3, pp. 1–12, 2017.

[40] W. Liu, D. Zou, and Z. Xu, "Modeling of optical wireless scattering communication channels over broad spectra," *JOSA A*, vol. 32, no. 3, pp. 486–490, 2015.

[41] A. Al-Kinani, C. Wang, H. Haas, and Y. Yang, "Characterization and modeling of visible light communication channels," in *2016 IEEE 83rd Vehicular Technology Conference (VTC Spring)*, pp. 1–5, 2016.

[42] A. Al-Kinani, C. Wang, H. Haas, and Y. Yang, "A geometry-based multiple bounce model for visible light communication channels," in *2016 International Wireless Communications and Mobile Computing Conference (IWCMC)*, pp. 31–37, 2016.

[43] C. Chen, W.-D. Zhong, D. Wu, and Z. Ghassemlooy, "Wide-FOV and high-gain imaging angle diversity receiver for indoor SDM-VLC systems," *IEEE Photonics Technology Letters*, vol. 28, pp. 2078–2081, oct 2016.

[44] Z. Zeng, M. D. Soltani, M. Safari, and H. Haas, "Angle diversity receiver in LiFi cellular networks," in *IEEE International Conference on Communications (ICC)*, IEEE, may 2019.

[45] B. Zhuang, C. Li, and Z. Xu, "Enhanced performance of spatial modulation with angular diversity receiver for indoor visible light communication," in *IEEE/CIC International Conference on Communications in China (ICCC)*, IEEE, jul 2016.

[46] P. P. Játiva, C. A. Azurdia-Meza, D. Zabala-Blanco, C. A. Gutiérrez, I. Sánchez, F. R. Castillo-Soria, and F. Seguel, "Bit error probability of vlc systems in underground

mining channels with imperfect csi," *AEU - International Journal of Electronics and Communications*, vol. 145, p. 154101, 2022.

[47] P. Palacios Játiva, I. Sánchez, I. Soto, C. A. Azurdia-Meza, D. Zabala-Blanco, M. Ijaz, A. Dehghan Firoozabadi, and D. Plets, "A novel and adaptive angle diversity-based receiver for 6g underground mining vlc systems," *Entropy*, vol. 24, no. 11, p. 1507, 2022.

[48] P. P. Játiva, C. A. Azurdia-Meza, M. R. Cañizares, D. Zabala-Blanco, and I. Soto, "Ber performance of ofdm-based visible light communication systems," in *2019 IEEE CHILEAN conference on electrical, electronics engineering, information and communication technologies (CHILECON)*, pp. 1–6, IEEE, 2019.

[49] P. P. Játiva, C. A. Azurdia-Meza, M. R. Canizares, S. Céspedes, and S. Montejo-Sánchez, "Performance enhancement of vlc-based systems using diversity combining schemes in the receiver," in *2019 IEEE Latin-American Conference on Communications (LATINCOM)*, pp. 1–6, IEEE, 2019.

[50] P. P. Jativa, C. A. Azurdia-Meza, M. R. Canizares, D. Zabala-Blanco, and S. Montejo-Sanchez, "Performance analysis of ofdm-based vlc schemes in nlos channels," in *2020 South American Colloquium on Visible Light Communications (SACVC)*, pp. 1–6, IEEE, 2020.

[51] P. Palacios Játiva, C. A. Azurdia-Meza, M. Román Cañizares, D. Zabala-Blanco, and C. Saavedra, "Propagation features of visible light communication in underground mining environments," in *International Conference on Applied Technologies*, pp. 82–93, Springer, 2019.

[52] P. P. Játiva, C. Azurdia, M. Román, D. Zabala-Blanco, F. Seguel, and I. Soto, "Empirical path loss distribution for visible light communications in underground mines," in *2020 12th International Symposium on Communication Systems, Networks and Digital Signal Processing (CSNDSP)*, pp. 1–6, 2020.

[53] P. P. Játiva, C. A. Azurdia-Meza, M. R. Cañizares, I. Sánchez, and D. Iturralde, "On the performance of visible light communications in underground mines," in *2020 IEEE Latin-American Conference on Communications (LATINCOM)*, pp. 1–6, IEEE, 2020.

[54] P. P. Játiva, F. Seguel, and P. Adasme, "Evaluation of intelligent reflecting surfaces for diffuse visible light communications link," in *2020 IEEE Latin-American Conference on Communications (LATINCOM)*, pp. 1–5, IEEE, 2020.

[55] P. P. Játiva, C. A. Azurdia-Meza, M. R. Cañizares, I. Sánchez, and A. D. Firoozabadi, "Bit error rate analysis for ofdm schemes applied to underground mining vlc systems," in *2021 Third South American Colloquium on Visible Light Communications (SACVLC)*, pp. 1–6, IEEE, 2021.

[56] P. P. Játiva, R. Becerra, C. A. Azurdia-Meza, D. Zabala-Blanco, I. Soto, and M. R. Cañizares, "Extreme learning machine based channel estimator and equalizer for un-

derground mining vlc systems," in *2021 IEEE Latin-American Conference on Communications (LATINCOM)*, pp. 1–6, IEEE, 2021.

[57] P. P. Játiva, C. A. Azurdia-Meza, M. R. Cañizares, I. Sánchez, F. Seguel, D. Zabala-Blanco, and D. F. Carrera, "Performance analysis of ieee 802.15. 7-based visible light communication systems in underground mine environments," *Photonic Network Communications*, vol. 43, no. 1, pp. 23–33, 2022.

[58] P. P. Játiva, C. A. Azurdia-Meza, D. Zabala-Blanco, I. Soto, M. Ijaz, D. F. Carrera, and S. Ekpo, "On the performance of angular diversity receivers in underground mining vlc systems," in *2022 13th International Symposium on Communication Systems, Networks and Digital Signal Processing (CSNDSP)*, pp. 795–800, IEEE, 2022.

[59] M. Improvement, "New emergency response act of 2006 (miner act), pub," *L. No. 108-236 (S 2803)*, 2006.

[60] T. Novak, D. P. Snyder, and J. L. Kohler, "Postaccident mine communications and tracking systems," *IEEE Transactions on Industry Applications*, vol. 46, no. 2, pp. 712–719, 2010.

[61] A. F. G. Gonçalves Ferreira, D. M. A. Fernandes, A. P. Catarino, and J. L. Monteiro, "Localization and positioning systems for emergency responders: A survey," *IEEE Communications Surveys Tutorials*, vol. 19, no. 4, pp. 2836–2870, 2017.

[62] P. Palacios Játiva, C. A. Azurdia-Meza, M. Román Cañizares, D. Zabala-Blanco, and C. Saavedra, "Propagation features of visible light communication in underground mining environments," in *Applied Technologies*, pp. 82–93, Springer International Publishing, 2020.

[63] J. Wang, A. Al-Kinani, W. Zhang, C. Wang, and L. Zhou, "A general channel model for visible light communications in underground mines," *China Communications*, vol. 15, no. 9, pp. 95–105, 2018.

[64] P. Palacios, C. A. Azurdia-Meza, M. Román-Cañizares, S. Céspedes, and S. Montejo-Sánchez, "Performance enhancement of vlc-based systems using diversity combining schemes in the receiver," in *IEEE 11th Latin-American Conference on Communications (LATINCOM)*, IEEE, nov 2019.

[65] Z. Ghassemlooy, *Optical wireless communications: System and channel modelling with MATLAB*. Boca Raton, FL: CRC Press, 2018.

[66] P. P. Játiva, C. A. Azurdia-Meza, M. R. Cañizares, S. Céspedes, and S. Montejo-Sánchez, "Performance enhancement of vlc-based systems using diversity combining schemes in the receiver," in *2019 IEEE Latin-American Conference on Communications (LATINCOM)*, pp. 1–6, 2019.

[67] Z. Ghassemlooy, *Optical wireless communications : system and channel modelling with MATLAB*. Boca Raton, FL: CRC Press, 2018.

[68] J. Wang, A. Al-Kinani, W. Zhang, C. Wang, and L. Zhou, "A general channel model for visible light communications in underground mines," *China Communications*, vol. 15, no. 9, pp. 95–105, 2018.

[69] G. Wu and J. Zhang, "Demonstration of a visible light communication system for underground mining applications," *DEStech Transactions on Engineering and Technology Research*, no. iect, 2016.

[70] F. Seguel, *Robust localization system using Visible Light Communication technology for underground mines.* Theses, Université de Lorraine ; Universidad de Santiago de Chile, Mar. 2020.

[71] D. Iturralde, C. Azurdia-Meza, N. Krommenacker, I. Soto, Z. Ghassemlooy, and N. Becerra, "A new location system for an underground mining environment using visible light communications," in *2014 9th International Symposium on Communication Systems, Networks Digital Sign (CSNDSP)*, pp. 1165–1169, 2014.

[72] D. Iturralde, F. Seguel, I. Soto, C. Azurdia, and S. Khan, "A new vlc system for localization in underground mining tunnels," *IEEE Latin America Transactions*, vol. 15, no. 4, pp. 581–587, 2017.

[73] A. Dehghan Firoozabadi, C. Azurdia-Meza, I. Soto, F. Seguel, N. Krommenacker, D. Iturralde, P. Charpentier, and D. Zabala-Blanco, "A novel frequency domain visible light communication (vlc) three-dimensional trilateration system for localization in underground mining," *Applied Sciences*, vol. 9, no. 7, p. 1488, 2019.

[74] I. Soto, R. Nilson Rodrigues, G. Massuyama, F. Seguel, P. Palacios Játiva, C. A. Azurdia-Meza, and N. Krommenacker, "A hybrid vlc-rf portable phasor measurement unit for deep tunnels," *Sensors*, vol. 20, no. 3, p. 790, 2020.

[75] J. Wang, A. Al-Kinani, J. Sun, W. Zhang, and C. Wang, "A path loss channel model for visible light communications in underground mines," in *2017 IEEE/CIC International Conference on Communications in China (ICCC)*, pp. 1–5, 2017.

[76] M. M. Céspedes and A. García Armada, "Characterization of the visible light communications during the construction of tunnels," in *2019 16th International Symposium on Wireless Communication Systems (ISWCS)*, pp. 356–360, 2019.

[77] Y. Zhai and S. Zhang, "Visible light communication channel models and simulation of coal workface energy coupling," *Mathematical Problems in Engineering*, vol. 2015, 2015.

[78] T. Komine and M. Nakagawa, "A study of shadowing on indoor visible-light wireless communication utilizing plural white led lightings," in *1st International Symposium onWireless Communication Systems, 2004.*, pp. 36–40, 2004.

[79] Y. Xiang, M. Zhang, M. Kavehrad, M. S. Chowdhury, M. Liu, J. Wu, and X. Tang, "Human shadowing effect on indoor visible light communications channel characteristics," *Optical Engineering*, vol. 53, no. 8, p. 086113, 2014.

[80] H. Farahneh, C. Mekhiel, A. Khalifeh, W. Farjow, and X. Fernando, "Shadowing effects on visible light communication channels," in *2016 IEEE Canadian Conference on Electrical and Computer Engineering (CCECE)*, pp. 1–5, 2016.

[81] Y. Wang, X. Wu, and H. Haas, "Load balancing game with shadowing effect for indoor hybrid lifi/rf networks," *IEEE Transactions on Wireless Communications*, vol. 16, no. 4, pp. 2366–2378, 2017.

[82] Z. Dong, T. Shang, Y. Gao, and Q. Li, "Study on vlc channel modeling under random shadowing," *IEEE Photonics Journal*, vol. 9, no. 6, pp. 1–16, 2017.

[83] S. Shen, S. Li, and H. Steendam, "Simultaneous position and orientation estimation for visible light systems with multiple leds and multiple pds," *IEEE Journal on Selected Areas in Communications*, pp. 1–1, 2020.

[84] D. Plets, S. Bastiaens, L. Martens, and W. Joseph, "An analysis of the impact of led tilt on visible light positioning accuracy," *Electronics*, vol. 8, no. 4, p. 389, 2019.

[85] D. Kim, J. K. Park, and J. T. Kim, "Three-dimensional vlc positioning system model and method considering receiver tilt," *IEEE Access*, vol. 7, pp. 132205–132216, 2019.

[86] M. A. Arfaoui, M. D. Soltani, I. Tavakkolnia, A. Ghrayeb, C. Assi, M. Safari, and H. Haas, "Measurements-based channel models for indoor lifi systems," *arXiv preprint arXiv:2001.09596*, 2020.

[87] Y. S. Eroğlu, Y. Yapıcı, and Güvenç, "Impact of random receiver orientation on visible light communications channel," *IEEE Transactions on Communications*, vol. 67, no. 2, pp. 1313–1325, 2019.

[88] M. D. Soltani, A. A. Purwita, Z. Zeng, H. Haas, and M. Safari, "Modeling the random orientation of mobile devices: Measurement, analysis and lifi use case," *IEEE Transactions on Communications*, vol. 67, no. 3, pp. 2157–2172, 2019.

[89] H. Ding, *Modeling and characterization of ultraviolet scattering communication channels*. PhD thesis, UC Riverside, 2011.

[90] S. S. Muhammad, "Delay profiles for indoor diffused visible light communication," in *2015 13th International Conference on Telecommunications (ConTEL)*, pp. 1–5, 2015.

[91] J. Kahn and J. Barry, "Wireless infrared communications," *Proceedings of the IEEE*, vol. 85, no. 2, pp. 265–298, 1997.

[92] C. Chen, D. A. Basnayaka, and H. Haas, "Downlink performance of optical attocell networks," *Journal of Lightwave Technology*, vol. 34, pp. 137–156, jan 2016.

[93] R. V. Priyan, S. Dinesh, J. Ilanthendral, and B. Ramya, "Communication system for underground mines using li-fi 5g technology," *IJLTEMAS*, vol. III, no. IX, pp. 80–85, 2014.

[94] H. Farahneh, F. Hussain, and X. Fernando, "A new alarming system for an underground mining environment using visible light communications," in *IEEE Canada International Humanitarian Technology Conference (IHTC)*, IEEE, jul 2017.

[95] F. Alsalami, Z. Ahmad, S. Zvanovec, P. Haigh, O. Haas, and S. Rajbhandari, "Indoor intruder tracking using visible light communications," *Sensors*, vol. 19, p. 4578, oct 2019.

[96] J. Wang, A. Al-Kinani, W. Zhang, C.-X. Wang, and L. Zhou, "A general channel model for visible light communications in underground mines," *China Communications*, vol. 15, pp. 95–105, sep 2018.

[97] H. Yang, C. Chen, and W.-D. Zhong, "Cognitive multi-cell visible light communication with hybrid underlay/overlay resource allocation," *IEEE Photonics Technology Letters*, vol. 30, pp. 1135–1138, jun 2018.

[98] "IEEE Standard for Local and metropolitan area networks–Part 15.7: Short-Range Optical Wireless Communications," *IEEE Std 802.15.7-2018*, pp. 1–670, Apr. 2019.

[99] Y. Sun, C. Gong, Z. Xu, and Y. Zhan, "Link gain and pulse width broadening evaluation of non-line-of-sight optical wireless scattering communication over broad spectra," *IEEE Photonics Journal*, vol. 9, no. 3, pp. 1–12, 2017.

[100] W. Liu, D. Zou, and Z. Xu, "Modeling of optical wireless scattering communication channels over broad spectra," *JOSA A*, vol. 32, no. 3, pp. 486–490, 2015.

[101] A. Al-Kinani, C. Wang, H. Haas, and Y. Yang, "A geometry-based multiple bounce model for visible light communication channels," in *2016 International Wireless Communications and Mobile Computing Conference (IWCMC)*, pp. 31–37, 2016.

[102] A. Al-Kinani, C.-X. Wang, Q. Zhu, Y. Fu, E.-H. M. Aggoune, A. Talib, and N. A. Al-Hasaani, "A 3d non-stationary gbsm for vehicular visible light communication miso channels," *IEEE Access*, vol. 8, pp. 140333–140347, 2020.

[103] F. Javaid, A. Wang, M. U. Sana, A. Husain, and I. Ashraf, "Characteristic study of visible light communication and influence of coal dust particles in underground coal mines," *Electronics*, vol. 10, no. 8, p. 883, 2021.

[104] P. P. Játiva, R. Becerra, C. A. Azurdia-Meza, D. Zabala-Blanco, I. Soto, and M. R. Cañizares, "Extreme learning machine based channel estimator and equalizer for underground mining vlc systems," in *2021 IEEE Latin-American Conference on Communications (LATINCOM)*, pp. 1–6, 2021.

[105] P. P. Játiva, C. A. Azurdia-Meza, D. Zabala-Blanco, C. A. Gutiérrez, I. Sánchez, F. R. Castillo-Soria, and F. Seguel, "Bit error probability of vlc systems in underground mining channels with imperfect csi," *AEU-International Journal of Electronics and Communications*, p. 154101, 2022.

[106] C. Xu, H. Zhang, and J. Cheng, "Effects of haze particles and fog droplets on nlos

ultraviolet communication channels," *Optics express*, vol. 23, no. 18, pp. 23259–23269, 2015.

[107] Y. Chen, C. W. Sung, S.-W. Ho, and W. S. Wong, "BER analysis for interfering visible light communication systems," in *10th International Symposium on Communication Systems, Networks and Digital Signal Processing (CSNDSP)*, IEEE, jul 2016.

[108] A. Ranjan, Y. Zhao, H. B. Sahu, and P. Misra, "Opportunities and challenges in health sensing for extreme industrial environment: Perspectives from underground mines," *IEEE Access*, vol. 7, pp. 139181–139195, 2019.

[109] S. Yarkan, S. Guzelgoz, H. Arslan, and R. R. Murphy, "Underground mine communications: A survey," *IEEE Communications Surveys Tutorials*, vol. 11, no. 3, pp. 125–142, 2009.

[110] U. I. Minhas, I. H. Naqvi, S. Qaisar, K. Ali, S. Shahid, and M. A. Aslam, "A wsn for monitoring and event reporting in underground mine environments," *IEEE Systems Journal*, vol. 12, no. 1, pp. 485–496, 2018.

[111] J. Shi, W. Niu, Y. Ha, Z. Xu, Z. Li, S. Yu, and N. Chi, "Ai-enabled intelligent visible light communications: Challenges, progress, and future," in *Photonics*, vol. 9, p. 529, Multidisciplinary Digital Publishing Institute, 2022.

[112] F. Miramirkhani and M. Uysal, "Channel modelling for indoor visible light communications," *Philosophical Transactions of the Royal Society A*, vol. 378, no. 2169, p. 20190187, 2020.

[113] M. Mardonova and Y. Choi, "Review of wearable device technology and its applications to the mining industry," *Energies*, vol. 11, p. 547, mar 2018.

[114] R. Mikesell, *The global copper industry : problems and prospects*. Abingdon, Oxon: Routledge, 2018.

[115] M. A. Dawood, S. S. Saleh, E.-S. A. El-Badawy, and M. H. Aly, "A comparative analysis of localization algorithms for visible light communication," *Optical and Quantum Electronics*, vol. 53, no. 2, pp. 1–25, 2021.

[116] L. Bai, Y. Yang, Z. Zhang, C. Feng, C. Guo, and J. Cheng, "A high-coverage camera assisted received signal strength ratio algorithm for indoor visible light positioning," *IEEE Transactions on Wireless Communications*, vol. 20, no. 9, pp. 5730–5743, 2021.

ANNEXES A

Annex A: Publications

Journal (WoS):

- Becerra, R., Azurdia-Meza, C. A., **Palacios Játiva, P.**, Soto, I., Sandoval, J., Ijaz, M., Carrera, D. F, "A Wavelength-Dependent Visible Light Communication Channel Model for Underground Environments and Its Performance Using a Color-Shift Keying Modulation Scheme". *Electronics*, vol. 12, no. 3, pp. 577, 2023.
- **Palacios Játiva, P.**; Sánchez, Iván; Soto, Ismael; Azurdia-Meza, Cesar A; Zabala-Blanco, David; Ijaz, Muhammad; and Dehghan Firoozabadi, Ali; and Plets, David, "A Novel and Adaptive Angle Diversity-Based Receiver for 6G Underground Mining VLC Systems," *Entropy*, vol. 24, no. 11, pp. 1507, 2022.
- **Palacios Játiva, P.**; Azurdia-Meza, Cesar A.; Sánchez, Iván; Zabala-Blanco, David; Dehghan Firoozabadi, Ali; Soto, Ismael; and Seguel, Fabian, "An Enhanced VLC Channel Model for Underground Mining Environments Considering a 3D Dust Particle Distribution Model," *Sensors*, vol. 20, no. 7, pp. 2483, 2022.
- **Palacios Játiva, P.**; Azurdia-Meza, C. A.; Zabala-Blanco, D.; Gutiérrez, C. A.; Sánchez, I.; Castillo-Soria, F. R.; and Seguel, F., "Bit error probability of VLC systems in underground mining channels with imperfect CSI," *AEU-International Journal of Electronics and Communications*, vol. 145, pp. 154101, 2022.
- **Palacios Játiva, P.**; Azurdia-Meza, Cesar A.; Cañizares, Milton Román; Sánchez, Iván; Seguel, Fabian; Zabala-Blanco, David; and Carrera, Diego Fernando, "Performance analysis of IEEE 802.15. 7-based visible light communication systems in underground mine environments," *Photonic Network Communications*, vol. 43, no. 1, pp. 23-33, 2022.
- Seguel, F., **Palacios Játiva, P.**, Azurdia-Meza, C. A., Krommenacker, N., Charpentier, P., Soto, I., "Underground Mine Positioning: A Review," *IEEE Sensors Journal*, 2021.
- **Palacios Játiva, P.**, C. A. Azurdia-Meza, I. Sánchez, F. Seguel, D. Zabala-Blanco, A. D. Firoozabadi, C. A. Gutiérrez, and I. Soto, "A VLC Channel Model for Underground Mining Environments with Scattering and Shadowing," *IEEE Access*, vol. 8, pp. 85445–185464, 2020.
- **Palacios Játiva, P.**; Román Cañizares, M.; Azurdia-Meza, C.A.; Zabala-Blanco, D.;

Dehghan Firoozabadi, A.; Seguel, F.; Montejo-Sánchez, S.; Soto, I., "Interference Mitigation for Visible Light Communications in Underground Mines Using Angle Diversity Receivers," *Sensors*, vol. 20, no. 2, pp. 367, 2020.

- I. Soto, R. Nilson Rodrigues, G. Massuyama, F. Seguel, **Palacios Játiva, P.**, C. A. Azurdia-Meza, and N. Krommenacker, "A Hybrid VLC-RF Portable Phasor Measurement Unit for Deep Tunnels," *Sensors*, vol. 20, no. 7, pp. 1488, 2020.

Conference:

- Fredes, Camilo and **Palacios Játiva, P.** and Meza, Cesar Azurdia and Soto, Ismael, "Design and Evaluation of an Experimental Visible Light Communications Platform," in *IEEE ICA-ACCA 2022*, Talca, Chile, 2022.
- Solis, Julian and **Palacios Játiva, P.** and Meza, Cesar A Azurdia and Zabala-Blanco, David and Soto, Ismael and Ijaz, Muhammad, "A General MIMO VLC Channel Model for Underground Mining Environments," in *IEEE Latin-American Conference on Communications)*, Río de Janeiro, Brasil, 2022.
- Javiero, Vinson and Ijaz, Muhammad and Ekpo, Sunday and Adebisi, Bamidele and Chen, Chen and **Palacios Játiva, P.** and Azurdia, Cesar and Soto, Ismael and Khalighi, Mohammad-Ali, "Investigation of Indoor Atmospheric Attenuation in Visible Light Positioning for Industrial Applications ," in *2022 13th International Symposium on Communication Systems, Networks and Digital Signal Processing (CSNDSP)*, Porto, Portugal, 2022.
- **Palacios Játiva, P.** and Becerra, Raimundo and Azurdia-Meza, Cesar A and Zabala-Blanco, David and Soto, Ismael and Cañizares, Milton Román, "Extreme Learning Machine Based Channel Estimator and Equalizer for Underground Mining VLC Systems," in *2021 IEEE Latin-American Conference on Communications (LATINCOM)*, Santo Domingo, República Dominicana, 2022.
- **Palacios Játiva, P.** and Azurdia-Meza, Cesar A and Zabala-Blanco, David and Soto, Ismael and Ijaz, Muhammad and Carrera, Diego Fernando and Ekpo, Sunday, "On the Performance of Angular Diversity Receivers in Underground Mining VLC Systems," in *2022 13th International Symposium on Communication Systems, Networks and Digital Signal Processing (CSNDSP)*, Porto, Portugal, 2022.
- **Palacios Játiva, P.** and Azurdia, Cesar and Román, Milton and Zabala-Blanco, David and Seguel, Fabian and Soto, Ismael, "Empirical Path Loss Distribution for Visible Light Communications in Underground Mines," in *2020 12th International Symposium on Communication Systems, Networks and Digital Signal Processing (CSNDSP)*, Funchal, Oporto, Portugal, 2020.
- **Palacios Játiva, P.** and Azurdia-Meza, Cesar A and Cañizares, Milton Román and Sánchez, Iván and Iturralde, Daniel, "On the performance of visible light communications in underground mines," in *2020 IEEE Latin-American Conference on Communications (LATINCOM)*, Online, 2020.
- **Palacios Játiva, P.** and Seguel, Fabian and Adasme, Pablo, "Evaluation of intelligent reflecting surfaces for diffuse visible light communications link," in *2020 IEEE Latin-American Conference on Communications (LATINCOM)*, Online, 2020.
- **Palacios Játiva, P.** and Azurdia-Meza, Cesar A and Cañizares, Milton Román and Zabala-Blanco, David and Soto, Ismael, "BER performance of OFDM-based visible light

communication systems," in *2019 IEEE CHILEAN conference on electrical, electronics engineering, information and communication technologies (CHILECON)*, Santiago, Chile, 2019.

- **Palacios Játiva, P.** and Azurdia-Meza, Cesar A and Canizares, Milton Roman and Zabala-Blanco, David and Montejo-Sanchez, Samuel, "Performance analysis of OFDM-based VLC schemes in NLOS channels," in *2020 South American Colloquium on Visible Light Communications (SACVC)*, Santiago, Chile, 2020.
- **Palacios Játiva, P.** and Azurdia-Meza, Cesar A and Román Cañizares, Milton and Zabala-Blanco, David and Saavedra, Carlos, "Propagation features of visible light communication in underground mining environments," in *International Conference on Applied Technologies*, Quito, Ecuador, 2019.

ANNEXES B

Annex B: Scripts and Codes

Base Programming Codes:

```
%posici n Ti
x_i=3;
y_i=0.5;
z_i=4.5;

%posici n Rj1
x_j=3;
y_j=1;
z_j=1.8;

%posici n del Rj2
x_j2=3;
y_j2=1.5;
z_j2=1.8;

%posici n del Rj3
x_j3=4;
y_j3=2;
z_j3=1.8;

%posici n del Rj4
x_j4=2.2;
y_j4=2.5;
z_j4=1.8;

%posici n del Rj5
x_j5=1;
y_j5=2.5;
z_j5=1.6;

%posici n del  rea  reflectiva (pared)

% first reflection_point
x_w1=2;
y_w1=2;
z_w1=3;
% second reflection_point
x_w2=1.5;
y_w2=2.3;
z_w2=4.0;
% third reflection_point
x_w=5;
y_w=2.9;
z_w=3.5;

%position of scatering particle
x_s=4;
```

```
y_s=4.5;
z_s=2.5;
                        %par metros de la simulaci n%

Aw=1  ;                                     % rea  reflectiva de la pared
pw=0.8 ;                                    %coeficiente de reflexi n del  rea  reflectiva
ang_rad = 60;                               %semi- ngulo  de mitad de potencia del LED
m= -log(2)/log(abs(cos(ang_rad*pi/180)));   %n mero Lambertiano
Ap=0.0001;                                  % rea  f sica del receptor (1 cm^2)
eta=1.5;                                    %indice de refracci n del PD
fov =  70;                                  %field of view

                %par metros de los  ngulos  de inclinaci n y rotaci n%

beta_i=45;                                  % ngulo  de inclinaci n del LED con respecto al eje z
alpha_i=45;                                 % ngulo  de rotaci n del LED con respecto al eje x

beta_j=45;                                  % ngulo  de inclinaci n del PD con respecto al eje z
alpha_j=45;                                 % ngulo  de rotaci n del PD con respecto al eje x

                            % wall roation angles
alpha_w1=60;
beta_w1=30;
alpha_w2=55;
beta_w2=35;
alpha_w=65;
beta_w=25;

gv=[20 60];                                 %uniform distribution probability
fv=[0 5];                                   %uniform distribution probability
W=6;                                        % width of obstacle
H=5;                                        % hight of obstacle
X=15;                                       %Lenght of mine
Y=10;                                       %height of mine
es=5;                                       % epsilon
t=5*10^-9;                                  % value of time
gymma=0.8;                                  %Reflection coefficient
g=0.53    ;                                 %Responsivity
f=1.5     ;                                 %Refractive index
kr=[0.1 0.001];                             %uniform distribution probability
km=[0 10];                                  %uniform distribution probability
ks=kr+km;                                   %uniform distribution probability
N=40;                                       %Number de scatters
rn=sqrt((x_j-x_s)^2+(y_j-y_s)^2+(z_j-z_s)^2);
p=0.1;                                      % parameter is used in calculation of Gn below equation 3.21

c=3*10^8 ;                                  % speed of light


%angulo de incidencia del enlace entre LED y PD for different position of
%1st position of receiver
incidencia_radian1=incline(x_i,y_i,z_i,x_j,y_j,z_j,alpha_j,beta_j);
incidencia1=rad2deg(incidencia_radian1) ; %conversion de radianes a grados
%2nd position of receiver
incidencia_radian2=incline(x_i,y_i,z_i,x_j2,y_j2,z_j2,alpha_j,beta_j);
incidencia2=rad2deg(incidencia_radian2);
%3rd position of receiver
incidencia_radian3=incline(x_i,y_i,z_i,x_j3,y_j3,z_j3,alpha_j,beta_j);
incidencia3=rad2deg(incidencia_radian3);
%4th position of receiver
incidencia_radian4=incline(x_i,y_i,z_i,x_j4,y_j4,z_j4,alpha_j,beta_j);
incidencia4=rad2deg(incidencia_radian4);
%5th position of receiver
incidencia_radian5=incline(x_i,y_i,z_i,x_j5,y_j5,z_j5,alpha_j,beta_j);
incidencia5=rad2deg(incidencia_radian5);


%angulo de irradiancia del enlace entre LED y PD
%1st position of receiver
irradiancia_radian1=rotacion(x_j,y_j,z_j,x_i,y_i,z_i,alpha_i,beta_i);
irradiancia1=rad2deg(irradiancia_radian1); %conversion de radianes a grados
```

```
%2nd position of receiver
irradiancia_radian2=rotacion(x_j2,y_j2,z_j2,x_i,y_i,z_i,alpha_i,beta_i);
irradiancia2=rad2deg(irradiancia_radian2) ;
%3rd position of receiver
irradiancia_radian3=rotacion(x_j3,y_j3,z_j3,x_i,y_i,z_i,alpha_i,beta_i);
irradiancia3=rad2deg(irradiancia_radian3) ;
%4th position of receiver
irradiancia_radian4=rotacion(x_j4,y_j4,z_j4,x_i,y_i,z_i,alpha_i,beta_i);
irradiancia4=rad2deg(irradiancia_radian4) ;
%5th position of receiver
irradiancia_radian5=rotacion(x_j5,y_j5,z_j5,x_i,y_i,z_i,alpha_i,beta_i);
irradiancia5=rad2deg(irradiancia_radian5) ;

%angulo de irradiancia del enlace entre LED y pared
irradiancialw_radian=rotacion(x_w,y_w,z_w,x_i,y_i,z_i,alpha_i,beta_i);
irradiancialw=rad2deg(irradiancialw_radian) ; %conversion de radianes a grados

%angulo de incidencia del enlace entre LED y pared
incidencialw_radian=incline(x_i,y_i,z_i,x_w,y_w,z_w,alpha_w,beta_w);
incidencialw=rad2deg(incidencialw_radian);  %conversion de radianes a grados

%angulo de irradiancia del enlace entre pared y PD
irradianciaw_radian=rotacion(x_j,y_j,z_j,x_w,y_w,z_w,alpha_w,beta_w);
irradianciaw=rad2deg(irradianciaw_radian);  %conversion from radian to degree

%angle de incidencia del enlace de pared a PD
%1st position of receiver
incidenciaw_radian11=incline(x_w1,y_w1,z_w1,x_j,y_j,z_j,alpha_j,beta_j);
incidenciaw11=rad2deg(incidenciaw_radian11);%conversion de radianes a grados

incidenciaw_radian21=incline(x_w2,y_w2,z_w2,x_j,y_j,z_j,alpha_j,beta_j);
incidenciaw21=rad2deg(incidenciaw_radian21);

incidenciaw_radian31=incline(x_w,y_w,z_w,x_j,y_j,z_j,alpha_j,beta_j);
incidenciaw31=rad2deg(incidenciaw_radian31);

%2st position of receiver
incidenciaw_radian12=incline(x_w1,y_w1,z_w1,x_j2,y_j2,z_j2,alpha_j,beta_j);
incidenciaw12=rad2deg(incidenciaw_radian12);%conversion de radianes a grados

incidenciaw_radian22=incline(x_w2,y_w2,z_w2,x_j2,y_j2,z_j2,alpha_j,beta_j);
incidenciaw22=rad2deg(incidenciaw_radian22);

incidenciaw_radian32=incline(x_w,y_w,z_w,x_j2,y_j2,z_j2,alpha_j,beta_j);
incidenciaw32=rad2deg(incidenciaw_radian32);

 %3rd position of receiver
incidenciaw_radian13=incline(x_w1,y_w1,z_w1,x_j3,y_j3,z_j3,alpha_j,beta_j);
incidenciaw13=rad2deg(incidenciaw_radian13);%conversion de radianes a grados

incidenciaw_radian23=incline(x_w2,y_w2,z_w2,x_j3,y_j3,z_j3,alpha_j,beta_j);
incidenciaw23=rad2deg(incidenciaw_radian23);

incidenciaw_radian33=incline(x_w,y_w,z_w,x_j3,y_j3,z_j3,alpha_j,beta_j);
incidenciaw33=rad2deg(incidenciaw_radian33);

%4th position of receiver
incidenciaw_radian14=incline(x_w1,y_w1,z_w1,x_j4,y_j4,z_j4,alpha_j,beta_j);
incidenciaw14=rad2deg(incidenciaw_radian14);%conversion de radianes a grados

incidenciaw_radian24=incline(x_w2,y_w2,z_w2,x_j4,y_j4,z_j4,alpha_j,beta_j);
incidenciaw24=rad2deg(incidenciaw_radian24);

incidenciaw_radian34=incline(x_w,y_w,z_w,x_j4,y_j4,z_j4,alpha_j,beta_j);
incidenciaw34=rad2deg(incidenciaw_radian34);

%5th position of receiver
incidenciaw_radian15=incline(x_w1,y_w1,z_w1,x_j5,y_j5,z_j5,alpha_j,beta_j);
incidenciaw15=rad2deg(incidenciaw_radian15);%conversion de radianes a grados

incidenciaw_radian25=incline(x_w2,y_w2,z_w2,x_j5,y_j5,z_j5,alpha_j,beta_j);
```

```
incidenciaw25=rad2deg(incidenciaw_radian25);

incidenciaw_radian35=incline(x_w,y_w,z_w,x_j4,y_j5,z_j5,alpha_j,beta_j);
incidenciaw35=rad2deg(incidenciaw_radian35);

% Calculation of distance from transmitter to receciver for five different
% position of receiver

  D1= DIST(x_i,y_i,z_i,x_j,y_j,z_j);
  D2= DIST(x_i,y_i,z_i,x_j2,y_j2,z_j2);
  D3= DIST(x_i,y_i,z_i,x_j3,y_j3,z_j3);
  D4= DIST(x_i,y_i,z_i,x_j4,y_j4,z_j4);
  D5= DIST(x_i,y_i,z_i,x_j5,y_j5,z_j5);


% Calculation of HLoS FOR 5 Values of receiver and their plots
[m_HLoS1,dl1]=HLoS_direct(x_i,y_i,z_i,x_j,y_j,z_j,Ap,eta,alpha_i,alpha_j,beta_i,beta_j,incidencia_radian
[m_HLoS2,dl2]=HLoS_direct(x_i,y_i,z_i,x_j2,y_j2,z_j2,Ap,eta,alpha_i,alpha_j,beta_i,beta_j,incidencia_rad
[m_HLoS3,dl3]=HLoS_direct(x_i,y_i,z_i,x_j3,y_j3,z_j3,Ap,eta,alpha_i,alpha_j,beta_i,beta_j,incidencia_rad
[m_HLoS4,dl4]=HLoS_direct(x_i,y_i,z_i,x_j4,y_j4,z_j4,Ap,eta,alpha_i,alpha_j,beta_i,beta_j,incidencia_rad
[m_HLoS5,dl5]=HLoS_direct(x_i,y_i,z_i,x_j5,y_j5,z_j5,Ap,eta,alpha_i,alpha_j,beta_i,beta_j,incidencia_rad
t1 = 1e-10:0.1e-9:30e-9 ;

y1=dirac(t1-dl1);
y2=dirac(t1-dl2);
y3=dirac(t1-dl3);
y4=dirac(t1-dl4);
y5=dirac(t1-dl5);
figure
hold on
grid on
title('graph for HLos')
xlabel('time (s)')
ylabel('Distance (m)')
zlabel('magnitude')

plot_HLoS1= plottt(y1,t1,m_HLoS1,D1);
plot_HLoS2= plottt(y2,t1,m_HLoS2,D2);
plot_HLoS3= plottt(y3,t1,m_HLoS3,D3);
plot_HLoS4= plottt(y4,t1,m_HLoS4,D4);
plot_HLoS5= plottt(y5,t1,m_HLoS5,D5);
legend([{'First position'},{'Second position'},{'Third position'},{'fourth position'},{'fifth position'}

view(3)


% Calculation of HnLoS for 5 Values of receiver and their plots

 [m_HnLoS1,dn1] =HnLos_calculation_total(x_i,y_i,z_i,x_j,y_j,z_j,x_w,y_w,z_w,x_w1,y_w1,z_w1,x_w2,y_w2,z_
;
 [m_HnLoS2,dn2] =HnLos_calculation_total(x_i,y_i,z_i,x_j2,y_j2,z_j2,x_w,y_w,z_w,x_w1,y_w1,z_w1,x_w2,y_w2
 [m_HnLoS3,dn3] =HnLos_calculation_total(x_i,y_i,z_i,x_j3,y_j3,z_j3,x_w,y_w,z_w,x_w1,y_w1,z_w1,x_w2,y_w2
;
 [m_HnLoS4,dn4] =HnLos_calculation_total(x_i,y_i,z_i,x_j4,y_j4,z_j4,x_w,y_w,z_w,x_w1,y_w1,z_w1,x_w2,y_w2
;
 [m_HnLoS5,dn5] =HnLos_calculation_total(x_i,y_i,z_i,x_j5,y_j5,z_j5,x_w,y_w,z_w,x_w1,y_w1,z_w1,x_w2,y_w2
;
 t1=1e-8:.1e-08:2.5e-8;
 figure
 hold on
 grid on
 title('graph for HnLos')
 xlabel('time (s)')
 ylabel('Distance (m)')
 zlabel('magnitude')

HnLoS_plot1= graph_draw(dn1,m_HnLoS1,t1,D1,3);
HnLoS_plot2= graph_draw(dn2,m_HnLoS2,t1,D2,3);
HnLoS_plot3= graph_draw(dn3,m_HnLoS3,t1,D3,3);
HnLoS_plot4= graph_draw(dn4,m_HnLoS4,t1,D4,3);
HnLoS_plot5= graph_draw(dn5,m_HnLoS5,t1,D5,3);
```

```
legend([{'First position'},{'Second position'},{'Third position'},{'fourth position'},{'fifth position'}
view(3)




%% Calculation of Hscatering for 5 Values of receiver and their plots
[m_Hscat1,ds1]=H_scater(x_i,y_i,z_i,x_j,y_j,z_j,Ap,m,f,g,gymma,kr,km,ks,p,N,irradiancia1,c,alpha_i,beta_
;
[m_Hscat2,ds2]=H_scater(x_i,y_i,z_i,x_j2,y_j2,z_j2,Ap,m,f,g,gymma,kr,km,ks,p,N,irradiancia1,c,alpha_i,be
[m_Hscat3,ds3]=H_scater(x_i,y_i,z_i,x_j3,y_j3,z_j3,Ap,m,f,g,gymma,kr,km,ks,p,N,irradiancia1,c,alpha_i,be
[m_Hscat4,ds4]=H_scater(x_i,y_i,z_i,x_j4,y_j4,z_j4,Ap,m,f,g,gymma,kr,km,ks,p,N,irradiancia1,c,alpha_i,be
[m_Hscat5,ds5]=H_scater(x_i,y_i,z_i,x_j5,y_j5,z_j5,Ap,m,f,g,gymma,kr,km,ks,p,N,irradiancia1,c,alpha_i,be
t1=5e-9:.1e-9:1.8e-8;
figure
hold on
grid on
title('graph for Hsca')
xlabel('time (s)')
ylabel('Distance (m)')
zlabel('magnitude')
scatering_plot1= graph_draw(ds1,m_Hscat1,t1,D1,40);
scatering_plot2= graph_draw(ds2,m_Hscat2,t1,D2,40);
scatering_plot3= graph_draw(ds3,m_Hscat3,t1,D3,40);
scatering_plot4= graph_draw(ds4,m_Hscat4,t1,D4,40);
scatering_plot5= graph_draw(ds5,m_Hscat5,t1,D5,40);
legend([{'First position'},{'Second position'},{'Third position'},{'fourth position'},{'fifth position'}
view(3)


%Calculation of Htotal for 5 Values of receiver and their plots
%Data prepation for five position of receiver for Htotal
 m_Htotal1=[m_HLoS1,m_HnLoS1,m_Hscat1];
 dt1=[dl1,dn1,ds1];
 m_Htotal2=[m_HLoS2,m_HnLoS2,m_Hscat2];
 dt2=[dl2,dn2,ds2];
 m_Htotal3=[m_HLoS3,m_HnLoS3,m_Hscat3];
 dt3=[dl3,dn3,ds3];
 m_Htotal4=[m_HLoS4,m_HnLoS4,m_Hscat4];
 dt4=[dl4,dn4,ds4];
 m_Htotal5=[m_HLoS5,m_HnLoS5,m_Hscat5];
 dt5=[dl5,dn5,ds5];
 t1=5e-9:.1e-9:2.8e-8;
figure
figure
hold on
grid on
title('graph for Htotal ')
xlabel('time (s)')
ylabel('Distance (m)')
zlabel('magnitude')
Htotal_plot1= graph_draw(dt1,m_Htotal1,t1,D1,44);
Htotal_plot2= graph_draw(dt2,m_Htotal2,t1,D2,44);
Htotal_plot3= graph_draw(dt3,m_Htotal3,t1,D3,44);
Htotal_plot4= graph_draw(dt4,m_Htotal4,t1,D4,44);
Htotal_plot5= graph_draw(dt5,m_Htotal5,t1,D5,44);
legend([{'First position'},{'Second position'},{'Third position'},{'fourth position'},{'fifth position'}
view(3)



% function to plot the graph for multiple impulse

function multi_pulse_plot= graph_draw(dm_total,m_total_Hscat,t1,D1,N)

for i=1:N
    y1=dirac(t1-dm_total(i));
    multi_pulse_plot= plottt(y1,t1,m_total_Hscat(i),D1);
end
```

```
end

% function to calculate the incidence angle
function ang_inc=incline(x1,y1,z1,x2,y2,z2,alpha,beta)
v=[x1-x2,y1-y2,z1-z2];
Ntilt=[cosd(alpha)*sind(beta),sind(alpha)*sind(beta),cosd(beta)];
d_p=dot_product(v,Ntilt);
d=sqrt((x1-x2)^2+(y1-y2)^2+(z1-z2)^2);
ang_inc=acos(d_p/d);
end

%funci n para calcular el angulo de irradiancia%
function ang_incidencia=rotacion(x1,y1,z1,x2,y2,z2,alpha,beta)
v=[x1-x2,y1-y2,z1-z2];
Ntilt=[cosd(alpha)*sind(beta),sind(alpha)*sind(beta),-cosd(beta)];
d_p=dot_product(v,Ntilt);
d=sqrt((x1-x2)^2+(y1-y2)^2+(z1-z2)^2);
ang_incidencia=acos(d_p/d);
end


%funcion to calculate the HnLos for three reflection points
function [HnLoS_Total,delta_t] =HnLos_calculation_total(x_i,y_i,z_i,x_j,y_j,z_j,x_w1,y_w1,z_w1,x_w2,y_w2
          [m_HnLoS1,dm1]=HnLos_calculation(x_i,y_i,z_i,x_j,y_j,z_j,x_w3,y_w3,z_w3,Aw,pw,alpha_i,alpha_j,a
          [m_HnLoS2,dm2]=HnLos_calculation(x_i,y_i,z_i,x_j,y_j,z_j,x_w1,y_w1,z_w1,Aw,pw,alpha_i,alpha_j,a
          [m_HnLoS3,dm3]=HnLos_calculation(x_i,y_i,z_i,x_j,y_j,z_j,x_w2,y_w2,z_w2,Aw,pw,alpha_i,alpha_j,a
          HnLoS_Total=[m_HnLoS1,m_HnLoS2,m_HnLoS3];
          delta_t=[dm1,dm2,dm3];



end


%funcion que calcula el HNLoS
function[m_HnLoS,dm]=HnLos_calculation(x_i,y_i,z_i,x_j,y_j,z_j,x_w,y_w,z_w,Aw,pw,alpha_i,alpha_j,alpha_w
    dv_iw= dv(x_i,y_i,x_w,y_w,fv);
    sv_iw= sv(x_i,y_i,z_i,x_w,y_w,z_w,fv);
    Piw=P_expt(gv,fv,W,H,X,Y,t,es, dv_iw,sv_iw);


    dv_wj= dv(x_w,y_w,x_j,y_j,fv);
    sv_wj= sv(x_w,y_w,z_w,x_j,y_j,z_j,fv);
    Pwj=P_expt(gv,fv,W,H,X,Y,t,es, dv_wj,sv_wj);


    g=gain(eta,inc,inc_r,fov);
    [v1,d1]=point_to_vector(x_i,y_i,z_i,x_w,y_w,z_w);
    Nnorm1=norm_vec_trans(alpha_i,beta_i);
    p1=dot_product(v1,Nnorm1);
    [v2,d2]=point_to_vector(x_w,y_w,z_w,x_i,y_i,z_i);
    Nnorm2=norm_vec_receiver(alpha_w,beta_w);
    p2=dot_product(v2,Nnorm2);
    [v3,d3]=point_to_vector(x_w,y_w,z_w,x_j,y_j,z_j);
    Nnorm3=norm_vec_receiver(alpha_w,beta_w);
    p3=dot_product(v3,Nnorm3);
    [v4,d4]=point_to_vector(x_j,y_j,z_j,x_w,y_w,z_w);
    Nnorm4=norm_vec_receiver(alpha_j,beta_j);
    p4=dot_product(v4,Nnorm4);

    digits(2);
    dm=((d1+d3)/c);
    dm=vpa(dm);
    dm=double(subs(dm));
    m_HnLoS= abs(((m+1)*Ap*Aw*pw*p1*p2*p3*p4*g*Piw*Pwj)/((d1^2)*(d3^2)*d1*d2*d3*d4));
    m_HnLoS=vpa(m_HnLoS);
    m_HnLoS=double(subs(m_HnLoS));
    end
```

```
%funci n para calcular el HLoS%
function [m_HLoS,dm]=HLoS_direct(x_i,y_i,z_i,x_j,y_j,z_j,Ap,eta,alpha_i,alpha_j,beta_i,beta_j,incidencia
    dv_ij= dv(x_i,y_i,x_j,y_j,fv);
    sv_ij= sv(x_i,y_i,z_i,x_j,y_j,z_j,fv);
    Pij=P_expt(gv,fv,W,H,X,Y,t,es, dv_ij,sv_ij);
    [v1,d1]=point_to_vector(x_i,y_i,z_i,x_j,y_j,z_j);
    Nnorm1=norm_vec_trans(alpha_i,beta_i);
    p1=dot_product(v1,Nnorm1);
    [v2,d2]=point_to_vector(x_j,y_j,z_j,x_i,y_i,z_i);
    Nnorm2=norm_vec_receiver(alpha_j,beta_j);
    p2=dot_product(v2,Nnorm2);
    g=gain(eta,incidencia,incidencia_r,fov);

    digits(2);
    dm= d1/c;
    dm=vpa(dm);
    dm=double(subs(dm));

    if (incidencia>=0) && (incidencia<=2*fov)
       m_HLoS=abs(((m+1)*Ap/(2*3.1416*d1^2))*(p1^m/d1)*(p2/d2)*g* Pij);
       m_HLoS=vpa(m_HLoS);
       m_HLoS=double(subs(m_HLoS));
    else
       m_HLoS=0;
    end
end


% Function to calculate the  Hscat for 40 scatering point
function [m_total_Hscat,dm_total]=H_scater(x_i,y_i,z_i,x_j,y_j,z_j,Ap,m,f,g,gymma,kr,km,ks,p,N,theta_ij,
          [v1,dij]=point_to_vector(x_i,y_i,z_i,x_j,y_j,z_j);

          dm_total=zeros(1,44);
          m_total_Hscat=zeros(1,40);
          for i =1:40

               Rr=0.5;
               rn=Rr*rand(1,1);
               theta_sn_j=randi([-180 180]);
               B_i_sn=Bisn(theta_sn_j,theta_ij);


               xs=rn*cosd(B_i_sn);
               ys=rn*sind(B_i_sn);
               zs=rn*cosd(theta_sn_j);
               phi_i_sn_radian=phi_scater(xs,ys,zs,x_i,y_i,z_i,alpha_i,beta_i);
               phi_i_sn=rad2deg(phi_i_sn_radian);

               di_sn=sqrt(rn^2+dij^2-2*rn*dij*cosd(B_i_sn));
               Di_j=di_sn+rn;
               Gn=Gain_n(f,g,gymma,phi_i_sn,kr,km,ks,p,N);

               digits(2);
               dm=(Di_j/c);
               dm=vpa(dm);
               dm=double(subs(dm));
               dm_total(i)=+dm;

               if (theta_sn_j>=-180) && (theta_sn_j<=180)
                    Hscat=abs(((m+1)*Ap*Gn/(2*3.1416*Di_j^2))*(cosd(phi_i_sn))^m*cosd(theta_sn_j));
                    Hscat=vpa(Hscat);
                    Hscat=double(subs(Hscat));
               else
                   Hscat=0;
               end
               m_total_Hscat(i)=+Hscat;


          end
end
```

```
%Function to calculate the  Pij for shadowing model
function Pij=P_expt(gv,fv,W,H,X,Y,t,es,d_v,s_v)
         syms w h x y p E

         if(gv(1)>=2*d_v) &&(gv(2)>=s_v)
             w_int=int(gv(1),w,0,W);
             h_int=int(gv(2),h,0,H);
             A=[w_int h_int];
             x_int=int(fv(1),x,0,X);
             y_int=int(fv(2),y,0,Y);
             B=[x_int y_int];
             exp_value=dot(A,B);
             f=p*t;
             est=-es*exp_value;
             d=vpa(subs(f,p,est),8);
             f=exp(E);
             Pij=vpa(subs(f,E,d),4);
         else
             Pij=0;
         end


end

%function to calculate the d(xv,yv)
function d_v= dv(x1,y1,x2,y2,fv)
          d_v= abs((y1-y2)*fv(1)-(x1-x2)*fv(2)-x2*y1+x1*y2)/sqrt((y1-y2)^2+(x2-x1)^2);
end


%function to calculate the s(xv,yv)
function s_v= sv(x1,y1,z1,x2,y2,z2,fv)
         if(z2<=z1)
             s_v=((y1-y2)^2+(x2-x1)^2+(fv(1)-x2)^2+(fv(2)-y2)^2-[(fv(1)-x1)^2+(fv(2)-y1)^2]/2*sqrt((y1-y
         else
             s_v=((y1-y2)^2+(x2-x1)^2+(fv(1)-x1)^2+(fv(2)-y1)^2-[(fv(1)-x2)^2+(fv(2)-y2)^2]/2*sqrt((y1-y

         end
end


%funcion para calcular la ganancia
function g=gain(eta,incide,incide_r,fov)
  if  (incide_r<=2*fov) && (incide_r>=0)
      g=(eta^2)/(sin(incide)^2);
  else
      g=0;
  end
end


% funcion para calcular el producto punto
function f=dot_product(a,b)
      f=dot(a,b);
end

% Calculo del vector normal para receptores
function m=norm_vec_receiver(alpha,beta)
     m=[cosd(alpha)*sind(beta),sind(alpha)*sind(beta),cosd(beta)];
end


% Calculo del vector normal para transmisores
function n=norm_vec_trans(alpha,beta)
      n=[cosd(alpha)*sind(beta),sind(alpha)*sind(beta),-cosd(beta)];
end
```

```
%funci n para calcular vector y distancia entre dos puntos
function [Vec,lenght]= point_to_vector(x1,y1,z1,x2,y2,z2)
      Vec=[x2-x1,y2-y1,z2-z1];
      lenght=sqrt((x2-x1)^2+(y2-y1)^2+(z2-z1)^2);

end


%calculation of Gn gain
function Gn=Gain_n(f,g,gymma,phi_i_sn,kr,km,ks,p,N)
        p_mie=pmie(f,g,phi_i_sn);
        p_ray=pray(gymma,phi_i_sn);
        p_total=(kr/ks)*p_ray+(km/ks)*p_mie;
        f_scat=p_total*sind(phi_i_sn);
        Gn=p*f_scat/N;
end

%calculation of pmie
function p_mie=pmie(f,g,phi_i_sn)
         p_mie=(1-g^2/4*pi)*(1/(1+g^2-2*g*cosd(phi_i_sn))^1.5+ f*3*(cosd(phi_i_sn))^2-1/2*(1+g^2)^1.5);
end


%calculation of pray
function p_ray=pray(gymma,phi_i_sn)
         p_ray=3*[1+3*gymma*(1-gymma)*(cosd(phi_i_sn))^2]/(16*pi*(1+2*gymma));
end

%scatering angles phi and theta
function phi_i_sn=phi_scater(x1,y1,z1,x2,y2,z2,alpha,beta)
v=[x1-x2,y1-y2,z1-z2];
Ntilt=[cosd(alpha)*sind(beta),sind(alpha)*sind(beta),-cosd(beta)];
d_p=dot_product(v,Ntilt);
d=sqrt((x1-x2)^2+(y1-y2)^2+(z1-z2)^2);
phi_i_sn=acos(d_p/d);
end

%scatering angle beta
function B_i_sn=Bisn(theta_sn_j,theta_ij)
if(theta_ij<theta_sn_j)
    B_i_sn=theta_sn_j-theta_ij;
else(theta_sn_j<theta_ij)
   B_i_sn= theta_ij-theta_sn_j;
end
end

% function to plot for one impulse
function plott= plottt(y1,t,dij,D)
         d = y1;
         idx = d == Inf; % find Inf
         d(idx) = dij;
         plott=plot3(t,D*ones(size(t)),d);
end

% Distance function
function D= DIST(x1,y1,z1,x2,y2,z2)

      D=sqrt((x2-x1)^2+(y2-y1)^2+(z2-z1)^2);

end
```